HETEROAGGREGATION BETWEEN ENGINEERED NANOMATERIALS AND HEMATITE NANOPARTICLES IN AQUATIC ENVIRONMENTS

by
Khanh An Huynh

A dissertation submitted to Johns Hopkins University in conformity with the requirements for the degree of Doctor of Philosophy

Baltimore, Maryland
February, 2014

ABSTRACT

The rapid growth in the use of engineered nanomaterials for industrial and research applications, as well as in consumer products, will inevitably result in the release of these nanomaterials into the environment. In natural and subsurface waters, engineered nanomaterials can undergo aggregation with each other (homoaggregation) or with other types of nanoparticles such as naturally occurring colloids (NOCs) (heteroaggregation). Since the concentration of engineered nanomaterials in natural aquatic systems is likely to be much lower than that of NOCs, heteroaggregation is expected to play a more important role than homoaggregation in determining the environmental fate and transport of engineered nanomaterials. While homoaggregation of engineered nanomaterials has been extensively investigated, the heteroaggregation behavior of these nanomaterials has rarely been studied and therefore is not well understood.

The objectives of this dissertation work were to investigate the heteroaggregation of engineered nanomaterials with hematite nanoparticles (HemNPs), a model NOC, and the effects of heteroaggregation on the antimicrobial activity of engineered nanomaterials. The engineered nanomaterials studied in this dissertation work were carbon nanotubes (CNTs) and silver nanoparticles (AgNPs). The first part of the dissertation effort focused on the heteroaggregation between CNTs and HemNPs. The rate and mechanism of CNT–HemNP heteroaggregation were demonstrated to depend on the concentration ratios of the two nanomaterials. Heteroaggregation rates were found to increase with increasing CNT/HemNP concentration ratio up to a point and to then decrease with further increase in the concentration ratio. In the presence of humic acid, the maximum heteroaggregation rate was observed to decrease when the humic acid concentration was increased. As the CNT–HemNP heteroaggregates were exposed to solution chemistries where there should be electrostatic and electrosteric repulsion between these nanoparticles, the strength of the heteroaggregates was presumably weakened, thus making the heteroaggregates more susceptible to disaggregation. The heteroaggregation behavior of two other carbon-based nanomaterials, namely, graphene oxide nanosheets and fullerene (C_{60}) nanoparticles, with HemNPs was also investigated and compared with that of CNTs with HemNPs.

The second part of the dissertation effort focused on the homoaggregation behavior of citrate- and polyvinylpyrrolidone (PVP)-coated AgNPs in different solution chemistries. The nature of homoaggregation of citrate-coated AgNPs NaCl solution was shown to be in excellent agreement with the Derjaguin–Landau–Verwey–Overbeek (DLVO) theory. PVP was found to be a more effective stabilizer than citrate in both monovalent (NaCl) and divalent ($CaCl_2$ and $MgCl_2$) electrolyte solutions. The adsorption of humic acid on citrate- and PVP-coated AgNPs was found to increase the colloidal stability of these nanoparticles in NaCl solutions and also at low $CaCl_2$ concentrations. Conversely, humic acid was observed to enhance the homoaggregation kinetics of both AgNPs at high $CaCl_2$ concentrations. In addition, the heteroaggregation between citrate-coated AgNPs and HemNPs was demonstrated to reduce the antimicrobial activity of AgNPs toward *Escherichia coli* bacteria. To our knowledge, this work is the first to describe this effect.

Advisor: Kai Loon Chen

Committee members: Edward J. Bouwer, William P. Ball, and D. Howard Fairbrother

ACKNOWLEDGEMENTS

First and foremost, I would like to thank my advisor, Professor Kai Loon Chen, who has been the most important person that helped me to persevere and succeed in my Ph.D. studies. I am so fortunate and grateful to have Kai Loon as my mentor. He has been always kind, patient, understanding, and supportive whenever I needed his help and advice. I believe that the skills and knowledge that I acquired with the help of Kai Loon are sufficient for me to build my own future successful career.

I would like to thank the members of my dissertation committee: Professors Edward Bouwer, Bill Ball, and Howard Fairbrother for spending their time reading this dissertation and providing me with valuable feedback throughout my Ph.D. studies. In addition, I would like to acknowledge Professors Haiou Huang and Joelle Frechette for serving on my Graduate Board Oral Examination, as well as Professors Alan Stone and Markus Hilpert for being the members of my Department Qualifying Examination. They have not only challenged me to improve my knowledge, but also have given me valuable suggestions to increase the quality of my work. My Ph.D. research could not be completed without the help from Dr. Michael McCaffery from the Integrated Imaging Center at JHU. Michael has been always an extremely helpful and patient collaborator, who agreed to spend a lot of his time capturing beautiful cryogenic transmission electron micrographs for my research projects. I would like to thank previous members of Fairbrother's group, Drs. Billy Smith and Kevin Wepasnick, for oxidizing and characterizing the carbon nanotubes used in my dissertation work.

I am extremely grateful to be a part of the Department of Geography and Environmental Engineering (DoGEE) with a very warm and friendly atmosphere that

made me always feel at home. At DoGEE, I have received a world-class education and made life-long friendships. I had the opportunities to take classes and have stimulating discussions with many inspiring professors such as Professors Edward Bouwer, Alan Stone, Bill Ball, and Lynn Roberts. I would like to specially thank Ed, Alan, and Bill for countlessly helping me on job hunting and giving me inputs and opinions regarding my research and future career plans. In addition, I would like to acknowledge tremendous help from Keith and other DoGEE staff members, such as Denise, Adena, Christine, Joyce, and Rob, during the time I spent at DoGEE.

I would like to thank the past and current members of Chen's research group, such as Peng, Li, Myunghee, Wenyu, Harry, Xitong, and Yeunook, for their help when we have been working together in the lab. I also would like to thank Jin, Pavlo, Amar, Andrew, Chip, Jessica, Katie, John, Nate, Phillip, Xiaomeng, and other students and postdocs in the wet groups at DoGEE for their support.

I would like to thank the Vietnam Education Foundation (VEF) for funding me through the first two years of my Ph.D. study. Because of their support, my dream of getting a Ph.D. degree from Hopkins has become a reality. Finally, I would like to thank my family members for their unconditional love, support, and encouragement. They have always been on my side whenever I had ups and downs during my Ph.D. studies, and helped me to see the light at the end of the long tunnel.

TABLE OF CONTENTS

Chapter 3. Disaggregation of Heteroaggregates Composed of Multiwalled Carbon Nanotubes and Hematite Nanoparticles 65

Chapter 4. Aggregation Kinetics of Citrate and Polyvinylpyrrolidone Coated Silver Nanoparticles in Monovalent and Divalent Electrolyte Solutions 91

LIST OF FIGURES

Chapter 2

Chapter 3

Chapter 4

Chapter 5

LIST OF TABLES

Chapter 2

Chapter 5

Chapter 1. Introduction

1.1. Two Popular Engineered Nanomaterials: Carbon Nanotubes and Silver Nanoparticles

Nanomaterials are materials with at least one external dimension in the size range of 1–100 nm.[1] Nanomaterials have been discovered to exhibit novel physicochemical, electrical, optical, and antimicrobial properties that their bulk materials do not possess. For example, the color of gold nanoparticle suspension depends on the size, shape, and aggregation states of these nanoparticles.[2] Graphene, which is single layers of carbon atoms packed into a honeycomb lattice,[3] has very high surface area (2,630 m^2/g) and thermal conductivity (~5,000 W/(m·K)).[4] Due to their photocatalytic properties, titanium dioxide nanoparticles can generate oxidizing species (*e.g.*, •OH radicals and $^1O_2$) when being irradiated.[5] For these reasons, engineered nanomaterials have been utilized in various applications, such as drugs, paints, and structural materials.[6-8]

Carbon nanotubes (CNTs) and silver nanoparticles (AgNPs) are reported to be the two most commonly used engineered nanomaterials in consumer products.[6] CNTs are cylindrical shape nanomaterials composed of coaxial tube(s) of carbon atoms in a helical arrangement.[9] Because of their unique molecular structure, CNTs have extraordinary physical, chemical, and electrical properties.[10, 11] The strength of nanotubes could be fifty times greater than that of steel wire. Depending on the chirality, CNTs can be either metallic or semiconducting.[10] These nanotubes are currently used in specialized medical appliances, batteries, and composite materials.[12] In the future, CNTs will be expected to be used in in transparent conducting films, field emission displays, flexible electronics, and water filters.[12] In many applications, such as composite materials and drug delivery agents, CNTs are required to be stable in an aqueous phase.[13, 14] However, this has been a challenge since CNTs have a strong tendency to undergo aggregation due to their hydrophobic graphene surfaces.[36, 37] To improve the colloidal stability of CNTs, hydrophilic and/or negatively-charged oxygen-containing functional groups, such as carboxyl and hydroxyl groups, could be grafted on the outer graphene sheet by using strong oxidizing agents.[14] As a result, oxidized CNTs become more hydrophilic and can be relatively stable in a broad range of solution chemistries.[14-16]

AgNPs have been used extensively in biomedical, chemical, and electrical engineering fields because of their antimicrobial, optical, and electrical properties.[17-21] Currently, there are about 320 tons of AgNPs produced and used worldwide per year.[22] AgNPs are being used as deodorizers and disinfectants in clothes, bandages, and food containers.[23] The use of medical devices coated with AgNPs (*e.g.*, endotracheal tubes) was reported to effectively reduce bacterial infection and potentially prevent the spread of antimicrobial resistance.[20, 24] AgNPs can be found in conductive inks used for printing electronic devices on plastic or paper.[21, 25] In addition, various studies have been conducted to explore the potential applications of silver nanomaterials for drinking water treatment and biological labeling.[26-28] Currently, the reduction of silver salts is one of the most common methods used to synthesize AgNPs.[19] To prevent aggregation, the surface of AgNPs is modified with capping agents, which are usually negatively charged species or relatively large and hydrophilic polymers, during or after synthesis.[29] The adsorption of these capping agents elevates the colloidal stability of AgNPs through the increase in electrostatic repulsion or the introduction of steric repulsion.[29] This enhancement in colloidal stability is especially critical for biomedical applications requiring stable AgNPs at high ionic strength conditions.[30] Citrate and polyvinylpyrrolidone (PVP) are the most commonly used capping agents for AgNPs.[31]

1.2. Fate and Transport of Carbon Nanotubes and Silver Nanoparticles in Aquatic Environments

CNTs and AgNPs will inevitably be released into the environment through the production, use, and disposal of products containing these nanomaterials.[23, 32-36] The recent discovery of Ag_2S nanoparticles in a wastewater treatment plant[37] is indicative of the presence of AgNPs in the environment.[37, 38] In natural and engineered aquatic systems, CNTs and AgNPs, or any engineered nanomaterial in general, will undergo aggregation, which is the association of particles to form clusters or aggregates.[39] Therefore, the bioavailability, as well as the environmental fate and transport of these nanomaterials, is greatly influenced by their aggregation behavior.[36, 40-43] For instance, the formation of aggregates may result in the removal of CNTs and AgNPs from the aqueous phase through sedimentation and thus lower their concentrations and bioavailability in this phase. In addition, aggregation can decrease the mobility of CNTs and AgNPs since large aggregates tend to move slower and settle faster than smaller aggregates or isolated nanoparticles. Furthermore, aggregation would also reduce the chemical reactivity of both CNTs and AgNPs.[44, 45]

Aggregation of engineered nanoparticles can occur through either homoaggregation or heteroaggregation. Homoaggregation is the aggregation between the same type of particles.[46, 47] Because aquatic systems contain many types of naturally occurring colloids, *e.g.*, hematite nanoparticles (HemNPs), microorganisms, clays, silica, and polysaccharides,[48] the homoaggregation of CNTs and AgNPs is unlikely to be the dominant aggregation process in these systems. Instead, the environmental fate and transport of these engineered nanomaterials are likely to be controlled by their aggregation with naturally occurring colloids,[46, 47] which is known as heteroaggregation. Nevertheless, the study of nanoparticle homoaggregation is still needed because it can provide a fundamental understanding of the aggregation behavior and colloidal stability of nanomaterials of interest in different environments. Results obtained from homoaggregation studies can also be employed to develop predictive models for (eco)toxicity of nanomaterials.[49] Therefore, homoaggregation of many types of nanoparticles, such as fullerene (C_{60}) nanoparticles,[50-52] cerium oxide nanoparticles,[53] viruses,[54] and HemNPs,[55-57] has been investigated under various experimental conditions using time-resolved dynamic light scattering (DLS).

To date, several studies on the homoaggregation of CNTs and AgNPs have been conducted. The homoaggregation kinetics of multiwalled and single-walled CNTs were found to be in qualitative agreement with Derjaguin−Landau−Verwey−Overbeek (DLVO) theory in solutions containing monovalent and divalent cations.[14, 15, 58, 59] The presence of macromolecules (*e.g.*, humic acid) and biomacromolecules (*e.g.*, alginate, bovine serum albumin, and cell culture medium) greatly reduced the homoaggregation kinetics of CNTs in NaCl solution.[58, 59] However, the homoaggregation kinetics of single-walled CNTs was enhanced in $CaCl_2$ solution in the presence of alginate.[59] The increase in surface oxygen content was reported to increase the stability of multiwalled CNTs in electrolyte solutions.[14, 15] Recently, Li and co-authors[60] performed homoaggregation experiments on unmodified AgNPs using time-resolved DLS to obtain the critical coagulation concentrations (CCCs) of these nanoparticles in different electrolyte solutions. Because the nanoparticles are completely destabilized at electrolyte concentrations higher than the CCCs,[61] the CCC provides a useful measure of the colloidal stability for AgNPs and therefore can be used to predict the fate and transport of AgNPs in natural and engineered systems. Although capping agents could change the surface properties and the colloidal stability of AgNPs considerably,[29] the effects of different capping agents on the CCCs of AgNPs have not yet been determined. Moreover, information on the influence of natural organic matter on the colloidal stability of AgNPs is still limited.

The heteroaggregation mechanisms and structures of heteroaggregates in binary suspensions containing oppositely charged latex particles,[62-66] micro-sized Al_2O_3 particles and SiO_2 nanoparticles,[67] and SiO_2 and aluminum-coated SiO_2 nanoparticles[68] have been investigated. In these suspensions, it was observed that heteroaggregation rates strongly depended on ionic strength and the distribution of nanoparticles.[62-64] The fractal dimension of heteroaggregates was found to increase as the solution ionic strength increased.[69] Currently, most of heteroaggregation studies have been conducted using spherical particles, while investigations on the heteroaggregation between spherical and non-spherical nanomaterials are still limited.[70] Therefore, there is a need for more information about the heteroaggregation behavior between nanomaterials of different shapes (*e.g.*, CNTs with HemNPs and graphene oxide (GO) nanosheets with HemNPs).

After homoaggregation or heteroaggregation, the aggregates containing either CNTs or AgNPs could go undergo disaggregation when the solution chemistry is changed or when the aggregates are exposed to strong hydrodynamic forces. As opposed to aggregation, disaggregation is expected to increase the mobility and chemical activity of these nanomaterials. In most disaggregation studies, the aggregates were usually disaggregated through the application of hydrodynamic forces[71-73] or ultrasound.[74-76] However, in many of these studies, no independent measurements were conducted to ensure that the amount of energy used to break the aggregates was consistent between experiments, which are critical for a fair comparison of the strength of aggregates. While there are some disaggregation studies on homoaggregates,[71, 73-78] the disaggregation of heteroaggregates composed of engineered nanomaterials (*e.g.*, CNTs) and naturally occurring colloids has never been studied.

1.3. Toxicity of Carbon Nanotubes and Silver Nanoparticles

Currently, the mechanisms for CNT toxicity are still not fully understood. CNTs have been observed to induce oxidative stress on bacteria and mammalian cells.[79, 80] In addition, CNT toxicity has been found to depend on nanotube surface properties.[81, 82] For instance, Magrez *et al.*[81] reported that the toxicity of CNTs on lung tumor cells increased significantly when carboxyl and hydroxyl groups were present on the nanotube surfaces. Kang *et al.*[82] observed similar results and they reported that functionalized CNTs were more toxic to *Escherichia coli* bacteria than untreated CNTs. It has been hypothesized that the toxicity of CNTs toward bacteria (*e.g.*, *E. coli*, *Pseudomonas aeruginosa*, *Staphylococcus aureus*, and *Bacillus subtilis*)[79, 82-85] and mouse macrophages[80] could be due to cell membrane damage resulting from direct cell–CNT contact.

AgNPs has been found to be toxic to bacteria, algae, and mammalian cells.[86-93] Some AgNP toxicity mechanisms have been proposed. They are (i) cell membrane damage, (ii) generation of reactive oxygen species (ROS), and (iii) dissolution of AgNPs.[92] Sondi and Salopek-Sondi[86] observed the incorporation of AgNPs into the cell membrane of *E. coli*, which potentially increased cell permeability and led to cell inactivation.[86] In a study conducted by Moroneset *et al.*,[89] AgNPs were found inside *E. coli* cells. The authors suggested that these intracellular AgNPs could cause cell damage through their interaction with sulfur- and phosphorus-containing compounds (*e.g.*, enzyme and DNA) inside the cell. Because ROS were observed to be generated and accumulated inside bacterial cells exposed with AgNPs, the toxicity of AgNPs was speculated to be related to ROS production.[94] Recently, Xiu *et al.*[95] performed toxicity experiments under both anaerobic (with no occurrence of AgNP dissolution) and aerobic (with occurrence of AgNP dissolution) conditions. They concluded that the dissolution of AgNPs (5–10 nm average diameter) was the main mechanism for AgNP toxicity to *E.coli*.

The toxicity of both CNTs and AgNPs has been found to be dependent on their homoaggregation states.[84, 96-100] In the case of AgNPs, the larger aggregates of AgNPs were found to be less toxic than the smaller aggregates or stable AgNPs.[96-100] The decrease in AgNP toxicity due to homoaggregation was attributed to the potential decrease in the effective AgNP surface area for AgNP dissolution[96, 98] and the decrease in the opportunities for AgNP–cell interactions.[100] Although heteroaggregation between AgNPs and naturally occurring colloids is expected to be the dominant aggregation process in aquatic environments, the effects of heteroaggregation on the antimicrobial activity of AgNPs has not been investigated to date.

1.4. Objectives and Scopes of Dissertation

The overall goals of this dissertation work were to investigate the heteroaggregation of engineered nanomaterials with hematite nanoparticles, a naturally occurring colloid, and the effects of heteroaggregation on the antimicrobial activity of engineered nanomaterials. The engineered nanomaterials of focus in this dissertation work were carbon nanotubes and silver nanoparticles. The specific objectives were to:

- determine the rates and elucidate mechanisms of heteroaggregation between CNTs and HemNPs;
- study the disaggregation of CNT homoaggregates and heteroaggregates that are composed of CNTs and HemNPs in different solution chemistries;
- examine and compare the effects of commonly used coating agents on the homoaggregation kinetics of AgNPs in monovalent and divalent electrolyte solutions; and
- investigate the effects of heteroaggregation on the antimicrobial activity of AgNPs.

1.5. Dissertation Organization

Chapter 2 focuses on the rates and mechanisms of heteroaggregation between negatively charged multiwalled CNTs and positively charged HemNPs. The CNTs were prepared by oxidizing as-received CNTs in a mixture of concentrated H_2SO_4 and HNO_3. The HemNPs were synthesized using the forced hydrolysis of $FeCl_3$ solution. In binary suspensions containing CNTs and HemNPs at low ionic strength, it was found that, under the conditions of these experiments, both CNTs and HemNPs were stable to homoaggregation and CNT–HemNP heteroaggregation occurred exclusively. By using time-resolved DLS, the CNT–HemNP heteroaggregation rates were obtained over a broad range of mass concentration ratios of CNTs and HemNPs. To elucidate the mechanisms of heteroaggregation, the structures of the CNT–HemNP heteroaggregates formed at different concentration ratios were observed through cryogenic transmission electron microscopy (cryo-TEM). The influence of humic acid on CNT–HemNP heteroaggregation was also investigated. In addition, the heteroaggregation between HemNPs and other carbon-based nanomaterials, such as C_{60} nanoparticles and GO nanosheets, were conducted and a comparison between their heteroaggregation behavior and that of CNTs and HemNPs was made.

In Chapter 3, the disaggregation behavior and the strength of heteroaggregates composed of multiwalled CNTs and HemNPs were examined in different solution chemistries. Oppositely charged CNTs and HemNPs were first allowed to undergo favorable heteroaggregation at pH 5.5 and 0.1 mM NaCl until the hydrodynamic diameters of the heteroaggregates reached *ca.* 400 nm. The heteroaggregates were subsequently exposed to three solution chemistries: (i) pH 5.5 with 0.1 mM NaCl, (ii) pH 11.0 with 0.1 mM NaCl, and (iii) pH 5.5 with 0.1 mM NaCl in the presence of 1 μg/L Suwannee River humic acid before they were disaggregated by ultrasound in an ultrasonication bath. The delivered ultrasonic power was determined by calorimetric method and was ensured to be the same in all disaggregation experiments. The heteroaggregate sizes before and after ultrasonication were measured by DLS in order to determine the degree of disaggregation and estimate the strength of heteroaggregates.

Chapter 4 presents the results from the investigation of the homoaggregation kinetics of AgNPs that were coated with two commonly used capping agents, citrate and polyvinylpyrrolidone (PVP). The unmodified AgNPs were synthesized through the reduction of Tollens' reagent by glucose in an ultrasonication bath. They were then cleaned and coated with citrate and PVP before being used in homoaggregation experiments. Time-resolved DLS was employed to measure the homoaggregation kinetics of the AgNPs over a range of monovalent (NaCl) and divalent ($CaCl_2$ and $MgCl_2$) electrolyte concentrations. Moreover, the influence of humic on the colloidal stability and homoaggregation kinetics of citrate- and PVP-coated AgNPs were also examined.

The effect of heteroaggregation between citrate-coated AgNPs and HemNPs on the antimicrobial activity of AgNPs is described in Chapter 5. The experiments presented in this chapter were conducted using *E. coli* bacteria in a phosphate-reduced Davis minimal medium. Centrifugal filters with MWCO of 3 kDa and an inductively coupled plasma mass spectrometry instrument (ICP-MS) were used to determine the AgNP and dissolved silver concentrations in the suspensions of interest. The bacterial growth in the test suspensions was determined through optical density measurements at 600 nm. By employing time-resolved DLS, the number concentration ratios of HemNPs and AgNPs that resulted in the desired heteroaggregate conformations were determined. The heteroaggregates having different conformations were then prepared and used for the evaluation of the effect of heteroaggregation on the antimicrobial activity of AgNPs. The dissolution of AgNPs in the presence of heteroaggregation was determined and the structures of heteroaggregates were observed under cryo-TEM. A mechanism for the effect of heteroaggregation on the antimicrobial activity of AgNPs was proposed.

1.6. References

1. European Commisssion. http://ec.europa.eu/environment/chemicals/nanotech/faq/definition_en.htm (01/17/2014),

2. Hu, M.; Chen, J. Y.; Li, Z. Y.; Au, L.; Hartland, G. V.; Li, X. D.; Marquez, M.; Xia, Y. N., Gold nanostructures: engineering their plasmonic properties for biomedical applications. *Chem Soc Rev* **2006,** *35*, (11), 1084-1094.

3. Geim, A. K.; Novoselov, K. S., The rise of graphene. *Nat Mater* **2007,** *6*, (3), 183-191.

4. Park, S.; Ruoff, R. S., Chemical methods for the production of graphenes. *Nat Nanotechnol* **2009,** *4*, (4), 217-224.

5. Fujishima, A.; Zhang, X. T.; Tryk, D. A., TiO2 photocatalysis and related surface phenomena. *Surf Sci Rep* **2008,** *63*, (12), 515-582.

6. The Project on Emerging Nanotechnologies - Analysis. http://www.nanotechproject.org/inventories/consumer/analysis_draft/ (07/25/2013),

7. West, J. L.; Halas, N. J., Engineered nanomaterials for biophotonics applications: Improving sensing, imaging, and therapeutics. *Annu Rev Biomed Eng* **2003,** *5*, 285-292.

8. Aitken, R. J.; Chaudhry, M. Q.; Boxall, A. B. A.; Hull, M., Manufacture and use of nanomaterials: current status in the UK and global trends. *Occup Med-Oxford* **2006,** *56*, (5), 300-306.

9. Iijima, S., Helical Microtubules of Graphitic Carbon. *Nature* **1991,** *354*, (6348), 56-58.

10. Baughman, R. H.; Zakhidov, A. A.; de Heer, W. A., Carbon nanotubes - the route toward applications. *Science* **2002,** *297*, (5582), 787-792.

11. Ajayan, P. M.; Zhou, O. Z., Applications of carbon nanotubes. *Top Appl Phys* **2001,** *80*, 391-425.

12. Endo, M.; Strano, M. S.; Ajayan, P. M., Potential applications of carbon nanotubes. *Top Appl Phys* **2008,** *111*, 13-61.

13. Jiang, L. Q.; Gao, L.; Sun, J., Production of aqueous colloidal dispersions of carbon nanotubes. *Journal of Colloid and Interface Science* **2003,** *260*, (1), 89-94.

14. Smith, B.; Wepasnick, K.; Schrote, K. E.; Bertele, A. H.; Ball, W. P.; O'Melia, C.; Fairbrother, D. H., Colloidal Properties of Aqueous Suspensions of Acid-Treated, Multi-Walled Carbon Nanotubes. *Environ Sci Technol* **2009,** *43*, (3), 819-825.

15. Smith, B.; Wepasnick, K.; Schrote, K. E.; Cho, H. H.; Ball, W. P.; Fairbrother, D. H., Influence of Surface Oxides on the Colloidal Stability of Multi-Walled Carbon Nanotubes: A Structure-Property Relationship. *Langmuir* **2009,** *25*, (17), 9767-9776.

16. Yi, P.; Chen, K. L., Influence of Surface Oxidation on the Aggregation and Deposition Kinetics of Multiwalled Carbon Nanotubes in Monovalent and Divalent Electrolytes. *Langmuir* **2011,** *27*, (7), 3588-3599.

17. McFarland, A. D.; Van Duyne, R. P., Single silver nanoparticles as real-time optical sensors with zeptomole sensitivity. *Nano Lett* **2003,** *3*, (8), 1057-1062.

18. Panáček, A.; Kvítek, L.; Prucek, R.; Kolár, M.; Večcřová, R.; Pizúrová, N.; Sharma, V. K.; Nevěčná, T. j.; Zbořil, R., Silver colloid nanoparticles: synthesis, characterization, and their antibacterial activity. *J. Phys. Chem. B* **2006,** *110*, 16248-16253.

19. Sharma, V. K.; Yngard, R. A.; Lin, Y., Silver nanoparticles: green synthesis and their antimicrobial activities. *Advances in Colloid and Interface Science* **2009,** *145*, (1-2), 83-96.

20. Shorr, A. F.; Zilberberg, M. D.; Kollef, M., Cost-Effectiveness Analysis of a Silver-Coated Endotracheal Tube to Reduce the Incidence of Ventilator-Associated Pneumonia. *Infect Cont Hosp Ep* **2009,** *30*, (8), 759-763.

21. Tang, B. L.; Chen, G. X.; Chen, Q. F.; Tai, J. L., Research and Manufacture of Nano-silver Conductive Ink. *Adv Mater Res-Switz* **2011,** *174*, 405-408.

22. Nowack, B.; Krug, H. F.; Height, M., 120 Years of Nanosilver History: Implications for Policy Makers. *Environ Sci Technol* **2011,** *45*, (4), 1177-1183.

23. Benn, T. M.; Westerhoff, P., Nanoparticle silver released into water from commercially available sock fabrics. *Environ Sci Technol* **2008,** *42*, (11), 4133-4139.

24. AGENTO I.C. Endotracheal Tube. http://bardmedical.com/Resources/Products/Documents/Brochures/Respiratory/Agento_PathoofVAP_0806-03.pdf (09/14),

25. InkTec Printed electronic. http://www.inktec.com/english/product_info/electronic.asp (09/14),

26. Li, Q. L.; Mahendra, S.; Lyon, D. Y.; Brunet, L.; Liga, M. V.; Li, D.; Alvarez, P. J. J., Antimicrobial nanomaterials for water disinfection and microbial control: Potential applications and implications. *Water Research* **2008,** *42*, (18), 4591-4602.

27. Schoen, D. T.; Schoen, A. P.; Hu, L. B.; Kim, H. S.; Heilshorn, S. C.; Cui, Y., High Speed Water Sterilization Using One-Dimensional Nanostructures. *Nano Lett* **2010,** *10*, (9), 3628-3632.

28. Schrand, A. M.; Braydich-Stolle, L. K.; Schlager, J. J.; Dai, L. M.; Hussain, S. M., Can silver nanoparticles be useful as potential biological labels? *Nanotechnology* **2008,** *19*, (23).

29. El Badawy, A. M.; Luxton, T. P.; Silva, R. G.; Scheckel, K. G.; Suidan, M. T.; Tolaymat, T. M., Impact of Environmental Conditions (pH, Ionic Strength, and Electrolyte Type) on the Surface Charge and Aggregation of Silver Nanoparticles Suspensions. *Environ Sci Technol* **2010,** *44*, (4), 1260-1266.

30. Doty, R. C.; Tshikhudo, T. R.; Brust, M.; Fernig, D. G., Extremely stable water-soluble Ag nanoparticles. *Chemistry of Materials* **2005,** *17*, (18), 4630-4635.

31. Tolaymat, T. M.; El Badawy, A. M.; Genaidy, A.; Scheckel, K. G.; Luxton, T. P.; Suidan, M., An evidence-based environmental perspective of manufactured silver nanoparticle in syntheses and applications: A systematic review and critical appraisal of peer-reviewed scientific papers. *Science of the Total Environment* **2010,** *408*, (5), 999-1006.

32. Farkas, J.; Peter, H.; Christian, P.; Urrea, J. A. G.; Hassellov, M.; Tuoriniemi, J.; Gustafsson, S.; Olsson, E.; Hylland, K.; Thomas, K. V., Characterization of the effluent from a nanosilver producing washing machine. *Environ Int* **2011,** *37*, (6), 1057-1062.

33. Geranio, L.; Heuberger, M.; Nowack, B., The Behavior of Silver Nanotextiles during Washing. *Environ Sci Technol* **2009,** *43*, (21), 8113-8118.

34. Kulthong, K.; Srisung, S.; Boonpavanitchakul, K.; Kangwansupamonkon, W.; Maniratanachote, R., Determination of silver nanoparticle release from antibacterial fabrics into artificial sweat. *Part Fibre Toxicol* **2010,** *7*.

35. Kohler, A. R.; Som, C.; Helland, A.; Gottschalk, F., Studying the potential release of carbon nanotubes throughout the application life cycle. *J Clean Prod* **2008,** *16*, (8-9), 927-937.

36. Petersen, E. J.; Zhang, L.; Mattison, N. T.; O'Carroll, D. M.; Whelton, A. J.; Uddin, N.; Nguyen, T.; Huang, Q.; Henry, T. B.; Holbrook, R. D.; Chen, K. L., Potential Release Pathways, Environmental Fate, And Ecological Risks of Carbon Nanotubes. *Environ Sci Technol* **2011,** *45*, (23), 9837-9856.

37. Kim, B.; Park, C. S.; Murayama, M.; Hochella, M. F., Discovery and Characterization of Silver Sulfide Nanoparticles in Final Sewage Sludge Products. *Environ Sci Technol* **2010,** *44*, (19), 7509-7514.

38. Nowack, B., Nanosilver Revisited Downstream. *Science* **2010,** *330*, (6007), 1054-1055.

39. Elimelech, M.; Gregory, J.; Jia, X.; Williams, R. A., *Particle deposition and aggregation: measurement, modelling, and simulation*. Butterworth-Heinemann: Oxford; Boston, 1995; p xv, 441 p.

40. Klaine, S. J.; Alvarez, P. J. J.; Batley, G. E.; Fernandes, T. F.; Handy, R. D.; Lyon, D. Y.; Mahendra, S.; McLaughlin, M. J.; Lead, J. R., Nanomaterials in the environment: Behavior, fate, bioavailability, and effects. *Environ Toxicol Chem* **2008,** *27*, (9), 1825-1851.

41. Petosa, A. R.; Jaisi, D. P.; Quevedo, I. R.; Elimelech, M.; Tufenkji, N., Aggregation and Deposition of Engineered Nanomaterials in Aquatic Environments: Role of Physicochemical Interactions. *Environ Sci Technol* **2010,** *44*, (17), 6532-6549.

42. Lowry, G. V.; Gregory, K. B.; Apte, S. C.; Lead, J. R., Guest Comment: Transformations of Nanomaterials in the Environment Focus Issue. *Environ Sci Technol* **2012,** *46*, (13), 6891-6892.

43. Lowry, G. V.; Gregory, K. B.; Apte, S. C.; Lead, J. R., Transformations of Nanomaterials in the Environment. *Environ Sci Technol* **2012,** *46*, (13), 6893-6899.

44. He, D.; Bligh, M. W.; Waite, T. D., Effects of Aggregate Structure on the Dissolution Kinetics of Citrate-Stabilized Silver Nanoparticles. *Environ Sci Technol* **2013,** *47*, (16), 9148-9156.

45. Brunet, L.; Lyon, D. Y.; Hotze, E. M.; Alvarez, P. J.; Wiesner, M. R., Comparative photoactivity and antibacterial properties of C60 fullerenes and titanium dioxide nanoparticles. *Environ Sci Technol* **2009,** *43*, (12), 4355-60.

46. Islam, A. M.; Chowdhry, B. Z.; Snowden, M. J., Heteroaggregation in colloidal dispersions. *Advances in Colloid and Interface Science* **1995,** *62*, (2-3), 109-136.

47. Buffle, J.; Wilkinson, K. J.; Stoll, S.; Filella, M.; Zhang, J. W., A generalized description of aquatic colloidal interactions: The three-colloidal component approach. *Environ Sci Technol* **1998,** *32*, (19), 2887-2899.

48. Buffle, J.; Leppard, G. G., Characterization of Aquatic Colloids and Macromolecules .1. Structure and Behavior of Colloidal Material. *Environ Sci Technol* **1995,** *29*, (9), 2169-2175.

49. Godwin, H. A.; Chopra, K.; Bradley, K. A.; Cohen, Y.; Harthorn, B. H.; Hoek, E. M. V.; Holden, P.; Keller, A. A.; Lenihan, H. S.; Nisbet, R. M.; Nel, A. E., The University of California Center for the Environmental Implications of Nanotechnology. *Environ Sci Technol* **2009,** *43*, (17), 6453-6457.

50. Chen, K. L.; Elimelech, M., Aggregation and Deposition Kinetics of Fullerene (C60) Nanoparticles. *Langmuir* **2006,** *22*, (26), 10994-11001.

51. Chen, K. L.; Elimelech, M., Influence of humic acid on the aggregation kinetics of fullerene (C-60) nanoparticles in monovalent and divalent electrolyte solutions. *Journal of Colloid and Interface Science* **2007,** *309*, (1), 126-134.

52. Chen, K. L.; Elimelech, M., Relating Colloidal Stability of Fullerene (C-60) Nanoparticles to Nanoparticle Charge and Electrokinetic Properties. *Environ Sci Technol* **2009,** *43*, (19), 7270-7276.

53. Buettner, K. M.; Rinciog, C. I.; Mylon, S. E., Aggregation kinetics of cerium oxide nanoparticles in monovalent and divalent electrolytes. *Colloid Surface A* **2010,** *366*, (1-3), 74-79.

54. Gutierrez, L.; Nguyen, T. H., Interactions between Rotavirus and Suwannee River Organic Matter: Aggregation, Deposition, and Adhesion Force Measurement. *Environ Sci Technol* **2012,** *46*, (16), 8705-8713.

55. Mylon, S. E.; Chen, K. L.; Elimelech, M., Influence of natural organic matter and ionic composition on the kinetics and structure of hematite colloid aggregation: Implications to iron depletion in estuaries. *Langmuir* **2004,** *20*, (21), 9000-9006.

56. Chen, K. L.; Mylon, S. E.; Elimelech, M., Aggregation kinetics of alginate-coated hematite nanoparticles in monovalent and divalent electrolytes. *Environ Sci Technol* **2006,** *40*, (5), 1516-1523.

57. Chen, K. L.; Mylon, S. E.; Elimelech, M., Enhanced aggregation of alginate-coated iron oxide (hematite) nanoparticles in the presence of calcium, strontium, and barium cations. *Langmuir* **2007,** *23*, (11), 5920-5928.

58. Saleh, N. B.; Pfefferle, L. D.; Elimelech, M., Aggregation Kinetics of Multiwalled Carbon Nanotubes in Aquatic Systems: Measurements and Environmental Implications. *Environ Sci Technol* **2008,** *42*, (21), 7963-7969.

59. Saleh, N. B.; Pfefferle, L. D.; Elimelech, M., Influence of Biomacromolecules and Humic Acid on the Aggregation Kinetics of Single-Walled Carbon Nanotubes. *Environ Sci Technol* **2010,** *44*, (7), 2412-2418.

60. Li, X.; Lenhart, J. J.; Walker, H. W., Dissolution-Accompanied Aggregation Kinetics of Silver Nanoparticles. *Langmuir* **2010,** *26*, (22), 16690-16698.

61. Chen, K. L.; Smith, B. A.; Ball, W. P.; Fairbrother, D. H., Assessing the colloidal properties of engineered nanoparticles in water: case studies from fullerene C-60 nanoparticles and carbon nanotubes. *Environmental Chemistry* **2010,** *7*, (1), 10-27.

62. Yu, W. L.; Borkovec, M., Distinguishing heteroaggregation from homoaggregation in mixed binary particle suspensions by multiangle static and dynamic light scattering. *Journal of Physical Chemistry B* **2002,** *106*, (51), 13106-13110.

63. Yu, W. L.; Matijevic, E.; Borkovec, M., Absolute heteroaggregation rate constants by multiangle static and dynamic light scattering. *Langmuir* **2002,** *18*, (21), 7853-7860.

64. Ryde, N.; Matijevic, E., Kinetics of Heterocoagulation .4. Evaluation of Absolute Coagulation Rate Constants Using a Classical Light-Scattering Technique. *J Chem Soc Faraday T* **1994,** *90*, (1), 167-171.

65. Puertas, A. M.; Fernandez-Barbero, A.; De Las Nieves, F. J., Charged colloidal heteroaggregation kinetics. *J Chem Phys* **2001,** *114*, (1), 591-595.

66. Lin, W.; Kobayashi, M.; Skarba, M.; Nu, C. D.; Galletto, P.; Borkovec, M., Heteroaggregation in binary mixtures of oppositely charged colloidal particles. *Langmuir* **2006,** *22*, (3), 1038-1047.

67. Cerbelaud, M.; Videcoq, A.; Abelard, P.; Pagnoux, C.; Rossignol, F.; Ferrando, R., Heteroaggregation between Al2O3 submicrometer particles and SiO2 nanoparticles: Experiment and simulation. *Langmuir* **2008,** *24*, (7), 3001-3008.

68. Kim, A. Y.; Berg, J. C., Fractal heteroaggregation of oppositely charged colloids. *Journal of Colloid and Interface Science* **2000,** *229*, (2), 607-614.

69. Kim, A. Y.; Hauch, K. D.; Berg, J. C.; Martin, J. E.; Anderson, R. A., Linear chains and chain-like fractals from electrostatic heteroaggregation. *Journal of Colloid and Interface Science* **2003,** *260*, (1), 149-159.

70. Afrooz, A. R. M. N.; Khan, I. A.; Hussain, S. M.; Saleh, N. B., Mechanistic Heteroaggregation of Gold Nanoparticles in a Wide Range of Solution Chemistry. *Environ Sci Technol* **2013,** *47*, (4), 1853-1860.

71. Chowdhury, I.; Hong, Y.; Honda, R. J.; Walker, S. L., Mechanisms of TiO2 nanoparticle transport in porous media: Role of solution chemistry, nanoparticle concentration, and flowrate. *Journal of Colloid and Interface Science* **2011,** *360*, (2), 548-555.

72. Jarvis, P.; Jefferson, B.; Gregory, J.; Parsons, S. A., A review of floc strength and breakage. *Water Research* **2005,** *39*, (14), 3121-3137.

73. Soos, M.; Ehrl, L.; Babler, M. U.; Morbidelli, M., Aggregate Breakup in a Contracting Nozzle. *Langmuir* **2010,** *26*, (1), 10-18.

74. Higashitani, K.; Yoshida, K.; Tanise, N.; Murata, H., Dispersion of Coagulated Colloids by Ultrasonication. *Colloid Surface A* **1993,** *81*, 167-175.

75. Wen, H. J.; Lee, D. J., Strength of cationic polymer-flocculated clay flocs. *Advances in Environmental Research* **1998,** *2*, (3), 390-396.

76. Quarch, K.; Durand, E.; Schilde, C.; Kwade, A.; Kind, M., Mechanical fragmentation of precipitated silica aggregates. *Chem Eng Res Des* **2010,** *88*, (12A), 1639-1647.

77. Baalousha, M., Aggregation and disaggregation of iron oxide nanoparticles: Influence of particle concentration, pH and natural organic matter. *Science of the Total Environment* **2009,** *407*, (6), 2093-2101.

78. Loosli, F.; Coustumer, P. L.; Stoll, S., TiO2 nanoparticles aggregation and disaggregation in presence of alginate and Suwannee River humic acids. pH and concentration effects on nanoparticle stability. *Water Research* *47*, (16), 6052-6063.

79. Kang, S.; Herzberg, M.; Rodrigues, D. F.; Elimelech, M., Antibacterial effects of carbon nanotubes: Size does matter. *Langmuir* **2008,** *24*, (13), 6409-6413.

80. Di Giorgio, M. L.; Di Bucchianico, S.; Ragnelli, A. M.; Aimola, P.; Santucci, S.; Poma, A., Effects of single and multi walled carbon nanotubes on macrophages: Cyto and genotoxicity and electron microscopy. *Mutat Res-Gen Tox En* **2011,** *722*, (1), 20-31.

81. Magrez, A.; Kasas, S.; Salicio, V.; Pasquier, N.; Seo, J. W.; Celio, M.; Catsicas, S.; Schwaller, B.; Forro, L., Cellular toxicity of carbon-based nanomaterials. *Nano Lett* **2006,** *6*, (6), 1121-1125.

82. Kang, S.; Mauter, M. S.; Elimelech, M., Physicochemical determinants of multiwalled carbon nanotube bacterial cytotoxicity. *Environ Sci Technol* **2008,** *42*, (19), 7528-7534.

83. Kang, S.; Pinault, M.; Pfefferle, L. D.; Elimelech, M., Single-walled carbon nanotubes exhibit strong antimicrobial activity. *Langmuir* **2007,** *23*, (17), 8670-8673.

84. Liu, S. B.; Wei, L.; Hao, L.; Fang, N.; Chang, M. W.; Xu, R.; Yang, Y. H.; Chen, Y., Sharper and Faster "Nano Darts" Kill More Bacteria: A Study of Antibacterial Activity of Individually Dispersed Pristine Single-Walled Carbon Nanotube. *ACS Nano* **2009,** *3*, (12), 3891-3902.

85. Young, Y. F.; Lee, H. J.; Shen, Y. S.; Tseng, S. H.; Lee, C. Y.; Tai, N. H.; Chang, H. Y., Toxicity mechanism of carbon nanotubes on Escherichia coli. *Mater Chem Phys* **2012,** *134*, (1), 279-286.

86. Sondi, I.; Salopek-Sondi, B., Silver nanoparticles as antimicrobial agent: a case study on *E. coli* as a model for Gram-negative bacteria. *Journal of Colloid and Interface Science* **2004,** *275*, (1), 177-182.

87. AshaRani, P. V.; Mun, G. L. K.; Hande, M. P.; Valiyaveettil, S., Cytotoxicity and Genotoxicity of Silver Nanoparticles in Human Cells. *ACS Nano* **2009,** *3*, (2), 279-290.

88. Navarro, E.; Piccapietra, F.; Wagner, B.; Marconi, F.; Kaegi, R.; Odzak, N.; Sigg, L.; Behra, R., Toxicity of Silver Nanoparticles to Chlamydomonas reinhardtii. *Environ Sci Technol* **2008,** *42*, (23), 8959-8964.

89. Morones, J. R.; Elechiguerra, J. L.; Camacho, A.; Holt, K.; Kouri, J. B.; Ramirez, J. T.; Yacaman, M. J., The bactericidal effect of silver nanoparticles. *Nanotechnology* **2005,** *16*, (10), 2346-2353.

90. Sotiriou, G. A.; Pratsinis, S. E., Antibacterial Activity of Nanosilver Ions and Particles. *Environ Sci Technol* **2010,** *44*, (14), 5649-5654.

91. Carlson, C.; Hussain, S. M.; Schrand, A. M.; Braydich-Stolle, L. K.; Hess, K. L.; Jones, R. L.; Schlager, J. J., Unique Cellular Interaction of Silver Nanoparticles: Size-Dependent Generation of Reactive Oxygen Species. *Journal of Physical Chemistry B* **2008,** *112*, (43), 13608-13619.

92. Marambio-Jones, C.; Hoek, E. M. V., A review of the antibacterial effects of silver nanomaterials and potential implications for human health and the environment. *Journal of Nanoparticle Research* **2010,** *12*, (5), 1531-1551.

93. Ivask, A.; George, S.; Bondarenko, O.; Kahru, A., Metal-Containing Nano-Antimicrobials: Differentiating the Impact of Solubilized Metals and Particles. In *Nano-Antimicrobials*, Cioffi, N.; Rai, M., Eds. Springer Berlin Heidelberg: 2012; pp 253-290.

94. Choi, O.; Hu, Z. Q., Size dependent and reactive oxygen species related nanosilver toxicity to nitrifying bacteria. *Environ Sci Technol* **2008,** *42*, (12), 4583-4588.

95. Xiu, Z. M.; Zhang, Q. B.; Puppala, H. L.; Colvin, V. L.; Alvarez, P. J., Negligible particle-specific antibacterial activity of silver nanoparticles. *Nano Lett* **2012,** *12*, (8), 4271-5.

96. Zook, J. M.; MacCuspie, R. I.; Locascio, L. E.; Halter, M. D.; Elliott, J. T., Stable nanoparticle aggregates/agglomerates of different sizes and the effect of their size on hemolytic cytotoxicity. *Nanotoxicology* **2011,** *5*, (4), 517-530.

97. Bae, E.; Park, H. J.; Lee, J.; Kim, Y.; Yoon, J.; Park, K.; Choi, K.; Yi, J., Bacterial Cytotoxicity of the Silver Nanoparticle Related to Physicochemical Metrics and Agglomeration Properties. *Environ Toxicol Chem* **2010,** *29*, (10), 2154-2160.

98. Zook, J.; Halter, M.; Cleveland, D.; Long, S., Disentangling the effects of polymer coatings on silver nanoparticle agglomeration, dissolution, and toxicity to determine mechanisms of nanotoxicity. *Journal of Nanoparticle Research* **2012,** *14*, (10), 1-9.

99. Kvitek, L.; Panacek, A.; Soukupova, J.; Kolar, M.; Vecerova, R.; Prucek, R.; Holecova, M.; Zboril, R., Effect of surfactants and polymers on stability and antibacterial activity of silver nanoparticles (NPs). *J Phys Chem C* **2008,** *112*, (15), 5825-5834.

100. Lok, C. N.; Ho, C. M.; Chen, R.; He, Q. Y.; Yu, W. Y.; Sun, H.; Tam, P. K. H.; Chiu, J. F.; Che, C. M., Silver nanoparticles: partial oxidation and antibacterial activities. *Journal of Biological Inorganic Chemistry* **2007,** *12*, (4), 527-534.

Chapter 2. Heteroaggregation of Multiwalled Carbon Nanotubes and Hematite Nanoparticles: Rates and Mechanisms*

---

*Most of the sections in this chapter has been published as: Huynh, K. A., McCaffery, J. M., and Chen, K. L., Heteroaggregation of Multiwalled Carbon Nanotubes and Hematite Nanoparticles: Rates and Mechanisms, *Environmental Science and Technology*, 2012, 46, 5912–5920. Co-author Michael McCaffery provided cryogenic-TEM images and helped with minor editing of the manuscript. Co-author Kai Loon Chen helped with data interpretation and manuscript editing.

2.1. Introduction

The utilization of carbon nanotubes (CNTs) in consumer products and industrial applications has increased significantly because of their extraordinary mechanical, electrical, and optical properties.[1-3] For example, transparent conductive CNT films can potentially replace the brittle and expensive indium tin oxide films that are currently used in touch screens, liquid crystal displays, and solar cells.[4, 5] The incorporation of CNTs in bicycle frames, car bodies, and windmill blades not only reduces the weight but also significantly enhances the mechanical strength of these structures.[6]

It is possible, therefore, that CNTs can enter aquatic ecosystems during the use and disposal of CNT-containing products.[7] Because CNTs have been shown to be toxic to bacteria and mammalian cells,[8, 9] the release of these nanotubes into natural aquatic systems can potentially cause adverse impacts on ecosystems and human health. Although the mechanisms of CNT toxicity are still being investigated, results from several studies indicate that the aggregation behavior of these nanomaterials is likely an important parameter that influences their toxicity.[9, 10]

Recently, some studies have been conducted to investigate *homoaggregation* (that is, aggregation between the same type of colloidal particles) of CNTs in aquatic environments.[11-15] It was observed that the homoaggregation behavior of CNTs conformed to the Derjaguin–Landau–Verwey–Overbeek (DLVO) theory in both monovalent and divalent electrolytes.[11, 12, 15] Moreover, the colloidal stability of these nanotubes was found to be strongly influenced by the nanotube surface oxygen content[12, 15] and solution chemistry, such as pH[11, 12] and natural organic matter concentration.[11]

In a heterogeneous colloidal system, *heteroaggregation*, or aggregation between different types of colloidal particles, can take place.[16-18] This process occurs in natural aquatic systems which contain a wide variety of naturally occurring inorganic, organic, and biological colloids, such as hematite (α-Fe_2O_3), colloidal organic matter, and microorganisms.[19] The presence of heteroaggregates comprising different types of naturally occurring colloids in surface waters had been observed through transmission electron microscopy (TEM).[16, 19, 20] Because the concentration of naturally occurring colloids is expected to be much higher than CNTs in natural aquatic systems, heteroaggregation is likely to play a more important role than homoaggregation in determining the fate and transport of CNTs once these nanotubes are released into the environment.[21] However, to date, heteroaggregation between CNTs and naturally occurring colloids has not been investigated.

The objective of this chapter is to determine the rates of heteroaggregation of CNTs and hematite nanoparticles (HemNPs), a naturally occurring colloid, over a broad range of nanoparticle distributions using time-resolved dynamic light scattering (DLS). The influence of humic acid, a key component of natural organic matter, on the heteroaggregation rates was also investigated. The structures of CNT–HemNP heteroaggregates formed at different nanoparticle distributions were evaluated using cryogenic TEM (cryo-TEM). The combinatorial use of DLS and cryo-TEM allowed the mechanisms of heteroaggregation of CNTs and HemNPs to be elucidated for the first time. Moreover, the heteroaggregation behavior of two other carbon-based nanomaterials, namely, graphene oxide (GO) nanosheets and fullerene (C_{60})

nanoparticles, with HemNPs is also investigated and compared with that of CNTs with HemNPs.

2.2. Materials and Methods

2.2.1. Preparation of Carbon-Based Nanomaterials and Hematite Nanoparticles

Pristine multiwalled CNTs (PD15L5-20, NanoLab Inc., Waltham, MA) were refluxed in a 3:1 volume mixture of 98% sulfuric acid (H_2SO_4) and 69% nitric acid (HNO_3) at 70 °C for 8 h. The concentration of pristine CNTs in the acid mixture was 12.5 mg/mL. To remove residual acids, metallic byproducts, and amorphous carbon, the oxidized CNTs were cleaned through repeated cycles of dilution with deionized (DI) water, ultracentrifugation at 1850 *g* (Powerspin LX, Unico, Dayton, NJ) for 5–10 min, and decantation of supernatant until the pH and resistivity of the supernatant was 5.5 and greater than 0.5 MΩ·cm, respectively. The cleaned CNTs were then dried in an oven overnight at 100°C and pulverized using a ball-mill (MM200, Retsch, Germany) for 15 min. After pulverization, the CNT powder was stored in a capped glass vial in the dark at room temperature. To prepare a CNT stock suspension, an ultrasonic bath (Branson 150R-MT, frequency 40 kHz) was used to disperse *ca.* 0.5 mg of CNT powder in 200 mL of deionized (DI) water (Millipore, MA) for 20 h. To remove CNT clusters that still remained in the suspension after ultrasonication, the suspension was centrifuged at 1400 *g* (Avanti centrifuge J-20 XPI, Beckman Coulter Inc., Brea, CA) for 5–10 min. The supernatant was then carefully transferred into a clean Pyrex bottle and stored in the dark at 4°C. This suspension will be referred to as CNT stock suspension.

5 mg of commercially available graphene oxide (single layer, SKU-GO-005, www.graphene-supermarket.com) was dispersed into 200 mL DI water through ultrasonication (Branson B1510 ultrasonication bath, 40 kHz) for six days. After ultrasonication, 35 mL of the suspension was filtered through a 0.22 μm cellulose acetate filter (Corning, NY). This process was repeated twice and all the filtrates were mixed together in a clean Pyrex bottle to obtain *ca.* 105 mL GO nanosheet stock suspension. For the preparation of C_{60} nanoparticle stock suspension, 252 mg of C_{60} powder (MR6HP, 99 % sublimed, Material & Electrochemical Research (MER) Corporation, AZ) was transferred into an autoclaved Pyrex bottle that contained 500 mL autoclaved DI water. The mixture was then stirred using a magnetic stirrer for 36 days in the dark at room temperature. Afterward, 250 mL of the mixture was filtered through a 0.22 μm cellulose acetate filter (Corning, NY). 50 mL of the filtrate was sequentially filtered through a 0.1 μm PVDF membrane (Millipore, MA). This process was conducted twice and the filtrates were mixed together in a clean Pyrex bottle to obtain *ca.* 100 mL C_{60} nanoparticle stock suspension. The bottles containing GO nanosheet and C_{60} nanoparticle stock suspensions were tightly capped, wrapped with aluminum foil, and stored at 4°C.

The total organic carbon (TOC) content of the CNT stock suspension was determined to be 1.39 mg/L through combustion catalytic oxidation at 680°C (TOC-VCSN, Shimadzu, Japan). The concentrations of the GO nanosheet and C_{60} nanoparticle stock suspensions were 11.66 mg/L and 1.67 mg/L, respectively, determined also through catalytic oxidation at 680°C (TOCL-CPH, Shimadzu, Japan). It is important to note that CNTs,[8, 10, 11, 22] GO nanosheets,[23-27] and C_{60} nanoparticles[28-31] were completely oxidized at 680°C. HemNPs were synthesized through the forced hydrolysis of $FeCl_3$.[32, 33] The concentration of the HemNP stock suspension was determined to be 4.4 g/L through gravimetric analysis.

2.2.2. Characterization of Carbon-Based Nanomaterials and HemNPs

The hydrodynamic diameters of the nanomaterials in the stock suspensions were determined using DLS. The structures and size distributions of these nanomaterials were determined through TEM imaging at 100 kV (TEM, FEI Tecnai 12 TWIN for CNTs and HemNPs, Philips EM 420 TEM for GO nanosheets and C_{60} nanoparticles). A 5–10 μL drop of the stock suspension of interest was deposited and dried on a carbon-coated copper TEM grid prior to being examined by the TEM. The length distribution of CNTs and size distribution of HemNPs were determined by measuring the lengths and diameters of over 500 randomly selected nanotubes and HemNPs, respectively (iTEM software, Olympus Soft Imaging Solutions GmbH, Münste, Germany). Additional high-resolution TEM (HR-TEM) images of CNTs and HemNPs were captured with a Philips CM300 FEG TEM. For HR-TEM imaging, CNT and HemNP samples were deposited and dried on lacey carbon-coated TEM copper specimen grids before being observed by TEM at 300 kV.

The electrophoretic mobilities (EPMs) of the nanoparticles were measured with a ZetaPALS analyzer (Brookhaven, Holtsville, NY) at 0.1 mM NaCl and pH 5.2 ± 0.2. All measurements were conducted at 25°C. For EPM measurements, the concentration of HemNPs was 0.88 mg/L. Meanwhile, the TOC concentrations of CNTs, GO nanosheets, and C_{60} nanoparticles were 0.56 mg/L, 1.17 mg/L, and 0.84 mg/L, respectively. The EPMs of HemNPs and CNTs were also determined in the presence of humic acid with concentrations ranging from 0.15 to 500.00 µg/L TOC. At least three nanoparticle samples were prepared for each solution chemistry and 10 EPM measurements were performed on each sample. Through X-ray photoelectron spectroscopy (XPS) analysis,[12, 34] the total surface oxygen content of CNTs was determined to be 10.3%.[15] The carboxyl groups made up nearly 70% of the total surface oxygen content, while the carbonyl and hydroxyl groups contributed 15% and 10%, respectively.[15]

2.2.3. Solution Chemistry

A NaCl stock solution was prepared with ACS-grade NaCl and then filtered through a 0.1-µm alumina syringe filter (Anotop 25, Whatman). All aggregation experiments were performed at an unadjusted pH of 5.2 ± 0.2. A humic acid stock solution was prepared by dissolving 12.8 mg of Suwannee River humic acid (SRHA) (Standard II, International Humic Substances Society) in 25 mL of deionized water (Millipore, MA). The mixture was stirred overnight in the dark at room temperature and filtered through a 0.22-µm cellulose acetate membrane filter (Millipore). Following that, the pH of the humic acid filtrate was adjusted to 10.3 and stored in the dark at 4°C. The TOC of the SHRA stock solution was determined to be 203.18 mg/L through UV-persulfate oxidation (Phoenix 8000 TOC analyzer, Tekmar-Dohrmann, Mason, OH).

2.2.4. Time-Resolved Dynamic Light Scattering

Time-resolved DLS measurements were conducted to obtain the aggregate hydrodynamic diameters as a function of time when carbon-based nanomaterials and HemNPs underwent homoaggregation or heteroaggregation. A light scattering unit comprising an argon laser (Lexel 95, Cambridge Laser) with a wavelength of 488 nm, a photomultiplier tube mounted on a goniometer (BI-200SM, Brookhaven), and a digital correlator (BI-9000AT, Brookhaven) was used to perform time-resolved DLS measurements. The goniometer houses a thermostated index-matching vat filled with a mixture of *cis*- and *trans*-decahydronaphthalene that was maintained at 25°C. All DLS measurements were performed at scattering angle of 90°. For each measurement, the autocorrelation function was accumulated over 15 s and an intensity-weighted diffusion coefficient was obtained through second-order cumulant analysis (Brookhaven software). The hydrodynamic diameter of the nanoparticles was then calculated using the Stokes-Einstein equation.[35] Time-resolved DLS measurements were performed over time periods of between 10 min and 2 h to allow for a large enough increase in hydrodynamic diameter for accurate derivation of homoaggregation and heteroaggregation rates.

For homoaggregation experiments, homoaggregation was induced by introducing a predetermined volume of NaCl stock solution into a borosilicate vial (VRW) that contained a diluted suspension of nanoparticles of interest. The suspension was briefly mixed (< 3 s) using a vortex mixer (Vortex Genie 2, Fisher) operated at its maximum setting and the vial was immediately inserted into the goniometer for DLS measurements. The final suspensions had a total volume of 1 mL. All the vials were only used once. Before use, they were soaked overnight in a cleaning solution (Extran MA01, Merck KGaA, Darmstadt, Germany), rinsed with copious DI water, and dried in an oven under dust-free conditions.

For the heteroaggregation experiments performed in the absence of humic acid, heteroaggregation between carbon-based nanomaterials (*e.g.*, CNTs, GO nanosheets, and C_{60} nanoparticles) and HemNPs was induced by adding a predetermined volume of carbon-based nanomaterial stock suspension into a vial containing a diluted HemNP suspension prepared with a NaCl solution. The HemNP and NaCl concentrations of the final suspensions were 0.44 mg/L and 0.1 mM, respectively. The CNT concentrations in the final suspensions were varied from 1 to 28 μg/L TOC. The concentrations of GO nanosheets and nC_{60} nanoparticles in the final suspensions were varied in the range of 1.9 – 466.4 μg/L TOC and 41.8 – 334.0 μg/L TOC, respectively.

For the heteroaggregation experiments between CNTs and HemNPs performed in the presence of humic acid, a premeasured volume of SRHA stock solution, followed by a premeasured volume of NaCl stock solution, was introduced into a vial containing a diluted HemNP suspension. Following that, a premeasured volume of CNT stock suspension was introduced into the mixture. In these experiments, the final calculated SRHA concentrations ranged from 0.15 to 500.00 μg/L TOC. The final concentrations of HemNPs, CNTs, and NaCl were the same as those used for the heteroaggregation experiments in the absence of humic acid.

All carbon-based nanomaterial, HemNP, and SRHA concentrations employed for the homoaggregation and heteroaggregation experiments are calculated based on the concentrations of the stock suspensions and stock solution and the dilution factors used to prepare the diluted suspensions.

2.2.5. Determination of Homoaggregation Kinetics

Before the investigation of heteroaggregation behavior of carbon-based nanomaterials and HemNPs, it is necessary to first characterize the colloidal stability of these nanoparticles through homoaggregation experiments. The experiments were conducted at (i) a CNT concentration of 83 μg/L TOC, (ii) a GO nanosheet concentration of 0.58 mg/L TOC, (iii) a C_{60} nanoparticle concentration of 1.52 mg/L TOC, and (iv) a HemNP concentration of 0.44 mg/L.

At the early stage of homoaggregation, the aggregation rate constant, k, is proportional to the initial rate of change of the homoaggregate hydrodynamic diameter, D_h:[36]

$$k \propto \frac{1}{N_0}\left(\frac{dD_h(t)}{dt}\right)_{t\to 0} \tag{2.1}$$

where t is time and N_0 is the initial primary particle concentration. The value of $\left(dD_h(t)/dt\right)_{t\to 0}$ was determined by performing a linear least-square analysis on the initial increase in D_h with t. For most NaCl concentrations, this analysis was performed over a time period in that D_h increased to 2.0 and 1.3 times of the initial hydrodynamic diameters of carbon-based nanomaterials and HemNPs, respectively. However, at low NaCl concentrations, D_h did not reach the desired values due to slow aggregation and the analysis was performed over 45 min instead. For all analyses, the y-intercept of the fitted line did not exceed 12 and 5 nm in excess of the initial hydrodynamic diameters of carbon-based nanomaterial and HemNPs, respectively.

The homoaggregation kinetics of nanoparticles were quantified using the attachment efficiency, α, that is calculated by normalizing the homoaggregation rate constant at the electrolyte concentration of interest, k, to that obtained under favorable aggregation condition, k_{fast}:[28, 33, 36, 37]

$$\alpha = \frac{k}{k_{fast}} = \frac{\frac{1}{N_0}\left(\frac{dD_h(t)}{dt}\right)_{t\to 0}}{\frac{1}{(N_0)_{fast}}\left(\frac{dD_h(t)}{dt}\right)_{t\to 0, fast}} \tag{2.2}$$

The terms with subscript “fast” refer to favorable conditions. The critical coagulation concentrations (CCCs) of carbon-based nanomaterials and HemNPs can then be derived by determining the intersections of extrapolations through reaction-limited and diffusion-limited regimes of the inverse-stability profiles and were used to quantify the colloidal stability of both nanoparticles.[21]

2.2.6. Determination of Heteroaggregation Rates

Time-resolved DLS was employed to determine heteroaggregation rates, dD_h/dt, in binary suspensions comprising carbon-based nanomaterials and HemNPs. All the heteroaggregation experiments were performed at a constant HemNP concentration of 0.44 mg/L, while the CNT concentrations were varied from 1 to 28 μg/L TOC. These nanoparticle concentrations resulted in the mass concentration ratio of CNTs and HemNPs (CNT/HemNP ratios) in the range of 0.002 – 0.064. Meanwhile, the concentrations of GO nanosheets and C_{60} nanoparticles were in the range of 1.9 – 466.4 μg/L TOC (GO/HemNP ratio = 0.004–1.060) and 41.8 – 334.0 μg/L TOC (C_{60}/HemNP ratio = 0.095 – 0.760), respectively. Since there is no reliable method to estimate the number concentration carbon-based nanomaterials, the concentration ratios used in heteroaggregation experiments were calculated based on the TOC concentrations of carbon-based nanomaterials and the mass concentration of HemNPs.

Before the heteroaggregation experiments were conducted, scattered light intensities from a HemNP suspension with a concentration of 0.44 mg/L, a CNT suspension with a concentration of 28 μg/L TOC, and a 0.1 mM NaCl solution (with no nanoparticles) were measured using the light scattering unit at the same incident laser intensity (Figure 2.1). At these nanoparticle concentrations, the scattered light intensity from the HemNP suspension was considerably higher (by ca. 20 times) than that of the CNT suspension. In comparison to the HemNP suspension, the scattered light intensity from the CNT suspension was only slightly higher than that of the NaCl solution, likely due to the relatively low concentration of CNTs and/or the optical properties of CNTs. Since the nanotube concentration of the CNT suspension (*i.e.*, 28 μg/L TOC) is equal to the highest concentration used for the CNT–HemNP heteroaggregation experiments and the scattered light intensity contributed by CNTs is proportional to the concentration of nanotubes, these observations show that the scattered light from binary suspensions for all the heteroaggregation experiments was largely contributed by HemNPs. The same phenomenon was also observed in binary suspensions containing either GO nanosheets and HemNPs or C_{60} nanoparticles and HemNPs. Hence, time-resolved DLS can be employed to monitor the growth in the hydrodynamic diameter of the heteroaggregates, which is equivalent to the hydrodynamic diameter of HemNPs while they undergo heteroaggregation with carbon-based nanomaterials. This approach to determine heteroaggregation rates is similar to that used by Ferretti *et al.*,[38] who measured the time evolution of hydrodynamic diameter of HemNPs in the presence of extracellular polysaccharides.

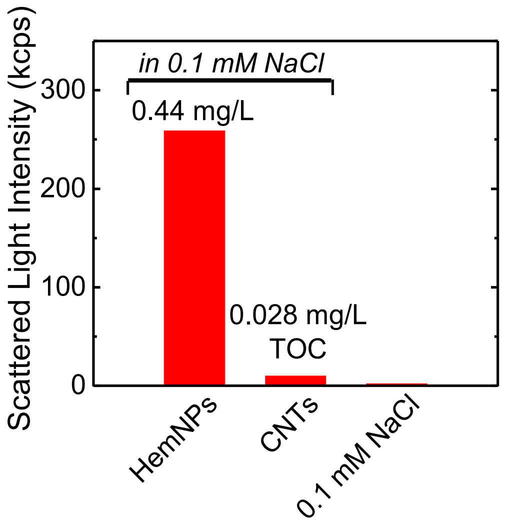

Figure 2.1. Scattered light intensities from HemNP suspension (0.44 mg/L), CNT suspension (28 μg/L TOC), and 0.1 mM NaCl solution at the same incident laser intensity. Intensities are presented in kilo counts per second (kcps).

At each concentration ratio, the heteroaggregation rate was determined by performing linear least-square analysis on the increase in aggregate hydrodynamic diameter, D_h, with t. In most cases, the analysis was performed over a time period in that D_h reached 1.3 times of the initial hydrodynamic diameter of HemNPs, $D_\mathrm{h,0}$. In the case of slow heteroaggregation, D_h failed to reach $1.3D_\mathrm{h,0}$ and the linear regression was performed instead over a time period of greater than 30 minutes. For all analyses, the y-intercepts of the fitted lines did not exceed 8 nm in excess of $D_\mathrm{h,0}$.

2.2.7. Cryogenic Transmission Electron Microscopy

Cryo-TEM was employed to examine the CNT–HemNP heteroaggregate structures formed at relative concentrations of 0.003, 0.032, and 0.127. The heteroaggregate suspensions were prepared in the same solution chemistry as that used for the heteroaggregation experiments (0.1 mM NaCl and pH 5.2) *ca.* 15 minutes before the vitrification process. CNT and HemNP concentrations used for cryo-TEM imaging were 10 times higher than the concentrations used for heteroaggregation experiments to allow for the formation of a reasonable number of heteroaggregates on each TEM grid. In addition, homoaggregates of CNTs prepared at a concentration of 1.25 mg/L TOC and a solution chemistry of 500 mM NaCl were observed with cryo-TEM 15 min after the onset of homoaggregation.

For preparing vitrified specimens, Lacey carbon-coated TEM copper grids were first ionized in a high vacuum evaporator (Denton 502A, Moorestown, NJ) for 30 s to increase the hydrophilicity of the grid surfaces. The ionized grid was then placed into a temperature/humidity controlled chamber of an automated vitrification robot (Vitrobot^{TM}) (FEI Vitrobot Mark IV, Hillsboro, OR) for specimen vitrification. The temperature and relative humidity of the chamber were maintained at 22°C and > 90 %, respectively. 10 μL of suspension containing the aggregates of interest was deposited on the ionized grid; and the Vitrobot^{TM} then blotted the grid with filter paper to remove excess water. The high humidity minimizes the evaporation from the film of water (*ca.* 100–200 nm in thickness) on the grid after blotting, while the ionization of the grid promotes spreading of the thin water layer uniformly on the grid surface. After blotting, the specimen was rapidly plunged into a cryogen reservoir containing liquid ethane that was cooled by liquid nitrogen. The blotting and plunging were done automatically by the Vitrobot^{TM} with the predefined blotting and plunging parameters presented in Table 2.1. With the combination of these parameters and grid ionization, we reproducibly obtained a thin and uniform layer of vitreous ice containing aggregates of interest after vitrification.

Table 2.1. Blotting and plunging parameters for cryo-TEM

Parameter	Value
Blot time	1 s
Wait time [a]	0 s
Drain time [b]	0 s
Blot force [c]	2
Blot total [d]	1

[a] The time between blotting.
[b] Wait time between blotting and vitrification.
[c] Scale from 0 to 10 with the increment of 1.0.
[d] Number of blotting.

After being plunged into liquid nitrogen-cooled ethane, the vitreous specimen was quickly transferred to liquid nitrogen and subsequently transferred into a cryo workstation filled with liquid nitrogen (Gatan 626 workstation, Pleasanton, CA). The specimen was then placed in the tip of the cryo holder (Gatan 626 70° single tilt liquid nitrogen holder, Pleasanton, CA) and inserted into the TEM. Different from the standard holder used in conventional TEM, the cryo holder has a shutter to shield the frozen hydrate specimen when it is being transferred into the TEM. The cryo holder also has a dewar, which contains sorbent material (zeolite) internally at its base, and is filled with liquid nitrogen to keep the temperature of the specimen below –160°C for TEM imaging. After insertion of the specimen into the TEM, the specimen was allowed to stabilize for 10–20 minutes, typically to a temperature of –174°C. During TEM imaging, the specimen temperature was monitored continuously by a cold stage controller (SmartSet 900, Gatan, Pleasanton, CA).

The images of the vitreous specimen were taken by an Eagle 2K CCD camera (FEI, Hillsboro, OR) mounted in the on-axis position of a Tecnai 12 TWIN transmission microscope operated at 100 kV. Due to the high dynamic range and sensitivity of this camera, clear TEM micrographs were taken at extremely low electron-beam irradiation.

This is critical in cryo-TEM imaging because high electron-beam radiation can cause the deformation and melting of the vitreous ice layer. The anti-contamination cryo-box of the TEM was charged with liquid nitrogen to minimize the contamination of specimen adjacent areas inside the TEM.

2.3. Results and Discussion

2.3.1. Physicochemical Properties of Carbon-Based Nanomaterials and HemNPs

Representative TEM images of CNTs, GO nanosheets, C_{60} nanoparticles, and HemNPs are presented in Figure 2.2. The carbon-based nanomaterials were observed to be polydisperse. CNTs were generally crooked due to the presence of defects on the tube walls that were formed during acid treatment (Figure 2.2a). GO nanosheets had a plate-like (2D) structure (Figure 2.2b). C_{60} nanoparticles were nearly spherical with slight angular feature (Figure 2.2c) while the HemNPs were mostly spherical (Figure 2.2d). High-resolution TEM imaging revealed multiple graphene layers making up the nanotube walls, as well as the angular features of the HemNPs (Figure 2.3). Figure 2.4 presents the length and size distributions of CNTs and HemNPs, respectively. The mean length of CNTs was 376 nm, while the HemNPs had an average diameter of 87 nm. From 20 DLS measurements, the average hydrodynamic diameters of CNTs and HemNPs were 109.8 nm and 80.7 nm, respectively. Also from DLS measurements, GO nanosheets and C_{60} nanoparticles were found to have average hydrodynamic diameters of 138.0 nm and 86.8 nm, respectively.

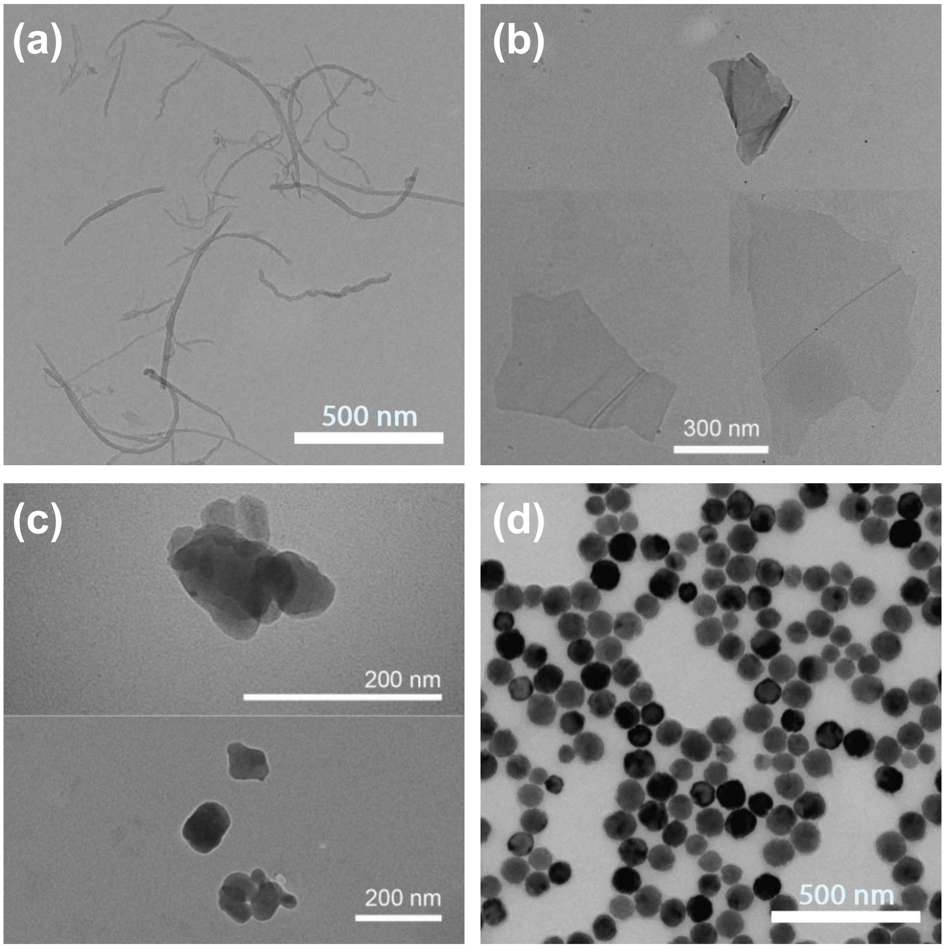

Figure 2.2. Representative TEM images of (a) CNTs, (b) GO nanosheets, (c) C_{60} nanoparticles, and (d) HemNPs.

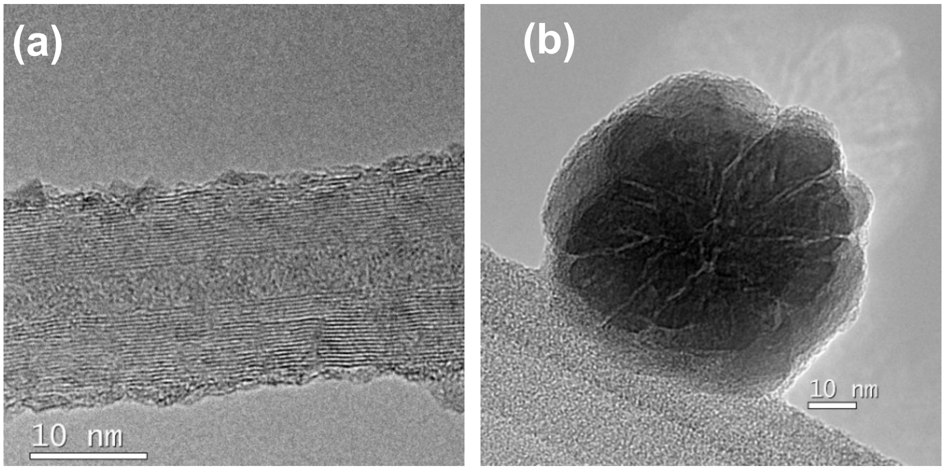

Figure 2.3. High-resolution TEM images of (a) a CNT and (b) a HemNP.

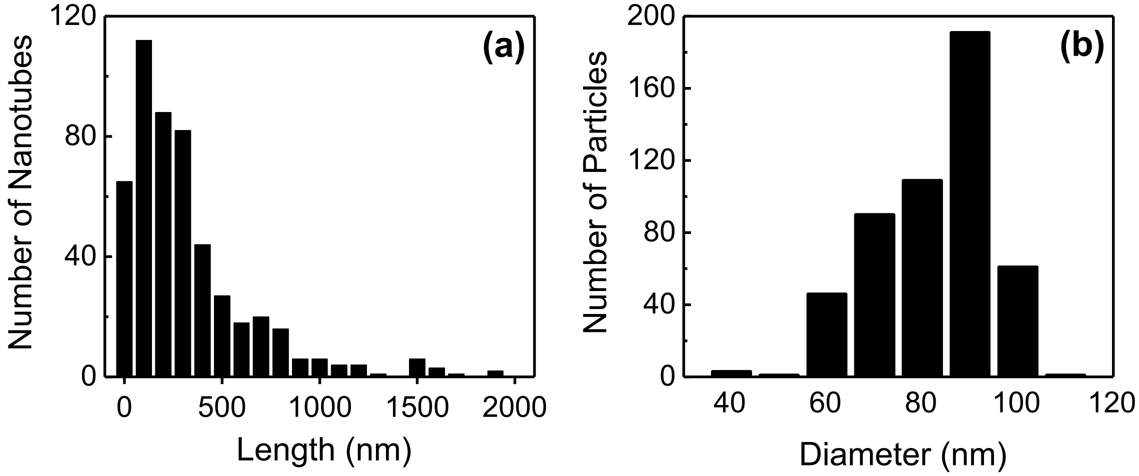

Figure 2.4. (a) Length distribution of CNTs with each bar representing a length range of 100 nm. (b) Size distribution of HemNPs with each bar representing a diameter range of 10 nm.

2.3.2. Electrokinetic Properties of Carbon-Based Nanomaterials and HemNPs

The average EPM of CNTs prepared in a 0.1 mM NaCl and pH 5.2 solution was -2.09×10^{-8} $m^2/(V \cdot s)$ (standard deviation = 0.53×10^{-8} $m^2/(V \cdot s)$). The dissociation of surface carboxyl groups of the CNTs is expected to result in the negative surface charge of the nanotubes. Since carbonyl and hydroxide groups are not likely to dissociate at the experimental condition[39, 40] and their surface densities are relatively small, both groups are not expected to contribute significantly to the surface charge of CNTs. At the same solution chemistry, the average EPM of GO nanosheets was -1.35×10^{-8} $m^2/(V \cdot s)$ (standard deviation = 0.90×10^{-8} $m^2/(V \cdot s)$) and that of C_{60} nanoparticles was -1.09×10^{-8} $m^2/(V \cdot s)$ (standard deviation = 0.68×10^{-8} $m^2/(V \cdot s)$). The average EPM of HemNPs prepared in a 0.1 mM NaCl and pH 5.2 solution was 1.79×10^{-8} $m^2/(V \cdot s)$ (standard deviation = 0.82×10^{-8} $m^2/(V \cdot s)$). HemNPs are expected to be positively charged in this solution chemistry since their isoelectric point is 9.[41, 42]

2.3.3. Homoaggregation Kinetics of Carbon-Based Nanomaterials and HemNPs

Representative homoaggregation profiles of 83 μg/L CNTs and 0.44 mg/L HemNPs at 4 different NaCl concentrations are shown in Figure 2.5a and b, respectively. For both CNTs and HemNPs, as the NaCl concentration was increased, the initial slope of the aggregation profiles increased until it reached a maximum. The reaction-limited and diffusion-limited regimes can be observed from the inverse-stability profiles for both CNTs and HemNPs (Figure 2.6), indicating that their aggregation behavior was in qualitative agreement with DLVO theory. In the reaction-limited regime (*i.e.*, $\alpha < 1$), an increase in NaCl concentration resulted in an increase in the degree of charge screening of the CNTs and HemNPs and reduced the energy barrier to homoaggregation, as reflected by an increase in attachment efficiencies.

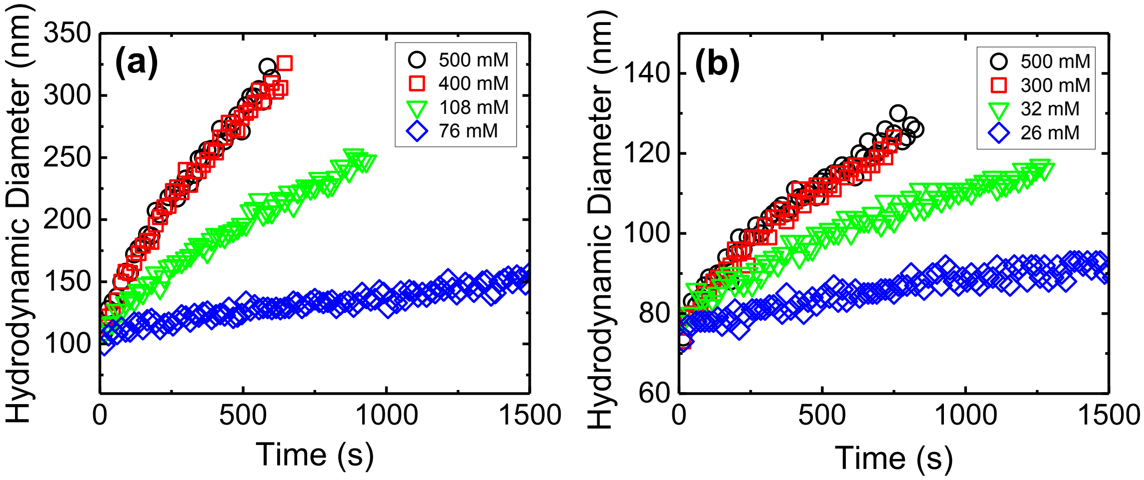

Figure 2.5. Representative homoaggregation profiles of (a) CNTs at a concentration of 83 μg/L TOC and (b) HemNPs at a concentration of 0.44 mg/L at different NaCl concentrations.

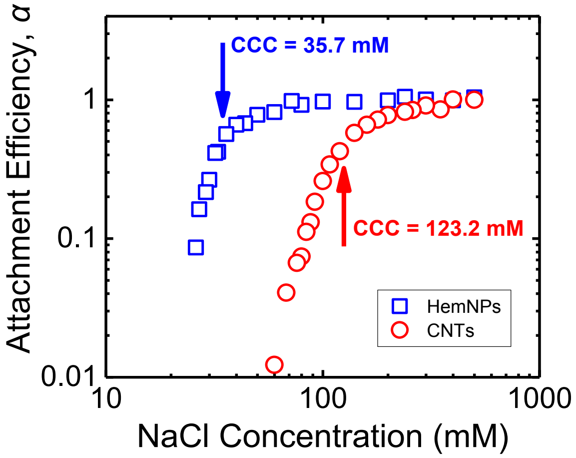

Figure 2.6. Attachment efficiencies of CNTs and HemNPs as functions of NaCl concentration at pH 5.2.

At electrolyte concentrations above the CCCs, the surface charge of both nanoparticles was completely screened and the energy barrier was eliminated. Under such conditions, the nanoparticles underwent diffusion-limited (fast) homoaggregation (*i.e.*, $\alpha = 1$). A representative cryo-TEM image of a CNT homoaggregate formed in the diffusion-limited regime at 500 mM NaCl shows that the homoaggregate had a loose, net-like structure (Figure 2.7). At pH 5.2, the CCC of CNTs (123.2 mM NaCl) was considerably higher than that of HemNPs (35.7 mM NaCl), indicating that the CNTs were colloidally more stable than the HemNPs. Furthermore, the CCC of CNTs at pH 5.2 was lower than that at pH 7.1 (*i.e.*, 210 mM NaCl[15]) because fewer carboxyl groups on CNT surfaces are protonated at the lower pH.

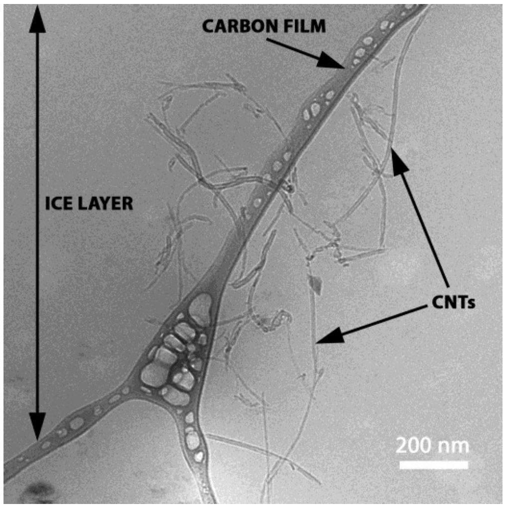

Figure 2.7. Cryo-TEM image of a CNT homoaggregate after 20 min of aggregation at 500 mM NaCl and pH 5.2. CNT concentration was 1.25 mg/L TOC.

The homoaggregation kinetics of the GO nanosheets and C_{60} nanoparticles in NaCl solution at pH 5.2 ± 0.2 were also investigated. The GO nanosheet concentration used in the homoaggregation experiments was 0.58 mg/L TOC. The attachment efficiencies of the GO nanosheets at different NaCl concentrations are presented in Figure 2.8a. Similar to CNTs and HemNPs, the homoaggregation behavior of GO nanosheets was also found to qualitatively follow the DLVO theory. These nanosheets have a CCC of 227 mM NaCl, which is close to the CCC value of 188 mM obtained by Wu *et al.*[43]

Homoaggregation experiments of C_{60} nanoparticles were conducted at a C_{60} nanoparticle concentration of 1.52 mg/L TOC. At such concentration, the C_{60} nanoparticles in the homoaggregate suspensions were found to be stable even at 500 mM NaCl, which was indicated by the flat homoaggregation profile presented in Figure 2.8a. Since the stock C_{60} suspension was the filtrate of two serial filtrations (0.22 μm and 0.10 μm), it was possible that the number of C_{60} nanoparticles used in the homoaggregate suspension (1.1 times dilution from the stock suspension) was very low. Therefore, the homoaggregation of C_{60} nanoparticles was possibly too slow to be detected within the time frame of the experiment (*i.e.*, 100 min).

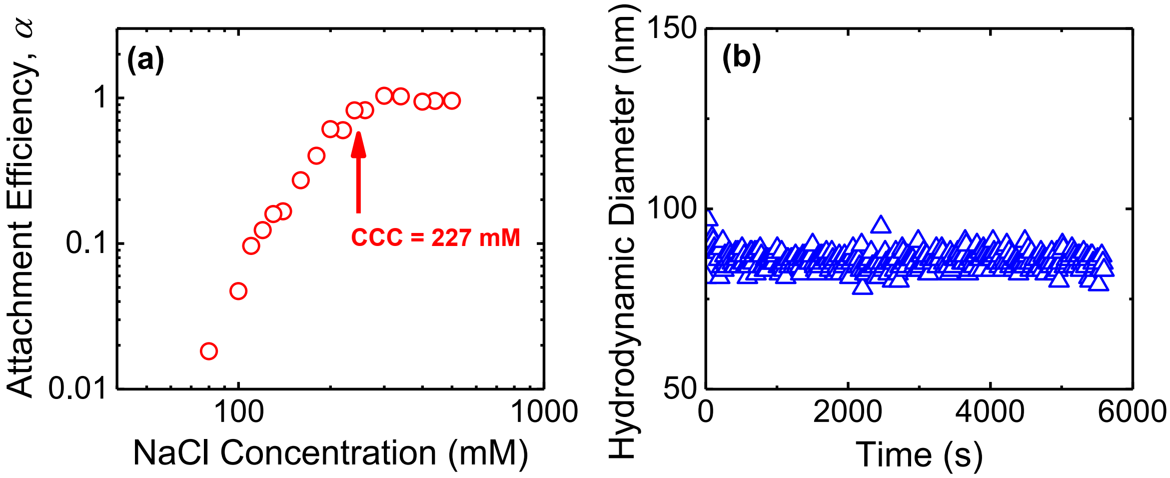

Figure 2.8. (a) Attachment efficiencies of GO nanosheets at different NaCl concentrations. GO nanosheet concentration was 0.58 mg/L TOC. (b) The homoaggregation profiles of C_{60} nanoparticles at a concentration of 1.52 mg/L TOC in 500 mM NaCl. The pH in (a) and (b) was 5.2.

2.3.4. CNTs and HemNPs Undergo Exclusive Heteroaggregation at Low NaCl Concentration

Figure 2.9 presents homoaggregation profiles of CNTs and HemNPs, as well as a heteroaggregation profile of CNTs and HemNPs at a CNT/HemNP ratio of 0.032. All the profiles were obtained at 0.1 mM NaCl. The HemNP homoaggregation experiment was conducted at the same nanoparticle concentration that was used for all the heteroaggregation experiments (*i.e.*, 0.44 mg/L). The CNT homoaggregation experiment was conducted at a concentration of 83 μg/L TOC, that is ca. 3 times of the highest CNT concentration used for the heteroaggregation experiments (*i.e.*, 28 μg/L TOC). It was necessary to employ an elevated CNT concentration for the CNT homoaggregation experiment because CNTs at a concentration of 28 μg/L TOC did not scatter sufficient light for accurate DLS measurements. Over the time period of 1500 s, no significant increase in hydrodynamic diameter of both CNTs and HemNPs was observed, indicating that these nanoparticles were stable to homoaggregation at 0.1 mM NaCl.

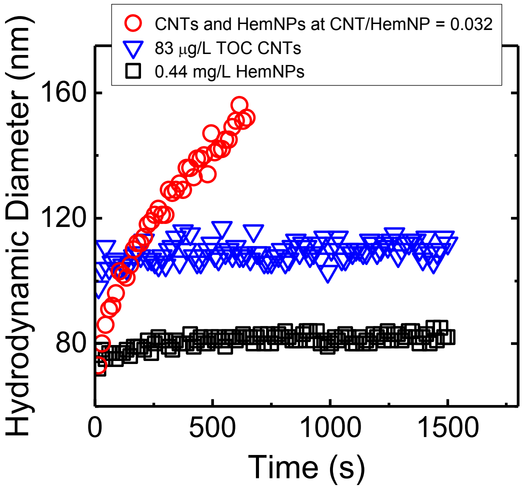

Figure 2.9. Homoaggregation profiles of CNTs and HemNPs, as well as heteroaggregation profile of CNTs and HemNPs at CNT/HemNP ratio of 0.032 (CNT concentration = 14 μg/L TOC and HemNP concentration = 0.44 mg/L). All the experiments were conducted at 0.1 mM NaCl and pH 5.2.

In contrast to the homoaggregation experiments, when CNTs were introduced into a HemNP suspension to form a binary suspension with final CNT and HemNP concentrations of 14 μg/L TOC and 0.44 mg/L, respectively, (*i.e.*, CNT/HemNP ratio = 0.032) at 0.1 mM NaCl, the hydrodynamic diameter increased significantly by almost 80 nm over a time period of only 645 s (Figure 2.9). Because the earlier homoaggregation experiments had shown that both nanoparticles were stable to homoaggregation, it is concluded that the substantial rise in hydrodynamic diameter of the aggregates in the binary system was a result of heteroaggregation that had occurred *exclusively*. Since the

CCCs of CNTs and HemNPs were much higher than 0.1 mM NaCl (Figure 2.6), both nanoparticles experienced a large electrostatic repulsion among the same type of nanoparticles that inhibited homoaggregation. Conversely, the low degree of charge screening at 0.1 mM NaCl allowed for favorable heteroaggregation between oppositely charged CNTs and HemNPs through both electrostatic and van der Waals attraction.

2.3.5. Influence of CNT/HemNP Ratio on Rates of Heteroaggregation

Heteroaggregation experiments were conducted over a range of nanoparticle relative concentrations in the presence of 0.1 mM NaCl. Representative heteroaggregation profiles at different CNT/HemNP ratios are shown in Figure 2.10a, while the rates of heteroaggregation are presented as a function of CNT/HemNP ratio in Figure 2.10b. For comparison, the homoaggregation rate of HemNPs under diffusion-limited conditions is also presented in Figure 2.10b. It was noted from Figure 2.10a that the initial hydrodynamic diameter of the binary suspension with CNT/HemNP ratio of 0.063, which was the highest concentration ratio used in the heteroaggregation experiments in this study, was equal to the hydrodynamic diameter of HemNPs (*ca.* 80 nm). This observation confirmed that HemNPs were the dominant light scatterers for all binary suspensions tested.

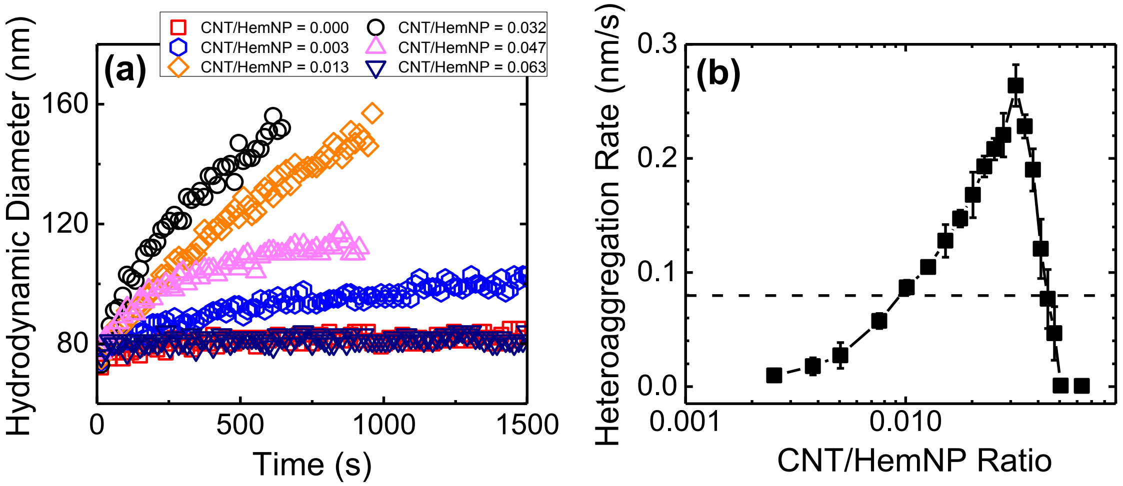

Figure 2.10. (a) Heteroaggregation profiles of CNTs and HemNPs at different CNT/HemNP ratios. (b) Heteroaggregation rate of CNTs and HemNPs as a function of CNT/HemNP ratio. Error bars represent standard deviations of at least three replicates. The dashed line represents the homoaggregation rate of HemNPs in the diffusion-limited regime. In (a) and (b), the HemNP concentration was fixed at 0.44 mg/L while the CNT concentration was varied.

At extremely low CNT/HemNP ratio (0.003), the HemNPs in the binary systems were relatively resistant to aggregation. As the relative concentration increased from 0.003 to 0.032, the rate of heteroaggregation increased correspondingly. At the optimal CNT/HemNP ratio of 0.032, the heteroaggregation rate reached a maximum that was *ca.* 3.3 times of the diffusion-limited homoaggregation rate of HemNPs. As the CNT/HemNP ratio was further increased above 0.032, the growth rates of heteroaggregates decreased dramatically until the growth rates approached zero at CNT/HemNP ratio of 0.050 and higher.

Gregory[44] observed a similar trend in the variation of heteroaggregation rates with colloidal/polymer ratio in suspensions that contained negatively charged polystyrene colloids and cationic dimethylaminoethyl methacrylate polymers. The heteroaggregation rate obtained at the optimal colloidal/polymer ratio under low ionic strength conditions was about twice the colloid homoaggregation rate in the diffusion-limited regime. Gregory[44] attributed the fast heteroaggregation to the formation of positively charged polymer patches on the colloid surface which resulted in long-range electrostatic attraction between oppositely charged polymer and uncovered patches on approaching colloids. In this CNT–HemNP system, however, CNTs are rigid[45, 46] and much longer than HemNPs, and thus are unlikely to form negatively charged patches on HemNPs.[44, 47] Hence, neither patchwise adsorption[35] nor charge neutralization[47] is expected to be the predominant mechanism resulting in the enhanced heteroaggregation of CNTs and HemNPs at the optimal CNT/HemNP ratio.

In order to investigate the effect of total nanoparticle concentrations on the heteroaggregation rate, additional heteroaggregation experiments were conducted at the optimal CNT/HemNP ratio, but at CNT and HemNP concentrations twice of their respective concentrations used for the previous heteroaggregation experiments (*i.e.*, 28 μg/L TOC CNTs and 0.88 mg/L HemNPs). The heteroaggregate rate obtained from the binary suspension with twice the original concentrations was 0.55 nm/s, which was twice the rate obtained for the original suspension (*i.e.*, 0.26 nm/s). Thus, when the CNT/HemNP ratio is maintained constant, the heteroaggregation rate is proportional to the total concentrations of CNTs and HemNPs.

2.3.6. Cryogenic TEM Imaging of CNT–HemNP Heteroaggregates

In order to elucidate the role of nanoparticle distributions on the heteroaggregation rates of CNTs and HemNPs, the structures of heteroaggregates were examined at different CNT/HemNP ratio by cryo-TEM. Unlike conventional TEM, cryo-TEM does not require the drying of the sample on a TEM grid which will result in artifacts, such as deformation of aggregates and agglomeration of particles and their aggregates.[48, 49] Instead, a grid with a thin film of colloidal suspension is rapidly plunged into liquid ethane (boiling point = −88.6°C[50]) to freeze the colloidal sample. The instantaneous freezing of the film of suspension (cooling rate ca. 10^5 K/s[51]) ensures that the structure of heteroaggregates in solution is preserved with no alteration.

At a low CNT/HemNP ratio of 0.0023, isolated HemNPs and some small heteroaggregates were observed in the cryo-TEM images. A representative image of a CNT–HemNP heteroaggregate formed at this ratio is presented in Figure 2.11a. In this image, a carbon lace (carbon film) separates two holes, one of which contains a frozen film of heteroaggregate suspension (ice layer) and the other that does not contain a film of suspension (empty region). Because the heteroaggregate sample was deposited on a grid coated with a lacey carbon film, a film of heteroaggregate suspension should form in some of the holes of the carbon film when the sample is blotted/frozen. Since the heteroaggregate is immobilized in an ice layer contained within the holes of the carbon film (instead of being dried and deposited on a carbon film, as is often the case for samples prepared for conventional TEM imaging), the structure of the heteroaggregate is expected to be representative of the heteroaggregate that is suspended in solution.

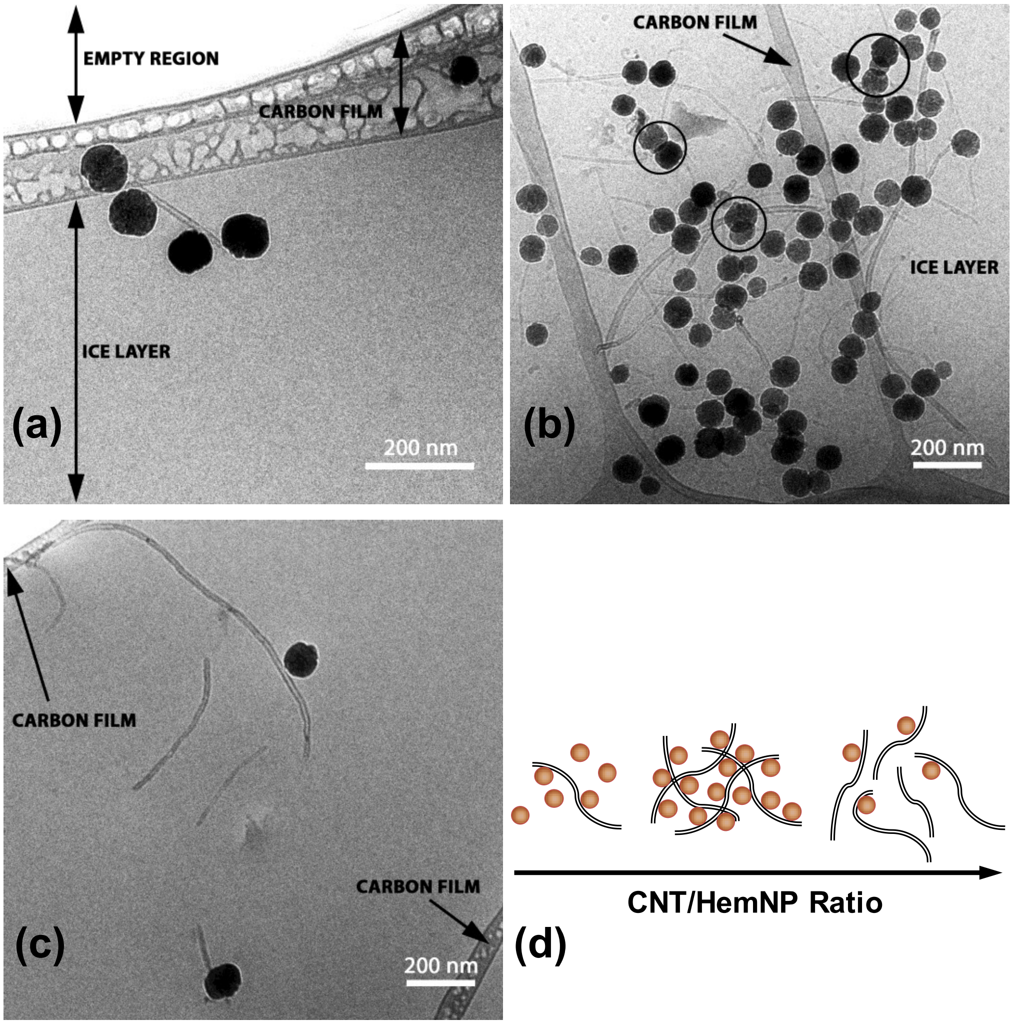

Figure 2.11. Representative cryo-TEM images of heteroaggregates at (a) low CNT/HemNP ratio (0.003), (b) optimal CNT/HemNP ratio (0.032), and (c) high CNT/HemNP (0.127) after *ca.* 15 min of heteroaggregation. (d) Proposed heteroaggregation mechanisms at different CNT/HemNP ratios.

At the optimal CNT/HemNP ratio of 0.032, HemNPs were interconnected by multiple strands of CNTs to form extensive and open heteroaggregate structures. A representative image of a heteroaggregate in a frozen film formed over three holes is presented in Figure 2.11b. It is important to note that the formation of the film of heteroaggregate suspension on the lacey carbon grid likely caused the heteroaggregates to collapse into flattened structures with thicknesses similar to that of the film of suspension. It is evident from the "overlapping" of HemNPs within the heteroaggregates (circles in Figure 2.11b) that about 2 or 3 HemNPs can stack above one another within the ice film, implying that the film thickness was *ca.* 200 nm. Nevertheless, the flattened structures are still much more representative of the original structures in solution compared to heteroaggregates that have been dried on a TEM grid. Representative heteroaggregates prepared at a high CNT/HemNP ratio of 0.127 are presented in Figure 2.11c. Similar to the heteroaggregates in Figure 2.10a and b, the heteroaggregates were entrapped in a film of frozen solution that was formed within a hole of a lacey carbon film. These heteroaggregates were frequently observed to comprise a CNT and a HemNP.

2.3.7. Proposed Heteroaggregation Mechanisms of CNTs and HemNPs

On the basis of the results from EPM and time-resolved DLS measurements, as well as the observations from cryo-TEM imaging, the mechanisms for heteroaggregation of CNTs and HemNPs at different CNT/HemNP ratio were proposed (Figure 2.11d). At all relative concentrations, HemNPs and CNTs are resistant to homoaggregation due to electrostatic repulsion. At extremely low relative concentrations of CNTs and HemNPs, HemNPs greatly outnumber CNTs. Thus, the chances of a CNT encountering HemNPs are extremely high. Because of the electrostatic and van der Waals attraction between a CNT and a HemNP, every collision between these oppositely charged nanoparticles will initially result in an attachment. However, as multiple HemNPs are attached to a single CNT, less space along the nanotube is available for more HemNPs to attach to. At this point in time, the strand of nanotube that is now lined with HemNPs practically becomes a stable heteroaggregate. This heteroaggregate repels other HemNPs, as well as other

CNTs that are lined with HemNPs, and ceases to grow in size. At such a low CNT/HemNP ratio (*e.g.*, 0.003), however, the occurrence of heteroaggregation is relatively rare due to the low concentration of CNTs. Thus, even though a few heteroaggregates were observed under cryo-TEM, negligible change in hydrodynamic diameter of the suspension was detected through time-resolved DLS.

As the CNT/HemNP ratio increases, the opportunities for HemNPs to encounter CNTs increase correspondingly. Because of the large aspect ratio of CNTs, the nanotubes can effectively bridge HemNPs, akin to the bridging of colloidal particles by long-chain polymers or polyelectrolytes.[35, 52] Since most of the CNTs are longer than the theoretical Debye length at an ionic strength of 0.1 mM (*i.e.*, ca. 30 nm),[35, 53] the bridging of HemNPs by CNTs can occur even before HemNPs approach close enough to experience significant electrostatic repulsion. This bridging mechanism results in the formation of an extensive network of CNTs and HemNPs. Therefore, the growth rate of heteroaggregates increases as the relative concentration initially increases until it reaches a maximum at the optimal CNT/HemNP ratio of 0.032.

As the CNT/HemNP ratio of CNTs and HemNPs is further increased, the number concentration of CNTs greatly exceeds that of HemNPs, resulting in every HemNP to attach to a CNT to form a composite nanoparticle. The negatively charged “nanotubular arms” of a composite nanoparticle can repel the arms of other approaching composite nanoparticles, as well as isolated CNTs, and prevent their attachment to the composite nanoparticle. Since the arms are considerably longer than the hematite constituent of a composite nanoparticle, repulsion between the arms is likely to dominate the interaction between composite nanoparticles. The growth of heteroaggregates is thus inhibited through this blocking mechanism and is reflected by the non-detectable change in hydrodynamic diameter of the heteroaggregates at CNT/HemNP ratio above 0.050 (Figure 2.10b).

2.3.8. Influence of Humic Acid on Heteroaggregation Rates of CNTs and HemNPs

In order to investigate the effects of natural organic matter on the heteroaggregation behavior of CNTs and HemNPs, heteroaggregation experiments were conducted at four SRHA concentrations (0.15, 0.20, 0.25, and 500.00 μg/L TOC). These highly diluted SRHA solutions were prepared through serial dilutions of the SRHA stock solution. For these experiments, the hematite concentration was kept constant at 0.44 mg/L, while the CNT concentration was varied from 1 to 28 μg/L TOC. The growth rates of aggregates at the four SRHA concentrations are presented as functions of CNT/HemNP ratio in Figure 2.12a. The heteroaggregation rates obtained in the absence of SRHA are also included for comparison.

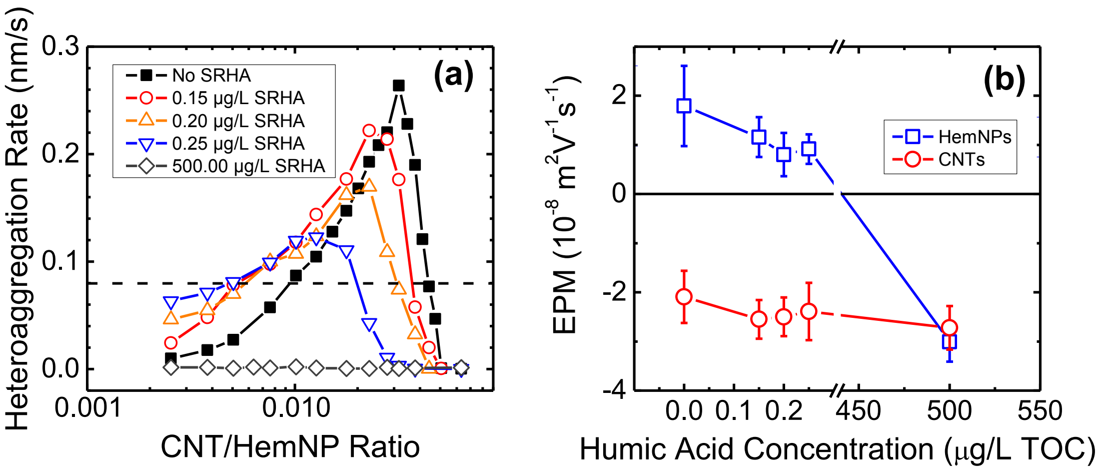

Figure 2.12. (a) Heteroaggregation rate of CNTs and HemNPs as a function of CNT/HemNP ratio at different Suwannee River humic acid (SRHA) concentrations. The rates in the absence of humic acid are reproduced from Figure 2.9b. The dash line represents the homoaggregation rate of HemNPs in the diffusion-limited regime. The HemNP concentration was fixed at 0.44 mg/L while the CNT concentration was varied. (b) Electrophoretic mobilities (EPMs) of CNTs and HemNPs at 0.1 mM NaCl and pH 5.2 in the presence of SRHA.

Generally, the trends in the variation of the aggregate growth rate with CNT/HemNP ratio at different SRHA concentrations are similar to that in the absence of humic acid. Specifically, the aggregate growth rate increases with an initial increase in CNT/HemNP ratio, reaches a maximum at an optimal CNT/HemNP ratio, and then decreases as the CNT/HemNP ratio is further increased. It is also observed that as the SRHA concentration increases, the maximum aggregate growth rate decreases. Similarly, within the higher range of CNT/HemNP ratio (> 0.02), an increase in SRHA concentration from 0 to 500.00 μg/L TOC resulted in a decrease in the aggregate growth rate at each CNT/HemNP ratio. Within the lower range of CNT/HemNP ratio (< 0.01), in contrast, the presence of SRHA with concentrations between 0.15 and 0.25 μg/L TOC elevated the aggregate growth rate at each CNT/HemNP ratio. At the highest SRHA concentration employed (500.00 μg/L TOC), no increase in aggregate size was detected regardless of the CNT/HemNP ratio.

In order to elucidate the effect of humic acid on the heteroaggregation behavior of CNTs and HemNPs, the EPMs of both nanoparticles were measured at the same SRHA concentrations employed for the heteroaggregation experiments (Figure 2.12b). As the SRHA concentration was increased from 0 to 0.25 μg/L TOC, the EPMs of HemNPs became noticeably less positive due to the increasing adsorption of humic acid macromolecules that contained negatively charged carboxyl functional groups. When the SRHA concentration was further raised to 500.00 μg/L TOC, the EPM of HemNPs decreased to -3.01×10^{-8} $m^2/(V \cdot s)$, indicating that sufficient humic acid macromolecules had adsorbed on the HemNPs to cause charge reversal to take place. The results imply that HemNPs were not completely coated with humic acid at SRHA concentrations lower than 0.25 μg/L TOC and the fraction of HemNP surface that remained uncoated decreased with increasing humic acid concentrations. At the highest SRHA concentration of 500.00 μg/L TOC, a significant fraction of HemNP surface was likely to be coated with humic acid. Conversely, an increase in SRHA concentration from 0 to 500.00 μg/L TOC had no significant effect on the EPM of CNTs, which was also observed by Saleh et al.,[11] possibly because the charge densities of CNTs and humic acid were very similar.

On the basis of the results from EPM measurements, an increase in SRHA concentration from 0 to 0.25 μg/L TOC will result in a decrease in the uncoated, positively charged HemNP surface that CNTs can attach to through favorable electrostatic interaction. Within the higher range of CNT/HemNP ratio (> 0.02), the reduction in favorable electrostatic interaction between CNTs and HemNPs with increasing humic acid concentration was evident from the decrease in the aggregate growth rate at each CNT/HemNP ratio (Figure 2.12a). In this regime in which CNT concentrations were relatively high, HemNPs were more likely to encounter CNTs than other HemNPs. Thus, the growth in aggregate size detected through DLS can be attributed to heteroaggregation.

Within the lower range of CNT/HemNP ratio (< 0.01), the HemNP concentrations were relatively high and HemNP–HemNP interactions were expected to dominate in the binary systems. The increase in SRHA concentration from 0 to 0.25 μg/L TOC will result in an increase in the HemNP surface that will be coated with the macromolecules to form negatively charged patches. Thus, homoaggregation of HemNPs may occur through the attraction of oppositely charged patches on approaching nanoparticles and contribute to the growth in aggregate size that was detected through DLS at the lower range of relative concentration (Figure 2.12a).

To verify that homoaggregation of HemNPs can occur at low concentrations of SRHA, additional time-resolved DLS measurements were conducted on suspensions containing only HemNPs at SRHA concentrations of 0.15, 0.20, and 0.25 μg/L TOC (Figure 2.13). At all three humic acid concentrations, the hydrodynamic diameter increased slightly from 80 nm to 90–100 nm over a time period of 2000 s, indicating that slow homoaggregation took place under these conditions. When the same experiments were conducted in the presence of CNTs at the lowest CNT/HemNP ratio used (*i.e.*, 0.003), the aggregate growth rates were considerably higher than those in the absence of CNTs. Over the same time period, the hydrodynamic diameters increased to 115–170 nm in the presence of CNTs and humic acid (Figure 2.13). The addition of humic acid does not cause CNTs to undergo homoaggregation since the EPMs of CNTs were found to be unchanged (Figure 2.12b). We therefore conclude that the faster aggregate growth in the presence of CNTs is due to heteroaggregation of CNTs and HemNPs that had occurred concomitantly with the slow homoaggregation of HemNPs. This observation also confirms that both homoaggregation and heteroaggregation contributed to the growth in aggregate size detected through time-resolved DLS at the lower CNT/HemNP ratio (< 0.01). Within this lower range of CNT/HemNP ratio, the faster aggregate growth observed in the presence of humic acid, as shown in Figure 2.12a, may be due to the bridging of *HemNP homoaggregates* by CNTs. In contrast, the aggregate growth in the absence of humic acid is slower since the bridging of *isolated HemNPs* by CNTs is more likely to occur.

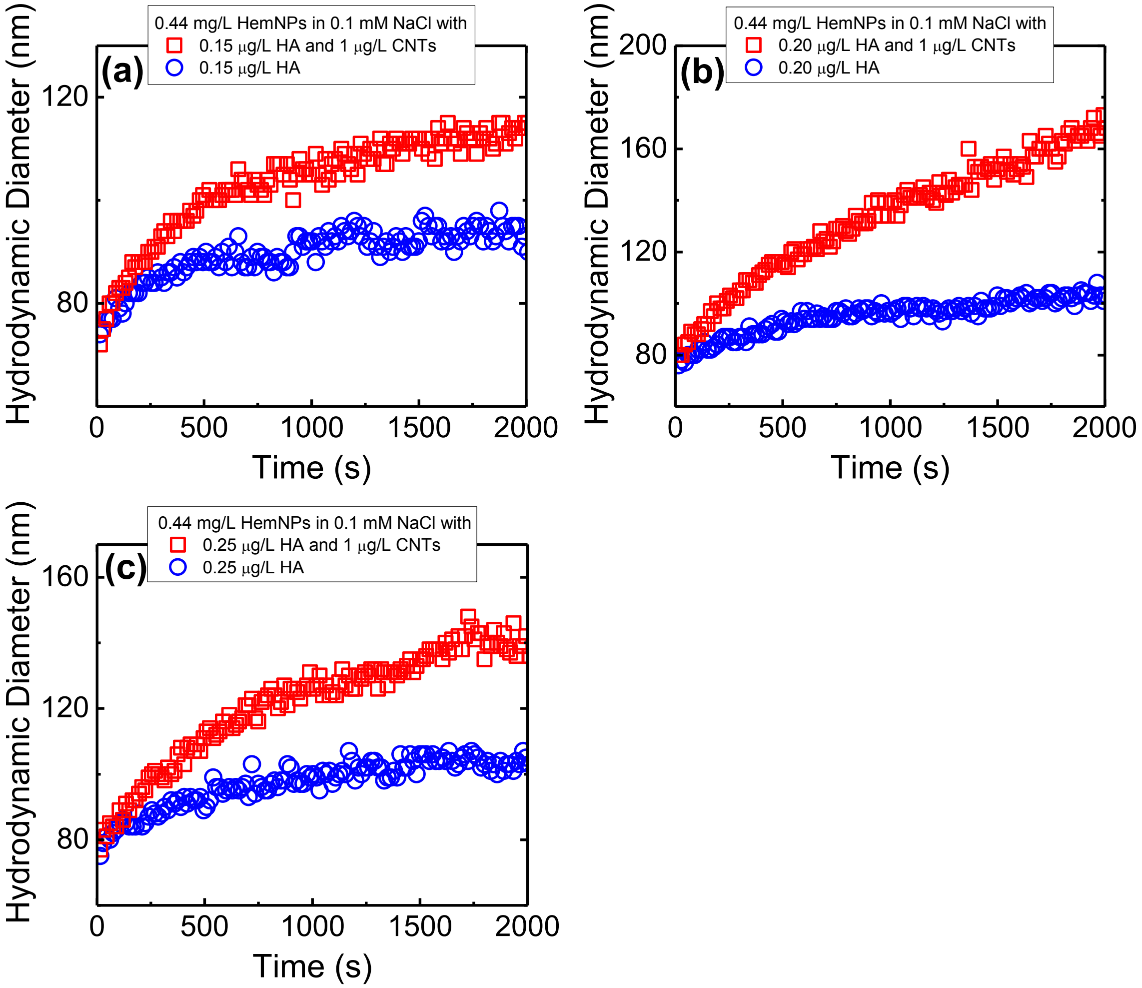

Figure 2.13. Influence of humic acid (SRHA) on the aggregation rates of HemNPs in the absence and presence of CNTs at 0.1 mM NaCl and pH 5.2. The SRHA concentrations are (a) 0.15 µg/L TOC, (b) 0.20 µg/L TOC, and (c) 0.25 µg/L TOC. For all experiments, the concentration of HemNPs is 0.44 mg/L. For experiments performed in the presence of CNTs, the CNT concentration is 1 µg/L TOC, resulting in a CNT/HemNP ratio of 0.003.

At the highest SRHA concentration of 500.00 µg/L, both HemNPs and CNTs were negatively charged (Figure 2.12b). Thus, they experienced significant electrostatic and electrosteric repulsion[35, 37, 54] that inhibited both homoaggregation and heteroaggregation. The stabilization of the binary systems is reflected by the non-detectable growth in aggregate size across the entire range of relative concentration studied (Figure 2.12a).

2.3.9. Heteroaggregation Behavior of GO Nanosheets and C_{60} Nanoparticles with HemNPs

Similar to the heteroaggregation experiments between CNTs and HemNPs, the heteroaggregation of GO nanosheets and C_{60} nanoparticles with HemNPs were conducted at pH 5.2 ± 0.2 and 0.1 mM NaCl. At this condition, these nanomaterials were stable to homoaggregation (Figure 2.6 and Figure 2.8) and the heteroaggregation occurred exclusively. The HemNP concentration was also fixed at 0.44 mg/L while the concentrations of GO nanosheets and nC_{60} nanoparticles were varied in the range of 2 – 466 μg/L TOC and 42 – 334 μg/L TOC, respectively. Similar to CNT–HemNP binary suspensions, HemNPs were also the dominant light scatterers in GO–HemNP and C_{60}–HemNP binary suspensions because the scattered light intensity from HemNPs was observed to be *ca.* 20 times higher than that from GO and C_{60} in all heteroaggregation experiments.

The heteroaggregation rates between (i) GO nanosheets and HemNPs and (ii) C_{60} nanoparticles and HemNPs obtained at different GO/HemNP and C_{60}/HemNP ratios (concentration ratios) are presented in Figure 2.14. The heteroaggregation rates between CNTs and HemNPs, as well as the homoaggregation of 0.44 mg/L HemNPs in diffusion-limited regime are also presented in this figure. It was observed from Figure 2.14 that the trends in the variation of heteroaggregation rate with concentration ratio in all three heteroaggregate systems (*i.e.*, CNTs + HemNPs, GO nanosheets + HemNPs, and C_{60} nanoparticles + HemNPs) were similar. An initial increase in the concentration ratio resulted in a corresponding increase in the heteroaggregation rate. After reaching the highest value at an optimal concentration ratio, the heteroaggregation rate decreased when the relative concentration ratio was further increased.

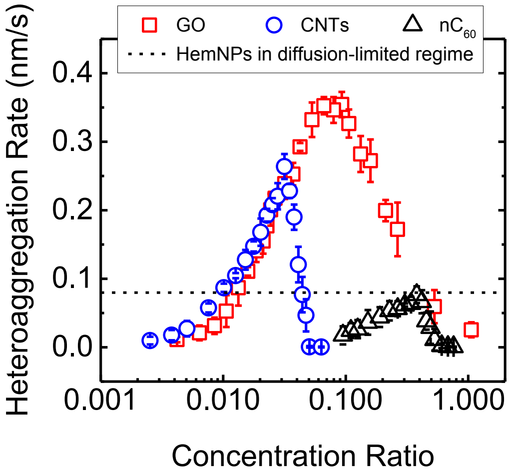

Figure 2.14. Heteroaggregation rates of CNTs, GO nanosheets, and C_{60} nanoparticles with HemNPs at different mass concentration ratios of carbon-based nanomaterials and HemNPs. The data for heteroaggregation between CNTs and HemNPs were reproduced from Figure 2.10. Error bars represent standard deviations of at least three replicates. The dashed line represents the homoaggregation rate of HemNPs in the diffusion-limited regime. The HemNP concentration was fixed at 0.44 mg/L. The GO, CNTs, and C_{60} concentrations were 2–466, 1–28, and 42–344 μg/L TOC, respectively.

At their respective optimal concentration ratios, the maximum heteroaggregation rate in the binary systems containing GO nanosheets was 0.35 nm/s while the maximum rate in the systems containing CNTs was 0.26 nm/s. In addition, the maximum heteroaggregation rate in system containing C_{60} was 0.08 nm/s, which was identical to the homoaggregation rate of HemNPs in diffusion-limited regime. It is interesting that despite the difference in the dimensionality of the three carbon nanomaterials, the heteroaggregation rate trends look the same, which indicates that the mechanisms of heteroaggregation for C_{60} nanoparticles and GO nanosheets may be similar to those for

CNTs. Presently, it is still not clear whether the differences in the maximum heteroaggregation rates at optimal concentration ratios are caused by dimensionality or size effects. Cryo-TEM imaging of GO–HemNP and C_{60}–HemNP heteroaggregates prepared at different concentration ratios may elucidate mechanisms for heteroaggregation. This work, however, is outside the scope of the dissertation and is recommended for future work.

2.3.10. Environmental Implications

Time-resolved DLS measurements show that concentration ratio has a significant influence on the heteroaggregation behavior of carbon-based nanomaterial and HemNPs. Hence, it is critical to consider this parameter in the modeling and prediction of the fate and transport of CNTs, as well as other carbon-based nanomaterials (*e.g.*, GO nanosheets and C_{60} nanoparticles) in natural aquatic systems. The presence of humic acid at the highest concentration employed in this study (500.00 μg/L TOC) was found to completely inhibit CNT–HemNP heteroaggregation regardless of CNT/HemNP ratio. Because the studied humic acid concentrations are smaller than those typically found in freshwater systems, CNTs are anticipated to be mobile in these environments. Due to the wide variety of naturally occurring colloids present in natural aquatic systems, further heteroaggregation studies between CNTs and other classes of naturally occurring colloids will be required. In the present study, CNTs with relatively high oxygen content (10.3 %) are employed. Additional investigation on binary systems comprising lowly oxidized CNTs and naturally occurring colloids in which homoaggregation and heteroaggregation are expected to occur simultaneously will be needed. Moreover, the structures of GO nanosheet or C_{60} nanoparticle heteroaggregates formed at different concentration ratios are needed to be evaluated through Cryo-TEM imaging to find the effect of dimensionality on the heteroaggregation mechanisms.

2.4. Refereces

1. Endo, M.; Hayashi, T.; Kim, Y. A.; Terrones, M.; Dresselhaus, M. S., Applications of carbon nanotubes in the twenty-first century. *Philos T Roy Soc A* **2004,** *362*, (1823), 2223-2238.

2. Aitken, R. J.; Chaudhry, M. Q.; Boxall, A. B. A.; Hull, M., Manufacture and use of nanomaterials: current status in the UK and global trends. *Occup Med-Oxford* **2006,** *56*, (5), 300-306.

3. Paradise, M.; Goswami, T., Carbon nanotubes - Production and industrial applications. *Mater Design* **2007,** *28*, (5), 1477-1489.

4. Kumar, A.; Zhou, C. W., The Race To Replace Tin-Doped Indium Oxide: Which Material Will Win? *ACS Nano* **2010,** *4*, (1), 11-14.

5. Transparent conductive films. http://www.unidym.com/products/transparent.html (07/31/2011),

6. Amroy. http://www.amroy.fi/index.php (07/31/2011),

7. Petersen, E. J.; Zhang, L.; Mattison, N. T.; O'Carroll, D. M.; Whelton, A. J.; Uddin, N.; Nguyen, T.; Huang, Q.; Henry, T. B.; Holbrook, R. D.; Chen, K. L., Potential Release Pathways, Environmental Fate, And Ecological Risks of Carbon Nanotubes. *Environ Sci Technol* **2011,** *45*, (23), 9837-9856.

8. Kang, S.; Herzberg, M.; Rodrigues, D. F.; Elimelech, M., Antibacterial effects of carbon nanotubes: Size does matter. *Langmuir* **2008,** *24*, (13), 6409-6413.

9. Johnston, H. J.; Hutchison, G. R.; Christensen, F. M.; Peters, S.; Hankin, S.; Aschberger, K.; Stone, V., A critical review of the biological mechanisms underlying the in vivo and in vitro toxicity of carbon nanotubes: The contribution of physico-chemical characteristics. *Nanotoxicology* **2010,** *4*, (2), 207-246.

10. Kang, S.; Mauter, M. S.; Elimelech, M., Physicochemical determinants of multiwalled carbon nanotube bacterial cytotoxicity. *Environ Sci Technol* **2008,** *42*, (19), 7528-7534.

11. Saleh, N. B.; Pfefferle, L. D.; Elimelech, M., Aggregation Kinetics of Multiwalled Carbon Nanotubes in Aquatic Systems: Measurements and Environmental Implications. *Environ Sci Technol* **2008,** *42*, (21), 7963-7969.

12. Smith, B.; Wepasnick, K.; Schrote, K. E.; Cho, H. H.; Ball, W. P.; Fairbrother, D. H., Influence of Surface Oxides on the Colloidal Stability of Multi-Walled Carbon Nanotubes: A Structure-Property Relationship. *Langmuir* **2009,** *25*, (17), 9767-9776.

13. Smith, B.; Wepasnick, K.; Schrote, K. E.; Bertele, A. H.; Ball, W. P.; O'Melia, C.; Fairbrother, D. H., Colloidal Properties of Aqueous Suspensions of Acid-Treated, Multi-Walled Carbon Nanotubes. *Environ Sci Technol* **2009,** *43*, (3), 819-825.

14. Petosa, A. R.; Jaisi, D. P.; Quevedo, I. R.; Elimelech, M.; Tufenkji, N., Aggregation and Deposition of Engineered Nanomaterials in Aquatic Environments: Role of Physicochemical Interactions. *Environ Sci Technol* **2010,** *44*, (17), 6532-6549.

15. Yi, P.; Chen, K. L., Influence of Surface Oxidation on the Aggregation and Deposition Kinetics of Multiwalled Carbon Nanotubes in Monovalent and Divalent Electrolytes. *Langmuir* **2011,** *27*, (7), 3588-3599.

16. Buffle, J.; Wilkinson, K. J.; Stoll, S.; Filella, M.; Zhang, J. W., A generalized description of aquatic colloidal interactions: The three-colloidal component approach. *Environ Sci Technol* **1998,** *32*, (19), 2887-2899.

17. Yu, W. L.; Matijevic, E.; Borkovec, M., Absolute heteroaggregation rate constants by multiangle static and dynamic light scattering. *Langmuir* **2002,** *18*, (21), 7853-7860.

18. Lin, W.; Kobayashi, M.; Skarba, M.; Nu, C. D.; Galletto, P.; Borkovec, M., Heteroaggregation in binary mixtures of oppositely charged colloidal particles. *Langmuir* **2006,** *22*, (3), 1038-1047.

19. Buffle, J.; Leppard, G. G., Characterization of Aquatic Colloids and Macromolecules .1. Structure and Behavior of Colloidal Material. *Environ Sci Technol* **1995,** *29*, (9), 2169-2175.

20. Wilkinson, K. J.; Stoll, S.; Buffle, J., Characterization of Nom-Colloid Aggregates in Surface Waters - Coupling Transmission Electron-Microscopy Staining Techniques and Mathematical-Modeling. *Fresen J Anal Chem* **1995,** *351*, (1), 54-61.

21. Chen, K. L.; Smith, B. A.; Ball, W. P.; Fairbrother, D. H., Assessing the colloidal properties of engineered nanoparticles in water: case studies from fullerene C(60) nanoparticles and carbon nanotubes. *Environ Chem* **2010,** *7*, (1), 10-27.

22. Scheibe, B.; Borowiak-Palen, E.; Kalenczuk, R. J., Oxidation and reduction of multiwalled carbon nanotubes - preparation and characterization. *Mater Charact* **2010,** *61*, (2), 185-191.

23. Du, F. P.; Wang, J. J.; Tang, C. Y.; Tsui, C. P.; Zhou, X. P.; Xie, X. L.; Liao, Y. G., Water-soluble graphene grafted by poly(sodium 4-styrenesulfonate) for enhancement of electric capacitance. *Nanotechnology* **2012,** *23*, (47).

24. El Achaby, M.; Arrakhiz, F. Z.; Vaudreuil, S.; Essassi, E. M.; Qaiss, A., Piezoelectric beta-polymorph formation and properties enhancement in graphene oxide - PVDF nanocomposite films. *Applied Surface Science* **2012,** *258*, (19), 7668-7677.

25. Liu, J.; Jeong, H.; Liu, J.; Lee, K.; Park, J. Y.; Ahn, Y. H.; Lee, S., Reduction of functionalized graphite oxides by trioctylphosphine in non-polar organic solvents. *Carbon* **2010,** *48*, (8), 2282-2289.

26. Liu, J. C.; Bai, H. W.; Wang, Y. J.; Liu, Z. Y.; Zhang, X. W.; Sun, D. D., Self-Assembling TiO2 Nanorods on Large Graphene Oxide Sheets at a Two-Phase Interface and Their Anti-Recombination in Photocatalytic Applications. *Adv Funct Mater* **2010,** *20*, (23), 4175-4181.

27. Mei, X. G.; Ouyang, J. Y., Ultrasonication-assisted ultrafast reduction of graphene oxide by zinc powder at room temperature. *Carbon* **2011,** *49*, (15), 5389-5397.

28. Chen, K. L.; Elimelech, M., Aggregation and Deposition Kinetics of Fullerene (C60) Nanoparticles. *Langmuir* **2006,** *22*, (26), 10994-11001.

29. Chen, K. L.; Elimelech, M., Influence of humic acid on the aggregation kinetics of fullerene (C-60) nanoparticles in monovalent and divalent electrolyte solutions. *Journal of Colloid and Interface Science* **2007,** *309*, (1), 126-134.

30. Chen, K. L.; Elimelech, M., Interaction of Fullerene (C-60) Nanoparticles with Humic Acid and Alginate Coated Silica Surfaces: Measurements, Mechanisms, and Environmental Implications. *Environ Sci Technol* **2008,** *42*, (20), 7607-7614.

31. Chen, K. L.; Elimelech, M., Relating Colloidal Stability of Fullerene (C-60) Nanoparticles to Nanoparticle Charge and Electrokinetic Properties. *Environ Sci Technol* **2009,** *43*, (19), 7270-7276.

32. Mylon, S. E.; Chen, K. L.; Elimelech, M., Influence of natural organic matter and ionic composition on the kinetics and structure of hematite colloid aggregation: Implications to iron depletion in estuaries. *Langmuir* **2004,** *20*, (21), 9000-9006.

33. Chen, K. L.; Mylon, S. E.; Elimelech, M., Aggregation kinetics of alginate-coated hematite nanoparticles in monovalent and divalent electrolytes. *Environ Sci Technol* **2006,** *40*, (5), 1516-1523.

34. Cho, H. H.; Smith, B. A.; Wnuk, J. D.; Fairbrother, D. H.; Ball, W. P., Influence of surface oxides on the adsorption of naphthalene onto multiwalled carbon nanotubes. *Environ Sci Technol* **2008,** *42*, (8), 2899-2905.

35. Elimelech, M.; Gregory, J.; Jia, X.; Williams, R. A., *Particle Deposition and Aggregation: Measurement, Modelling and Simulation*. Butterworth-Heinemann: Oxford, England, 1995.

36. Holthoff, H.; Egelhaaf, S.; Borkovec, M.; Schurtenberger, P.; Sticher, H., Coagulation rate measurements of colloidal particles by simultaneous static and dynamic light scattering. *Langmuir* **1996,** *12*, (23), 5541-5549.

37. Huynh, K. A.; Chen, K. L., Aggregation Kinetics of Citrate and Polyvinylpyrrolidone Coated Silver Nanoparticles in Monovalent and Divalent Electrolyte Solutions. *Environ Sci Technol* **2011**, (45), 5564-5571.

38. Ferretti, R.; Stoll, S.; Zhang, J. W.; Buffle, J., Flocculation of hematite particles by a comparatively large rigid polysaccharide: schizophyllan. *Journal of Colloid and Interface Science* **2003,** *266*, (2), 328-338.

39. Carey, F. A.; Sundberg, R. J., *Advanced Organic Chemistry Part B: Reactions and Synthesis*. Springer US: 2007.

40. Schwarzenbach, R. P.; Gschwend, P. M.; Imboden, D. M., *Environmental Organic Chemistry*. John Wiley & Sons, Inc: 2003.

41. Zhang, J. W.; Buffle, J., Kinetics of Hematite Aggregation by Polyacrylic-Acid - Importance of Charge Neutralization. *Journal of Colloid and Interface Science* **1995,** *174*, (2), 500-509.

42. Chen, K. L.; Mylon, S. E.; Elimelech, M., Enhanced aggregation of alginate-coated iron oxide (hematite) nanoparticles in the presence of calcium, strontium, and barium cations. *Langmuir* **2007,** *23*, (11), 5920-5928.

43. Wu, L.; Liu, L.; Gao, B.; Munoz-Carpena, R.; Zhang, M.; Chen, H.; Zhou, Z.; Wang, H., Aggregation kinetics of graphene oxides in aqueous solutions: experiments, mechanisms, and modeling. *Langmuir* **2013,** *29*, (49), 15174-81.

44. Gregory, J., Rates of Flocculation of Latex Particles by Cationic Polymers. *Journal of Colloid and Interface Science* **1973,** *42*, (2), 448-456.

45. Treacy, M. M. J.; Ebbesen, T. W.; Gibson, J. M., Exceptionally high Young's modulus observed for individual carbon nanotubes. *Nature* **1996,** *381*, (6584), 678-680.

46. Falvo, M. R.; Clary, G. J.; Taylor, R. M.; Chi, V.; Brooks, F. P.; Washburn, S.; Superfine, R., Bending and buckling of carbon nanotubes under large strain. *Nature* **1997,** *389*, (6651), 582-584.

47. Kleimann, J.; Gehin-Delval, C.; Auweter, H.; Borkovec, M., Super-stoichiometric charge neutralization in particle-polyelectrolyte systems. *Langmuir* **2005,** *21*, (8), 3688-3698.

48. Talmon, Y., Staining and Drying-Induced Artifacts in Electron-Microscopy of Surfactant Dispersions. *Journal of Colloid and Interface Science* **1983,** *93*, (2), 366-382.

49. Kilpatrick, P. K.; Miller, W. G.; Talmon, Y., Staining and Drying-Induced Artifacts in Electron-Microscopy of Surfactant Dispersions .2. Change in Phase-Behavior Produced by Variation in Ph Modifiers, Stain, and Concentration. *Journal of Colloid and Interface Science* **1985,** *107*, (1), 146-158.

50. Cui, H.; Hodgdon, T. K.; Kaler, E. W.; Abezgauz, L.; Danino, D.; Lubovsky, M.; Talmon, Y.; Pochan, D. J., Elucidating the assembled structure of amphiphiles in solution via cryogenic transmission electron microscopy. *Soft Matter* **2007,** *3*, (8), 945-955.

51. Siegel, D. P.; Green, W. J.; Talmon, Y., The mechanism of lamellar-to-inverted hexagonal phase transitions: a study using temperature-jump cryo-electron microscopy. *Biophysical Journal* **1994,** *66*, (2, Part 1), 402-414.

52. Hunter, R. J., *Foundations of Colloid Science*. Oxford University Press: Oxford, England, 2002.

53. Israelachvili, J., *Intermolecular and Surface Forces*. Academic Press: London, England, 1991.

54. Stankus, D. P.; Lohse, S. E.; Hutchison, J. E.; Nason, J. A., Interactions between Natural Organic Matter and Gold Nanoparticles Stabilized with Different Organic Capping Agents. *Environmental Science & Technology* **ASAP**.

Chapter 3. Disaggregation of Heteroaggregates Composed of Multiwalled Carbon Nanotubes and Hematite Nanoparticles*

---

*This chapter was submitted as a manuscript with co-author Kai Loon Chen to *Environmental Science: Processes and Impacts*. Co-author Kai Loon Chen helped with data interpretation and manuscript editing.

3.1. Introduction

Carbon nanotubes (CNTs) are cylindrical nanomaterials (micrometer-scale in length and nanometer-scale in diameter) that comprise coaxial tube(s) of carbon atoms in a helical arrangement.[1] Because of their unique molecular structure, CNTs have extraordinary physical, chemical, and electrical properties.[2, 3] Single-walled CNTs have been reported to have high Young's modulus and tensile strength.[3, 4] In addition, CNTs can be either metallic or semiconducting, depending on their chirality.[3] Currently, CNTs are already used in batteries, composite materials, and specialized medical appliances.[5] They potentially can also be employed in power transmission cables, flexible electronics, and membranes for water filtration.[5]

The increasing manufacturing and use of CNTs will inevitably result in the release of these nanomaterials into the environment.[6, 7] The environmental fate and transport of CNTs, as well as the toxicity of CNTs in aqueous systems,[8, 9] are strongly dependent on their aggregation and disaggregation behavior.[7] In natural and subsurface waters, the concentration of CNTs is likely to be much lower than that of naturally occurring colloids. As a result, CNTs have a greater opportunity to undergo heteroaggregation (or aggregation between different types of colloids) with natural occurring colloids than homoaggregation (or aggregation among the same type of colloids) with other CNTs.[7, 10-12] These aggregation processes are expected to reduce the mobility of CNTs in the environment.

The homoaggregation of CNTs is relatively well studied.[12-15] CNT homoaggregation has been demonstrated to qualitatively follow the Derjaguin–Landau–Verwey–Overbeek (DLVO) theory and their colloidal stability is strongly dependent on their surface chemistry.[12-15] Recently, several studies have been conducted on the heteroaggregation of CNTs with other types of colloids.[12, 16] As presented in Chapter 2, the bridging of positively charged HemNPs by negatively charged CNT strands was observed to be a key mechanism for the heteroaggregation of these nanoparticles. Similarly, in the study of Afrooz *et al.*,[16] bridging was likely to be the dominant mechanism for the heteroaggregation of poly(acrylic acid)-coated gold nanoparticles and pluronic acid-modified CNTs.

After either homo- or heteroaggregation, disaggregation may take place when the solution chemistry is changed or when the aggregates are exposed to strong hydrodynamic forces that can be present in natural aquatic environments. The techniques that have been employed to investigate the disaggregation of colloidal aggregates mainly involve the perturbation of the aggregate samples either through the introduction of hydrodynamic forces (*e.g.*, in impeller-based stirred tanks,[17] contracting nozzles,[18] and filtration columns[19]) or through the introduction of ultrasonic energy (*e.g.*, using ultrasonication probes or baths[20-22]). In most of these studies, no independent measurements were conducted to ensure that the amount of energy used for disaggregating the aggregates was consistent between experiments, which is essential for the fair comparison of the strength of aggregates between experiments. While some studies have shown that homoaggregates comprising iron oxide nanoparticles and titanium dioxide nanoparticles can undergo disaggregation when the solution composition is changed (*e.g.*, through the addition of natural organic matter),[23, 24] no studies have been conducted on the disaggregation of heteroaggregates composed of CNTs and other types of colloids.

In this study, the disaggregation behavior of heteroaggregates that were composed of multiwalled CNTs and HemNPs was investigated and compared with that of CNT homoaggregates. The experiments involved the use of ultrasound to disaggregate the heteroaggregates and dynamic light scattering (DLS) for the measurements of the size of the aggregates before and after ultrasonication to determine the degree of disaggregation. A calorimetric method was employed to measure the ultrasonic power delivered to the test suspensions. Furthermore, the disaggregation experiments were designed such that no transfer of aggregate samples from one system to another was required and the unintended disaggregation of aggregates was hence circumvented. Through the disaggregation experiments, the strength of the heteroaggregates was evaluated in different solution chemistries and the stability of the nanoparticles and aggregates was evaluated after ultrasonication.

3.2. Materials and Methods

3.2.1. Preparation and characterization of CNTs and HemNPs

The details for the preparation of the nanomaterials employed in this Chapter were presented in Chapter 2.[12] Briefly, as-received multiwalled CNTs (PD15L5-20, NanoLab Inc., Newton, MA) were cleaned and oxidized using a mixture of concentrated H_2SO_4 and HNO_3. HemNPs were synthesized through the forced hydrolysis of a $FeCl_3$ solution.[25-27] The hydrodynamic diameters of the CNTs and HemNPs were determined to be 106.0 nm and 82.6 nm, respectively, through DLS. Through X-ray photoelectron spectroscopy (XPS) analysis,[14, 28] the CNTs were determined to have a total surface oxygen content of 10.3%. The XPS analysis also showed that the predominant oxygen-containing functional groups on the surface of CNTs were the carboxyl groups, which contributed to 70% of the total surface oxygen content.[12, 29] Carbonyl groups and hydroxyl groups were found to make up 15% and 10% of the total surface oxygen content, respectively.[12, 29] The total organic carbon (TOC) content of the CNT stock suspension was determined through combustion catalytic oxidation at 680 °C (Shimadzu TOC-VCSN) to be 1.39 mg/L, while the nanoparticle concentration in the HemNP stock suspension was determined through gravimetric analysis to be 4.4 g/L.,[12] which was estimated to equate to a HemNP number concentration of 2.41×10^{12} particles/mL.

3.2.2. Solution Chemistry

ACS reagent grade NaCl and NaOH were used to prepare the stock solutions. The NaCl stock solution was filtered through a 0.1-μm PVDF membrane (Millipore, MA) before use. A humic acid stock solution (Suwannee River humic acid, Standard II, International Humic Substances Society) with a total organic carbon (TOC) concentration of 231.11 mg/L was prepared using the procedures described in Chapter 2.

3.2.3. Time-Resolved Dynamic Light Scattering

Time-resolved DLS was used to monitor the hydrodynamic diameters of CNT homoaggregates and CNT–HemNP heteroaggregates as a function of time during the disaggregation experiments. Details of the light scattering setup and time-resolved DLS measurement are presented in Chapter 2.

3.2.4. Disaggregation Experiments

Before the disaggregation experiments, the aggregates of interest were firstly prepared by allowing the nanoparticles to undergo aggregation under favorable (non-repulsive or attractive) conditions. Specifically, CNT homoaggregates were formed at pH 5.5 and 500.0 mM NaCl, at which the NaCl concentration was high enough such that the energy barrier to aggregation between the negatively-charged CNTs was eliminated (Chapter 2). Heteroaggregates composed of CNTs and HemNPs were formed at pH 5.5 and 0.1 mM NaCl. At this solution chemistry, heteroaggregation between CNTs and HemNPs was favorable since CNTs and HemNPs were oppositely charged at pH 5.5.[12, 30] Heteroaggregation occurred exclusively under such conditions since strong electrostatic repulsion between nanoparticles of the same type prevented the homoaggregation of either CNTs or HemNPs (Chapter 2).

To induce CNT homoaggregation, a predetermined volume of NaCl stock solution was added into a DLS vial (borosilicate glass, VWR) that contained a CNT suspension prepared in deionized (DI) water (Millipore, MA). CNTs were allowed to undergo homoaggregation at a CNT concentration of 111 μg/L TOC. To induce CNT–HemNP heteroaggregation, a predetermined volume of CNT stock suspension was transferred into a DLS vial holding a diluted suspension of HemNPs. CNTs and HemNPs underwent heteroaggregation at CNT and HemNP concentrations of 56 μg/L TOC and 1.76 mg/L, respectively. These concentrations resulted in a CNT/HemNP concentration ratio of 0.032 (by mass) at which the heteroaggregation rate was observed to be the fastest (Chapter 2). The final CNT homoaggregate or CNT–HemNP heteroaggregate suspensions had a volume of 1 mL. They were vortexed for ca. 1–2 s and immediately inserted into the light scattering system. The increase in the hydrodynamic diameter of CNT homoaggregates and CNT–HemNP heteroaggregates was monitored continuously through time-resolved DLS. In the CNT–HemNP heteroaggregate suspensions employed in this study, the HemNPs were the dominant light scatterers because the light scattering intensity from HemNPs was at least 20 times higher than that from CNTs (Chapter 2). Since the homoaggregation of CNTs or HemNPs did not take place at pH 5.5 and 0.1 mM NaCl, the growth in the size of CNT–HemNP heteroaggregates can be quantified by the increase in the hydrodynamic diameter of spherical HemNPs obtained from DLS measurements performed on the heteroaggregate suspensions.[12]

Disaggregation experiments were conducted using an ultrasonication bath (Branson B1510, 40 kHz). A wire cage was assembled using 14-gauge steel wire (OD 1.98 mm, used for the cage frame) and 22-gauge steel wire (OD 0.73 mm, used to fasten the components of the frame) to hold the test suspensions at a fixed position in the ultrasonication bath. The cage was firmly secured in the ultrasonication bath and it held a 50-mL centrifuge tube (BD Biosciences, NJ) in the center of the bath, in which the vial containing the test suspension was positioned. This ultrasonication setup is presented in Figure 3.1a.

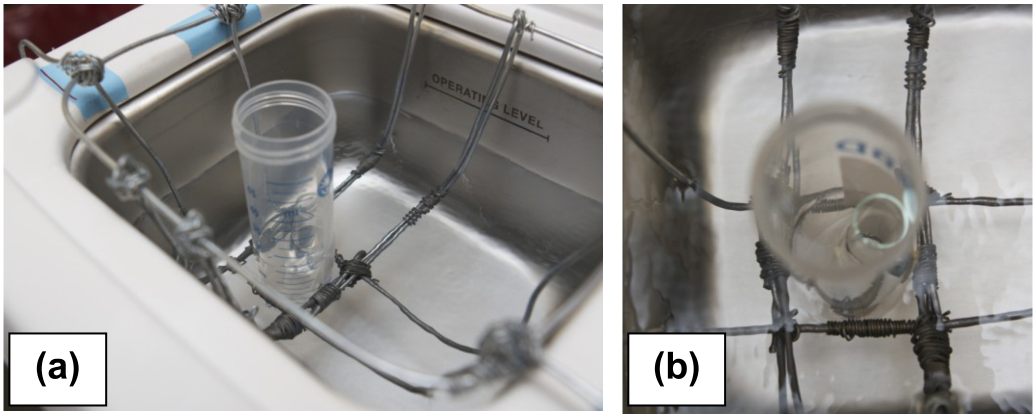

Figure 3.1. (a) Experimental setup for the disaggregation experiments. (b) The DLS vial containing the aggregate sample was held in a 50-mL centrifuge tube secured in the cage during ultrasonication.

Before the start of each disaggregation experiment, the ultrasonication bath was filled with 1 L of distilled water and a new centrifuge tube containing 20 mL of DI water was secured in position in the cage. After the initiation of homoaggregation or heteroaggregation, when the hydrodynamic diameter of the CNT homoaggregates or CNT–HemNP heteroaggregates increased to 400 ± 25 nm, the DLS vial containing the aggregating suspension was removed from the light scattering system. A solution of interest (2 mL) was gently introduced into the DLS vial to obtain the desired solution chemistry for disaggregation (final volume = 3 mL). For the CNT homoaggregates, the disaggregation experiments were performed at pH 5.5 and 500.0 mM NaCl. For the CNT–HemNP heteroaggregates, the disaggregation was performed at three different solution chemistries: (i) pH 5.5 in the absence of humic acid , (ii) pH 11.0 in the absence of humic acid , and (iii) pH 5.5 in the presence of 1 μg/L TOC of humic acid (calculated from the concentration of the stock humic acid solution and the dilution factor). All disaggregation experiments of heteroaggregates were conducted in the presence of 0.1 mM NaCl. The dilution of the aggregating suspensions (from 1 to 3 mL) will reduce the degree of aggregation which may take place concurrently during the ultrasonication process and confound the analysis of the disaggregation results.[20] The DLS vial was then placed inside the centrifuge tube as shown in Figure 3.1b and the ultrasonication process was started. The water levels in the centrifuge tube and the ultrasonication bath were at the same elevation once the DLS vial was inside the centrifuge tube.

The disaggregation experiments were conducted over durations of 30 s, 2 min, 4 min, and 6 min. At the completion of the ultrasonication process, the DLS vial was taken out of the centrifuge tube, quickly dried with a piece of lens paper (Fisher), and then immediately inserted into the light scattering system for DLS measurements. It took *ca.* 30 s to dry and insert the DLS vial into the light scattering system. Since this process did not require the transfer of the aggregate suspensions with the use of a pumping device or a pipette, the change in the hydrodynamic diameter of the aggregates in the suspensions was solely due to the disaggregation of the aggregates during the ultrasonication process. All the experiments were conducted at room temperature and repeated for at least three times.

3.2.5. Determination of Power Delivered by Ultrasonication Bath

A calorimetric method[31] was employed to determine the ultrasonic power that was delivered by the ultrasonication bath, as well as to verify that the ultrasonication bath was delivering the same power for all disaggregation experiments. This method involved the use of a thermocouple thermometer (Dig-Sense DualLogR) to record the water temperature as a function of time during the ultrasonication process. Calorimetric curves were then constructed by plotting the water temperature against time. The delivered ultrasonic power was calculated from Equation 3.1:[31]

$$P = \frac{dT}{dt} M C_p \tag{3.1}$$

where P is the delivered ultrasonic power (W), T is temperature (K), t is time (s), M is the mass of the ultrasonicated water (= 1000 g), and C_p is the specific heat capacity of water (= 4.18 $\mathrm{J g^{-1} K^{-1}}$). The slope of the calorimetric curves, $\mathrm{d}T/\mathrm{d}t$, was determined through linear regression analysis.

The delivered ultrasonic power was determined before the start of the disaggregation experiments. The temperature probe of the thermometer was immersed in the middle of the ultrasonication bath, *ca.* 1 cm above the base of the bath.[31] The total logging time was 30 min and the temperature-logging interval was 10 s.

3.2.6. Determination of Degree of Disaggregation

The degree of disaggregation (DoD) was used to quantify the aggregate breakage resulting from the ultrasonication process. It was calculated using Equation 3.2:

$$DoD(\%) = \frac{D_{before} - D_{after}}{D_{before} - D_0} \times 100\% \tag{3.2}$$

where D_{before} is the hydrodynamic diameter of aggregates immediately before ultrasonication (average of four DLS measurements), D_{after} is the hydrodynamic diameter of aggregates immediately after ultrasonication (average of four DLS measurements), and D_0 is the average hydrodynamic diameter of the CNTs (for disaggregation of CNT homoaggregates) or HemNPs (for disaggregation of CNT–HemNP heteroaggregates) obtained from twenty DLS measurements. A DoD of 100% indicates that the aggregates are completely disaggregated to become dispersed nanoparticles, while a DoD of 0% indicates that no disaggregation has occurred. Consequently, the DoD is a suitable measure to indirectly determine the strength of the aggregates.

3.3. Results and Discussion

3.3.1. Power of Ultrasonication Bath

A constant ultrasonic power delivered by the ultrasonication bath is essential for a fair comparison of the disaggregation behavior between the aggregates and of their aggregate strength. Five representative calorimetric curves are shown in Figure 3.2. It was observed from all the curves that the water temperature increased linearly with increasing duration of ultrasonication. Although the position of the calorimetric curve depended on the initial temperature of the water in the bath, the slopes of the curves were not influenced by the initial temperature. The slopes of all calorimetric curves obtained for our disaggregation experiments (13 in total) were found to be nearly identical. This observation confirmed that ultrasonic power delivered by the ultrasonication bath was the same for all disaggregation experiments. The average slope of the calorimetric curves was determined to be 0.0042 °C/s (standard deviation = 0.0002 °C/s). By using Equation 3.1, the ultrasonic power delivered to the water in the ultrasonication bath (volume of 1 L) was calculated to be 17.7 W. The power delivered to the test suspensions in the DLS vials during ultrasonication (volume of 3 mL) was therefore estimated to be 53.2 mW.

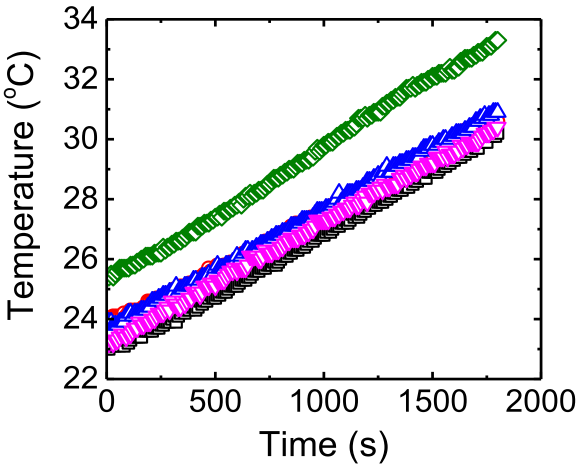

Figure 3.2. Representative calorimetric curves obtained for the ultrasonication bath employed for the disaggregation experiments.

3.3.2. Disaggregation of CNT Homoaggregates at pH 5.5 and 500.0 mM NaCl

The disaggregation of CNT homoaggregates was investigated at pH 5.5 and 500.0 mM NaCl. A representative aggregation and disaggregation profile of the CNTs obtained from DLS measurements is presented in Figure 3.3. This profile comprises three regions: (i) aggregation (0–825 s), (ii) disaggregation (825–1230 s), and (iii) re-growth (>1230 s).

In this particular experiment, the homoaggregate suspension was subjected to 6 min of ultrasonication in the disaggregation region. Representative aggregation and disaggregation profiles for ultrasonication durations of 30 s, 2 min, 4 min, and 6 min are shown in Figure 3.4a. For all four ultrasonication durations, an abrupt drop in CNT homoaggregate size was observed after ultrasonication. An increase in the homoaggregate size (i.e., re-growth) was also observed after the disaggregation region for all durations of disaggregation.

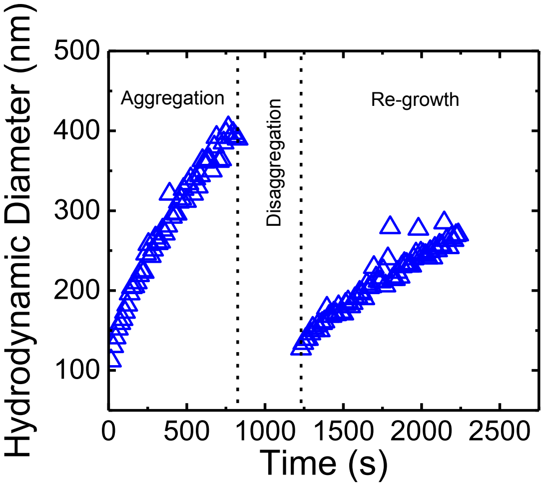

Figure 3.3. Representative time-resolved DLS measurements of the hydrodynamic diameter of CNT homoaggregates before and after 6 min of ultrasonication. Three regions are shown: (i) aggregation, (ii) disaggregation, and (iii) re-growth.

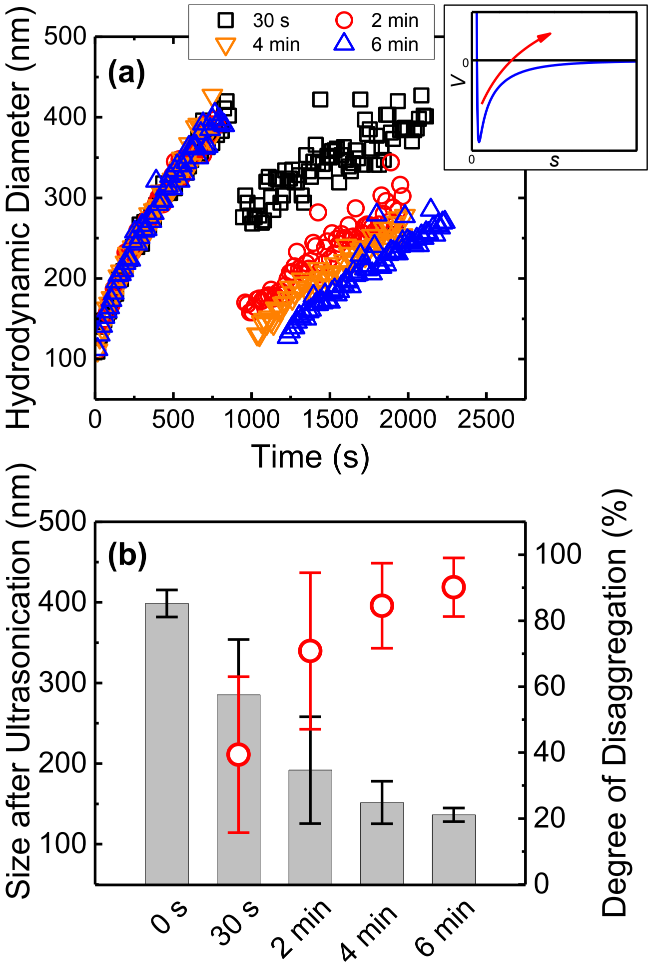

Figure 3.4. (a) Disaggregation of CNT homoaggregates at pH 5.5 and 500.0 mM NaCl for ultrasonication durations of 30 sec, 2 min, 4 min, and 6 min. The profile for 6 min of ultrasonication was reproduced from Figure 3.3. The variation of interaction energy, *V*, between two CNTs as a function of separation distance, *s*, is illustrated in the inset. (b) Size of CNT homoaggregates and the degrees of disaggregation (DoDs) at ultrasonication durations of 30 sec, 2 min, 4 min, and 6 min. Size of homoaggregates before ultrasonication (*i.e.*, 0 s) is also provided. Error bars represent standard deviations.

The influence of ultrasonication duration on the homoaggregate size and DoD is presented in Figure 3.4b. Overall, smaller CNT homoaggregates and higher DoD values were obtained with longer periods of ultrasonication. After 30 s of ultrasonication, the homoaggregate size was reduced from 398.7 nm to 285.3 nm, which corresponded to a

DoD of 38%. When the ultrasonication duration was raised to 2 min, the homoaggregate size was reduced considerably to 191.9 nm, while the DoD increased to nearly 70%. Further increases in the ultrasonication duration to 4 min and 6 min, however, led to less drastic changes in both homoaggregate size and DoD (151.7 nm and 85% for 4 min; 136.4 nm and 90% for 6 min). Since the energy barrier to CNT homoaggregation was eliminated at 500 mM NaCl (Chapter 2),[12] the attachment between CNTs was expected to occur in the primary energy minimum. When the effects of Born repulsion are considered, in additional to DLVO (i.e., electric double layer and van der Waals) interactions, the primary minimum is expected to have a finite depth.[32, 33] Thus, the energy required to break a CNT–CNT bond would be equal to the depth of the primary minimum. A schematic illustrating the finite depth of primary minimum is presented in the inset of Figure 3.4a. Since the CNTs were expected to be chemically heterogeneous,[33, 34] which could be partially contributed by the presence of small amount residual metal catalyst used in the production of CNTs,[35] the CNT–CNT bonds within the CNT homoaggregates were expected to have a distribution of bond strengths. Short durations of ultrasonication (*e.g.*, 30 s and 2 min) would provide sufficient energy to release the CNTs out of the shallow primary minima and break the weaker CNT–CNT bonds. The stronger CNT–CNT bonds, on the other hand, were likely to be either broken only at longer ultrasonication durations (*e.g.*, 4 min and 6 min) or remain unbroken.

The size of CNT homoaggregates seemed to be approaching a stable value of 136.4 nm after 6 min of ultrasonication (Figure 3.4b). Similar observations were made in other studies on the disaggregation of homoaggregates in the presence of hydrodynamic forces.[18, 36, 37] For example, Kobayashi *et al.*[36] reported that the size of homoaggregates composed of latex particles (primary particle size = 1.3 μm) remained the same (*ca.* 4.5 μm) when they were exposed to turbulent flow for more than 90 min. In this current study, since the CNT homoaggregates after 6 min of ultrasonication (= 136.4 nm) was only slightly larger than the primary CNTs (= 106.9 nm), these homoaggregates were likely composed of only a few strands of CNTs.

Aggregation of the CNT homoaggregates was observed in the re-growth region and the slopes of the aggregation profiles in this region were found to be similar (Figure 4.4a). Since the solution chemistry in the re-growth region remained the same as that in the aggregation and disaggregation regions (*i.e.*, pH 5.5 and 500 mM NaCl), no energy barrier to the aggregation between the CNT homoaggregates was expected to exist. Therefore, these CNT homoaggregates were able to undergo favorable aggregation.

3.3.3. Disaggregation of CNT–HemNP Heteroaggregates at pH 5.5 and 0.1 mM NaCl

The aggregation and disaggregation profiles of CNT–HemNP heteroaggregates at pH 5.5 are presented in Figure 3.5a. A sudden decrease in the heteroaggregate size was observed in the disaggregation region for all ultrasonication durations. After the disaggregation region, an increase in the CNT–HemNP heteroaggregate size was observed in the re-growth region for all disaggregation durations. A representative cryogenic transmission electron microscopy (cryo-TEM) image of the CNT–HemNP heteroaggregate is presented in the inset of Figure 3.5a. The CNT and HemNP concentrations used in cryo-TEM imaging were 2.5 times higher than the ones used in the disaggregation experiment to allow for the formation of a reasonable number of heteroaggregates on the TEM grid. The procedures for preparing and imaging the vitrified specimen were described in Chapter 2.

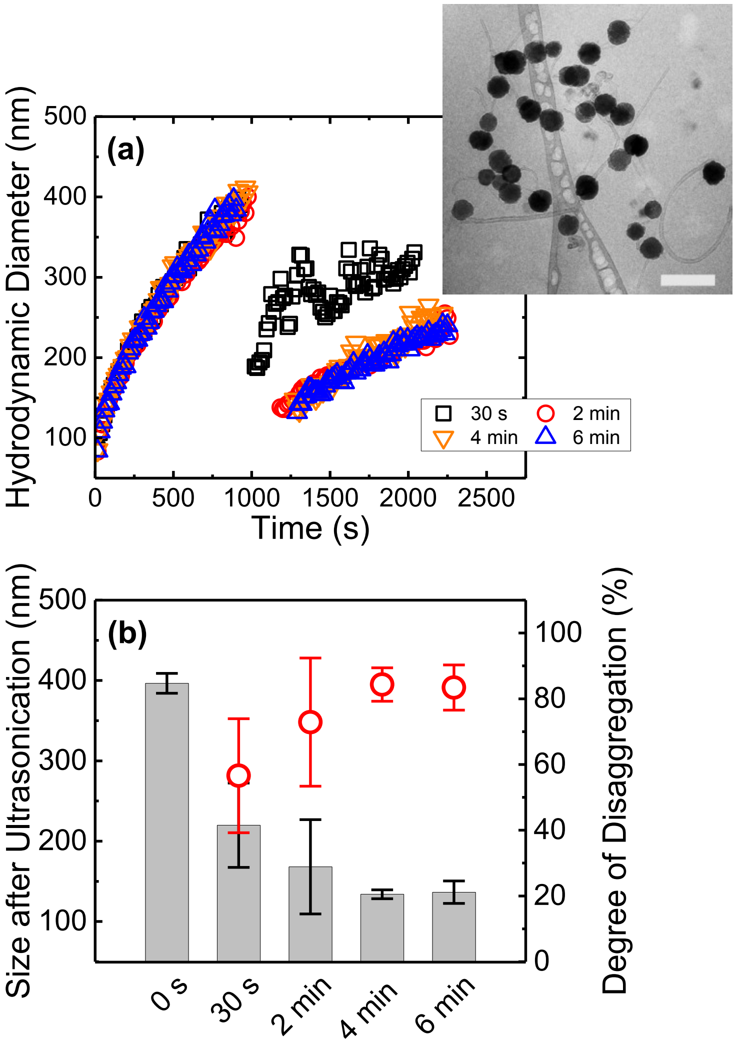

Figure 3.5. (a) Disaggregation of CNT–HemNP heteroaggregates at pH 5.5 and 0.1 mM NaCl for ultrasonication durations of 30 sec, 2 min, 4 min, and 6 min. The inset shows a representative cryo-TEM image of a CNT–HemNP heteroaggregate after *ca.* 15 min of heteroaggregation. The concentrations of both CNTs and HemNPs were 2.5 times higher than the ones used in disaggregation experiments. Scale bar represents 200 nm. (b) Size of CNT–HemNP heteroaggregates and the degrees of disaggregation (DoDs) at ultrasonication durations of 30 sec, 2 min, 4 min, and 6 min. Size of heteroaggregates before ultrasonication (*i.e.*, 0 s) is also provided. Error bars represent standard deviations.

The sizes of the heteroaggregates and the corresponding DoD values obtained at different ultrasonication durations are shown in Figure 3.5b. After only 30 s of ultrasonication, the heteroaggregate size was reduced from 396.4 nm to 219.9 nm, which corresponded to a DoD of 57%. An increase in the ultrasonication duration to 2 min resulted in further decrease in the heteroaggregate size to 168.1 nm, which corresponded to a DoD of 73%. Ultrasonication durations of 4 and 6 min produced nearly identical heteroaggregate sizes (134.0 nm and 136.5 nm, respectively) and DoD values (84% and 83%, respectively), hence indicating that the size of CNT–HemNP heteroaggregates approached a stable value after 4 min of ultrasonication. At 4 min and 6 min of ultrasonication, the heteroaggregates were not completely disaggregated since the heteroaggregate size (134.0 nm) was larger than the size of the primary HemNPs (82.6 nm). The CNT–HemNP heteroaggregates obtained after these ultrasonication durations were expected to compose of several CNT strands and HemNPs. An unpaired and two-sided *t*-test (sample size of 4) showed that the final DoD (at 6 min of ultrasonication) of the CNT–HemNP heteroaggregates was significantly lower than that of CNT homoaggregates with a *P*-value of 0.02, indicating that the CNT–HemNP heteroaggregates were more resistant to disaggregation than the CNT homoaggregates. Indirectly, this result suggests that the CNT–HemNP interactions were stronger than CNT–CNT interactions.

Similar to CNT homoaggregates, an increase in the aggregation size was observed after the disaggregation of the CNT–HemNP heteroaggregates (Figure 3.5a). At pH 5.5 and 0.1 mM NaCl, the CNT components and HemNP components of the CNT–HemNP experienced electrostatic and van der Waals attractions. Therefore, the CNT–HemNP heteroaggregates were able to undergo favorable cluster–cluster aggregation.

3.3.4. Disaggregation of CNT–HemNP Heteroaggregates at Elevated pH

The disaggregation behaviors of CNT–HemNPs heteroaggregates at pH 11.0 are presented in Figure 3.6a. The size of the heteroaggregates was observed to decrease dramatically after ultrasonication. However, in contrast to the observations for both CNT homoaggregates and CNT–HemNP heteroaggregates at pH 5.5, the aggregation profiles after ultrasonication were flat, indicating that no re-growth of aggregates took place. The heteroaggregate sizes and the corresponding DoD values obtained at different periods of ultrasonication are shown in Figure 3.6b. After 30 s of ultrasonication, a DoD of 69% was obtained. The DoD values continued to increase as the ultrasonication duration was increased. After 6 min of ultrasonication, the heteroaggregate size was 86.6 nm, which was similar to the size of primary HemNPs (82.6 nm). This size corresponded to a DoD of 99%, indicating that the heteroaggregates were almost completely disaggregated to primary nanoparticles at the elevated pH.

The strength of an aggregate is dependent on (i) the number of particle-particle bonds within the aggregate structure and (ii) the strength of particle-particle bonds.[17, 38] Since the CNT–HemNP heteroaggregates employed in all disaggregation experiments were prepared at the same CNT and HemNP concentrations and at the same solution chemistry to achieve a comparable hydrodynamic diameter of 400 ± 25 nm, the CNT–HemNP heteroaggregates had similar number of CNT–HemNP bonds and aggregate structure before they were subjected to ultrasonication. Thus, the primary difference in the DoD between pH 5.5 and pH 11.0 was expected due to the difference in the strength of CNT–HemNP interactions within the heteroaggregates.

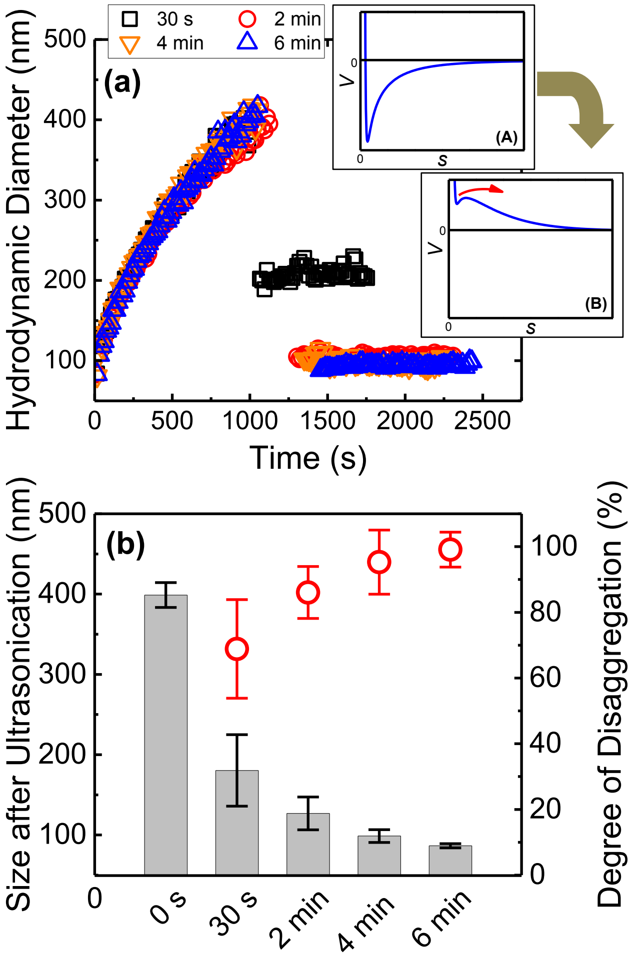

Figure 3.6. (a) Disaggregation of CNT–HemNP heteroaggregates at pH 11.0 and 0.1 mM NaCl for ultrasonication durations of 30 sec, 2 min, 4 min, and 6 min. The change in the variation of interaction energy, *V*, between a CNT and a HemNP as a function of separation distance, *s*, with the increase in pH from 5.5 to 11.0 is illustrated in Insets A (pH 5.5) and B (pH 11.0). (b) Size of CNT–HemNP heteroaggregates and the degrees of disaggregation (DoDs) at ultrasonication durations of 30 sec, 2 min, 4 min, and 6 min. Size of heteroaggregates before ultrasonication (*i.e.*, 0 s) is also provided. Error bars represent standard deviations.

When heteroaggregation between CNTs and HemNPs took place at pH 5.5 and 0.1 mM NaCl, the oppositely charged CNTs and HemNPs underwent favorable attachment in the primary minimum.[32, 33] The energy required to break a CNT–HemNP bond must thus be greater than the depth of the primary minimum (Inset A of Figure 3.6a). With the increase in pH from 5.5 to 11.0 immediately before the ultrasonication process, the surface charge of HemNPs was reversed from positive to negative since hematite has an isoelectric point of pH 9.[30] At the same time, the rise in pH resulted in an increase in deprotonated carboxyl groups on the CNT surface and thus raised the negative charge of the CNT surface.[13] The transition from electrostatic attraction to electrostatic repulsion between the attached CNT and HemNP resulting from the rise in solution pH likely reduced the depth of the primary minimum (Inset B of Figure 3.6a) and weakened the CNT–HemNP interaction within the heteroaggregates, as seen from the complete disaggregation of the heteroaggregates at 6 min. By performing an unpaired and two-sided *t*-test on the average heteroaggregate size obtained after 6 min of ultrasonication (sample size = 4) for pH 5.5 and pH 11.0, the increase in pH from 5.5 to 11.0 was concluded to significantly reduce the size of heteroaggregates after disaggregation (*P*-value = 0.005). As CNTs and HemNPs were both negatively charged at pH 11, electrostatic repulsion prevented re-aggregation of the disaggregated nanoparticles.

3.3.5. Disaggregation of CNT–HemNP Heteroaggregates in the Presence of Humic Acid

The aggregation and disaggregation profiles of CNT–HemNP heteroaggregates at pH 5.5 and 0.1 mM NaCl in the presence of 1 μg/L TOC of humic acid are presented in Figure 3.7a, while the heteroaggregate sizes after ultrasonication and the corresponding DoD values are presented in Figure 3.7b. The DoD was 76% at 30 s of ultrasonication and increased to 88% at 2 min of ultrasonication. At longer ultrasonication durations of 4 and 6 min, the DoD approached a value of 95% and 97%, respectively.

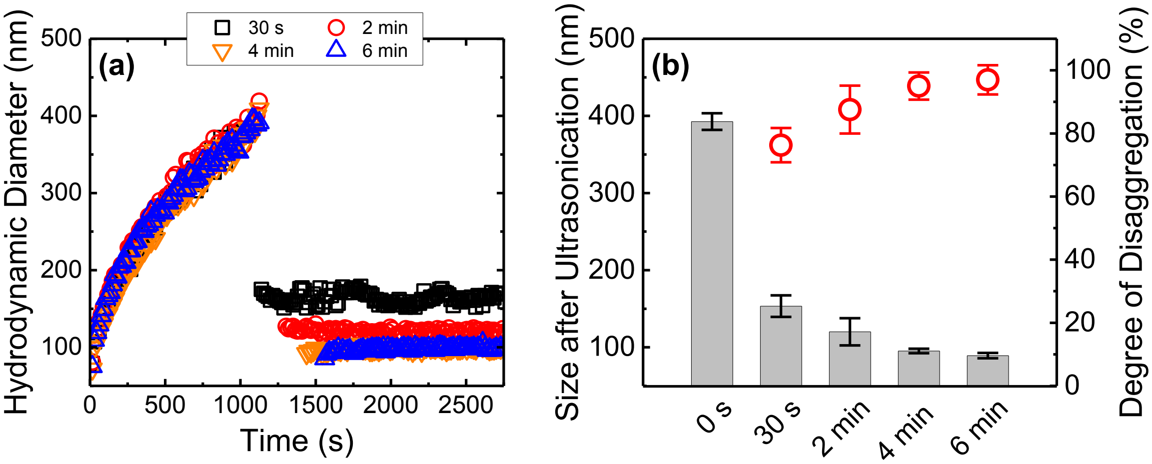

Figure 3.7. (a) Disaggregation of CNT–HemNP heteroaggregates at pH 5.5 and 0.1 mM NaCl in the presence of humic acid (1 μg/L TOC) for ultrasonication durations of 30 sec, 2 min, 4 min, and 6 min. (b) Size of CNT–HemNP heteroaggregates and the degrees of disaggregation (DoDs) at ultrasonication durations of 30 sec, 2 min, 4 min, and 6 min. Size of heteroaggregates before ultrasonication (*i.e.*, 0 s) is also provided. Error bars represent standard deviations.

Electrophoretic mobility measurements conducted in Chapter 2 had shown that an increase in humic acid concentration from 0 to as high as 500 μg/L TOC only slightly raised the surface charge of the CNTs.[12] The presence of humic acid within this range, on the other hand, had a stronger influence on the surface charge of the HemNPs.[12] Specifically, the HemNPs became less positive charged with an initial increase in the humic acid concentration (up to 0.25 μg/L TOC) and they underwent charge reversal at 500 μg/L TOC.[12] Therefore, the electrostatic attraction between CNTs and HemNPs was weakened with the addition of 1 μg/L TOC humic acid. Furthermore, the adsorption of humic acid on the surface of both CNTs and HemNPs will induce electrosteric repulsion between these nanoparticles.[38] The combined effects of the decrease in electrostatic attraction and the presence of electrosteric repulsion may reduce the depth of the primary minimum of CNT–HemNP interaction (insets of Figure 3.6a) which led to a high DoD of 97% after 6 min of sonication. An unpaired and two-sided *t*-test showed that the average size of heteroaggregates after ultrasonication was significantly smaller in the presence of humic acid than that in the absence of humic acid (*P*-value = 0.006, sample size of 4 and 3 in the absence and presence of humic acid, respectively), thus indicating that the introduction of humic acid will reduce the resistance to breakage for the CNT–HemNP heteroaggregates. This result also indirectly demonstrated that the heteroaggregates had lower bond strength in the presence of humic acid. In the presence of humic acid, the aggregation profiles obtained after 2, 4, and 6 min of ultrasonication were flat (Figure 3.7a), indicating that no re-growth in aggregates had occurred. The high stability of the disaggregated nanoparticles and aggregates after ultrasonication could be explained by the decrease in electrostatic attraction and the presence of electrosteric repulsion, both resulted from the adsorption of humic acid on the nanoparticle surface. In contrast, slight fluctuations were present in the aggregation profile after 30 s of ultrasonication, possibly because the energy provided was only enough to partially disaggregate the heteroaggregates to form aggregates that were extremely heterogeneous in size.

3.3.6. Conclusions

The disaggregation behavior and the strength of CNT–HemNP heteroaggregates formed under favorable conditions were investigated using ultrasound and DLS. Calorimetric tests were conducted to ensure that a constant ultrasonic power was employed for all the disaggregation experiments. The elevation of solution pH, as well as the introduction of low concentrations of humic acid, significantly increased the propensity for the heteroaggregates to undergo disaggregation. With the consideration of DLVO interactions together with Born repulsion, it was speculated that these changes in solution chemistry that either led to an increase in electrostatic repulsion or introduced electrosteric repulsion between CNTs and HemNPs weakened the CNT–HemNP interactions within the heteroaggregates.

3.4. References

1. Iijima, S., Helical Microtubules of Graphitic Carbon. *Nature* **1991,** *354*, (6348), 56-58.

2. Ajayan, P. M.; Zhou, O. Z., Applications of carbon nanotubes. *Top Appl Phys* **2001,** *80*, 391-425.

3. Baughman, R. H.; Zakhidov, A. A.; de Heer, W. A., Carbon nanotubes - the route toward applications. *Science* **2002,** *297*, (5582), 787-792.

4. Yu, M. F.; Files, B. S.; Arepalli, S.; Ruoff, R. S., Tensile loading of ropes of single wall carbon nanotubes and their mechanical properties. *Phys Rev Lett* **2000,** *84*, (24), 5552-5555.

5. Endo, M.; Strano, M. S.; Ajayan, P. M., Potential applications of carbon nanotubes. *Top Appl Phys* **2008,** *111*, 13-61.

6. Kohler, A. R.; Som, C.; Helland, A.; Gottschalk, F., Studying the potential release of carbon nanotubes throughout the application life cycle. *J Clean Prod* **2008,** *16*, (8-9), 927-937.

7. Petersen, E. J.; Zhang, L.; Mattison, N. T.; O'Carroll, D. M.; Whelton, A. J.; Uddin, N.; Nguyen, T.; Huang, Q.; Henry, T. B.; Holbrook, R. D.; Chen, K. L., Potential Release Pathways, Environmental Fate, And Ecological Risks of Carbon Nanotubes. *Environ Sci Technol* **2011,** *45*, (23), 9837-9856.

8. Kang, S.; Herzberg, M.; Rodrigues, D. F.; Elimelech, M., Antibacterial effects of carbon nanotubes: Size does matter. *Langmuir* **2008,** *24*, (13), 6409-6413.

9. Johnston, H. J.; Hutchison, G. R.; Christensen, F. M.; Peters, S.; Hankin, S.; Aschberger, K.; Stone, V., A critical review of the biological mechanisms underlying the

in vivo and in vitro toxicity of carbon nanotubes: The contribution of physico-chemical characteristics. *Nanotoxicology* **2010,** *4*, (2), 207-246.

10. Petosa, A. R.; Jaisi, D. P.; Quevedo, I. R.; Elimelech, M.; Tufenkji, N., Aggregation and Deposition of Engineered Nanomaterials in Aquatic Environments: Role of Physicochemical Interactions. *Environ Sci Technol* **2010,** *44*, (17), 6532-6549.

11. Chen, K. L.; Smith, B. A.; Ball, W. P.; Fairbrother, D. H., Assessing the colloidal properties of engineered nanoparticles in water: case studies from fullerene C(60) nanoparticles and carbon nanotubes. *Environ Chem* **2010,** *7*, (1), 10-27.

12. Huynh, K. A.; McCaffery, J. M.; Chen, K. L., Heteroaggregation of Multiwalled Carbon Nanotubes and Hematite Nanoparticles: Rates and Mechanisms. *Environ Sci Technol* **2012,** *46*, (11), 5912-5920.

13. Smith, B.; Wepasnick, K.; Schrote, K. E.; Bertele, A. H.; Ball, W. P.; O'Melia, C.; Fairbrother, D. H., Colloidal Properties of Aqueous Suspensions of Acid-Treated, Multi-Walled Carbon Nanotubes. *Environ Sci Technol* **2009,** *43*, (3), 819-825.

14. Smith, B.; Wepasnick, K.; Schrote, K. E.; Cho, H. H.; Ball, W. P.; Fairbrother, D. H., Influence of Surface Oxides on the Colloidal Stability of Multi-Walled Carbon Nanotubes: A Structure-Property Relationship. *Langmuir* **2009,** *25*, (17), 9767-9776.

15. Saleh, N. B.; Pfefferle, L. D.; Elimelech, M., Aggregation Kinetics of Multiwalled Carbon Nanotubes in Aquatic Systems: Measurements and Environmental Implications. *Environ Sci Technol* **2008,** *42*, (21), 7963-7969.

16. Afrooz, A. R. M. N.; Khan, I. A.; Hussain, S. M.; Saleh, N. B., Mechanistic Heteroaggregation of Gold Nanoparticles in a Wide Range of Solution Chemistry. *Environ Sci Technol* **2013,** *47*, (4), 1853-1860.

17. Jarvis, P.; Jefferson, B.; Gregory, J.; Parsons, S. A., A review of floc strength and breakage. *Water Research* **2005,** *39*, (14), 3121-3137.

18. Soos, M.; Ehrl, L.; Babler, M. U.; Morbidelli, M., Aggregate Breakup in a Contracting Nozzle. *Langmuir* **2010,** *26*, (1), 10-18.

19. Chowdhury, I.; Hong, Y.; Honda, R. J.; Walker, S. L., Mechanisms of TiO2 nanoparticle transport in porous media: Role of solution chemistry, nanoparticle concentration, and flowrate. *Journal of Colloid and Interface Science* **2011,** *360,* (2), 548-555.

20. Higashitani, K.; Yoshida, K.; Tanise, N.; Murata, H., Dispersion of Coagulated Colloids by Ultrasonication. *Colloid Surface A* **1993,** *81*, 167-175.

21. Wen, H. J.; Lee, D. J., Strength of cationic polymer-flocculated clay flocs. *Advances in Environmental Research* **1998,** *2*, (3), 390-396.

22. Quarch, K.; Durand, E.; Schilde, C.; Kwade, A.; Kind, M., Mechanical fragmentation of precipitated silica aggregates. *Chem Eng Res Des* **2010,** *88*, (12A), 1639-1647.

23. Baalousha, M., Aggregation and disaggregation of iron oxide nanoparticles: Influence of particle concentration, pH and natural organic matter. *Science of the Total Environment* **2009,** *407*, (6), 2093-2101.

24. Loosli, F.; Coustumer, P. L.; Stoll, S., TiO2 nanoparticles aggregation and disaggregation in presence of alginate and Suwannee River humic acids. pH and concentration effects on nanoparticle stability. *Water Research 47*, (16), 6052-6063.

25. Matijevic, E.; Scheiner, P., Ferric hydrous oxide sols: III. Preparation of uniform particles by hydrolysis of Fe(III)-chloride, -nitrate, and -perchlorate solutions. *Journal of Colloid and Interface Science* **1978,** *63*, (3), 509-524.

26. Mylon, S. E.; Chen, K. L.; Elimelech, M., Influence of natural organic matter and ionic composition on the kinetics and structure of hematite colloid aggregation: Implications to iron depletion in estuaries. *Langmuir* **2004,** *20*, (21), 9000-9006.

27. Chen, K. L.; Mylon, S. E.; Elimelech, M., Aggregation kinetics of alginate-coated hematite nanoparticles in monovalent and divalent electrolytes. *Environ Sci Technol* **2006,** *40*, (5), 1516-1523.

28. Cho, H. H.; Smith, B. A.; Wnuk, J. D.; Fairbrother, D. H.; Ball, W. P., Influence of surface oxides on the adsorption of naphthalene onto multiwalled carbon nanotubes. *Environ Sci Technol* **2008,** *42*, (8), 2899-2905.

29. Yi, P.; Chen, K. L., Influence of Surface Oxidation on the Aggregation and Deposition Kinetics of Multiwalled Carbon Nanotubes in Monovalent and Divalent Electrolytes. *Langmuir* **2011,** *27*, (7), 3588-3599.

30. Chen, K. L.; Mylon, S. E.; Elimelech, M., Enhanced aggregation of alginate-coated iron oxide (hematite) nanoparticles in the presence of calcium, strontium, and barium cations. *Langmuir* **2007,** *23*, (11), 5920-5928.

31. Taurozzi, J. S.; Hackley, V. A.; Wiesner, M. R., Ultrasonic dispersion of nanoparticles for environmental, health and safety assessment - issues and recommendations. *Nanotoxicology* **2011,** *5*, (4), 711-729.

32. Ruckenstein, E.; Prieve, D. C., Adsorption and Desorption of Particles and Their Chromatographic-Separation. *Aiche J* **1976,** *22*, (2), 276-283.

33. Yi, P.; Chen, K. L., Influence of Solution Chemistry on the Release of Multiwalled Carbon Nanotubes from Silica Surfaces. *Environ Sci Technol* **2013,** *47*, (21), 12211-12218.

34. Yi, P.; Chen, K. L., Interaction of Multiwalled Carbon Nanotubes with Supported Lipid Bilayers and Vesicles as Model Biological Membranes. *Environ Sci Technol* **2013,** *47*, 5711-5719.

35. Wepasnick, K. A.; Smith, B. A.; Schrote, K. E.; Wilson, H. K.; Diegelmann, S. R.; Fairbrother, D. H., Surface and structural characterization of multi-walled carbon nanotubes following different oxidative treatments. *Carbon* **2011,** *49*, (1), 24-36.

36. Kobayashi, M.; Adachi, Y.; Ooi, S., Breakup of fractal flocs in a turbulent flow. *Langmuir* **1999,** *15*, (13), 4351-4356.

37. Harshe, Y. M.; Lattuada, M.; Soos, M., Experimental and Modeling Study of Breakage and Restructuring of Open and Dense Colloidal Aggregates. *Langmuir* **2011,** *27*, (10), 5739-5752.

38. Elimelech, M.; Gregory, J.; Jia, X.; Williams, R. A., *Particle deposition and aggregation: measurement, modelling, and simulation*. Butterworth-Heinemann: Oxford; Boston, 1995; p xv, 441 p.

Chapter 4. Aggregation Kinetics of Citrate and Polyvinylpyrrolidone Coated Silver Nanoparticles in Monovalent and Divalent Electrolyte Solutions*

---

*This chapter has been published as: Huynh, K. A. and Chen, K. L., Aggregation Kinetics of Citrate and Polyvinylpyrrolidone Coated Silver Nanoparticles in Monovalent and Divalent Electrolyte Solutions, *Environmental Science and Technology*, 2011, 45, 5564–5571. Co-author Kai Loon Chen helped with data interpretation and manuscript editing.

4.1. Introduction

Because of the optical and antimicrobial properties and electrical conductivity of silver nanoparticles (AgNPs),[1-4] these nanomaterials are already finding applications in a wide variety of fields, which include biomedical, chemical, and electrical engineering. The combination of their antimicrobial activity and relative low cost is likely the key reason for nanosilver-containing products to presently comprise more than 50% of the inventoried consumer products that contain engineered nanoparticles.[5] For example, AgNPs are being incorporated into clothes, bandages, and food containers as deodorizers and disinfectants.[6] In addition, studies have been conducted to explore the use of AgNPs for drinking water treatment applications.[7]

With AgNPs increasingly being manufactured and utilized in consumer products, AgNPs are likely to be released into surface waters and the subsurface. Recent studies have shown that AgNPs can exert toxic effects on mammalian cells[8, 9] and microorganisms,[4, 10] even though the mechanisms for AgNP toxicity are still not well understood. Thus, the potential release of these engineered nanomaterials into the environment has raised concerns on their impacts on the ecosystem and human health.

Currently, the most commonly used method to synthesize spherical, reasonably monodisperse AgNPs is chemical reduction of silver salts.[3] In addition, AgNPs are often modified with capping agents. Since these capping agents are usually negatively charged species or relatively large, hydrophilic polymers, the adsorption of these agents will impart colloidal stability to AgNPs by either enhancing their surface charge or introducing steric or electrosteric repulsion.[11] This enhancement in colloidal stability is especially critical for applications which require the dispersion of AgNPs in aqueous solutions, such as the high ionic strength solutions typically encountered in biomedical applications.

The environmental impact of AgNPs is greatly dependent on their mobility and aggregation behavior in the natural and engineered environment. Recently, Li *et al.*[12] investigated the influence of solution chemistry on the aggregation kinetics of unmodified AgNPs and obtained the critical coagulation concentrations (CCCs) of these nanoparticles through time-resolved dynamic light scattering (DLS). Since the CCC represents the minimum amount of electrolyte needed to completely destabilize the suspension,[13] it provides a useful metric of colloidal stability for AgNPs and hence can be used in the prediction of the fate and transport of AgNPs in natural and engineered systems. To date, no study has been conducted to derive the CCCs of AgNPs that have been modified with capping agents. Furthermore, the impact of natural organic matter (NOM), which is ubiquitous in aquatic systems, on the colloidal stability of modified AgNPs is still not well understood.

The objective of this study is to quantify and compare the aggregation kinetics and colloidal stability of AgNPs that were synthesized through the reduction of a Tollens' reagent and modified with two commonly used capping agents—citrate and polyvinylpyrrolidone (PVP). Time-resolved DLS measurements were conducted to obtain the aggregation kinetics of both modified AgNPs over a range of monovalent (NaCl) and divalent ($MgCl_2$ and $CaCl_2$) electrolyte concentrations. The Derjaguin–Landau–Verwey–Overbeek (DLVO) theory was used to fit the experimental data in order to derive the Hamaker constant of citrate-coated AgNPs. In addition, the influence of humic acid on the colloidal stability of both citrate- and PVP-coated AgNPs was investigated.

4.2. Materials and Methods

4.2.1. Silver Nanoparticle Synthesis and Characterization

All reagents used for the preparation of the citrate- and PVP-coated AgNPs were purchased from Sigma Aldrich. Unmodified AgNPs were synthesized through the reduction of a Tollens' reagent using glucose.[2, 14, 15] Stock solutions of 0.1 M $AgNO_3$ and 1.0 M glucose were prepared and filtered using 0.1-μm alumina syringe filters (Anotop 25, Whatman, Middlesex, UK). A Tollens' reagent comprising 0.1 mM $AgNO_3$ and 0.8 mM NH_4OH was prepared and the pH was adjusted to 11.5 by adding NaOH. The reagent (20 mL) was contained in a 50-mL polypropylene centrifuge tube (BD Biosciences, NJ), which was placed into a glass chamber filled with water. The chamber was connected to a refrigerated isotherm bath circulator (Fisher) in order to maintain the water temperature at 25°C. The glass chamber was subsequently put into an ultrasonic bath (Branson 5510, power 180 W, frequency 40 kHz) to homogenize the reactants in the centrifuge tube and enhance their reactivity.[14] The formation of AgNPs was initiated by introducing 40 μL of glucose stock solution into the Tollens' reagent while the reagent was ultrasonicated. After 45 min of ultrasonication, the color of the mixture changed from colorless to bright yellow, indicating that the formation of AgNPs had occurred. This suspension will be referred to as the *original AgNP stock suspension*. Measurements using inductively coupled plasma mass spectrometry instrument (ICP-MS) showed that the total and dissolved silver concentrations of a freshly prepared stock suspension were 10.360 mg/L and 0.002 mg/L, respectively. These measurements indicated that the yield of AgNP formation was nearly 100%.

In order to prepare the citrate-coated AgNPs, the original AgNP stock suspension was centrifuged at 3,650 *g* (Beckman Coulter, CA, 4,000 rpm) and 15°C for 60 min. 90% volume of the supernatant was decanted and replaced with an equal amount of 1 μM trisodium citrate solution. This cleaning process was repeated two more times. The final suspension was ultrasonicated for 30 min to break up AgNP aggregates that might have formed during the centrifugation process. The suspension was then contained in a tightly capped Pyrex glass bottle and stored in the dark at 4°C. This suspension will be referred to as the *citrate-coated AgNP stock suspension*. The dissolved silver concentration and mass concentration of AgNPs in the citrate-coated AgNP stock suspension used for the aggregation experiments were 0.11 mg/L and 8.47 mg/L, respectively.

In order to prepare the PVP-coated AgNPs, a PVP stock solution was first prepared by adding 24.4 mg of PVP (MW 10 kDa, Sigma-Aldrich) into 50 mL of DI water and stirring the mixture overnight in the dark at room temperature. The total organic carbon (TOC) content of the PVP stock solution was determined to be 297.4 mg/L via UV-persulfate oxidation (Phoenix 8000 TOC analyzer, Dohrmann, OH). The original AgNP stock suspension was centrifuged at 3,650 *g* (Beckman Coulter, CA, 4,000 rpm) at 15°C for 60 min. 90% volume of the supernatant was decanted and replaced with an equal amount of DI water. This cleaning process was repeated two more times. After the supernatant was decanted in the third cleaning process, the remaining highly concentrated AgNP suspension was re-suspended in a diluted PVP solution such that the final PVP concentration in the suspension is 6.6 mg/L TOC. The suspensions were then ultrasonicated for 30 min and stored in the dark at 4°C. The dissolved silver concentration and mass concentration of AgNPs in the PVP-coated AgNP stock suspension used for the aggregation experiments were 0.22 mg/L and 8.25 mg/L, respectively.

The absorbance spectra of citrate- and PVP-coated AgNP suspensions were obtained over a range of wavelengths from 300 to 900 nm by using a UV-Vis spectrophotometer (UV-1800, Shimadzu). In addition, the citrate- and PVP-coated AgNPs were examined using a transmission electron microscope (TEM) (Philips CM300 FEG). A drop of AgNP stock suspension was deposited and dried on a specimen copper TEM grid, which was coated with a Lacey carbon film (SPI Supplies, PA), before being observed under the TEM at 300 kV. The elemental composition and crystalline structure of the AgNPs were obtained through energy dispersive X-ray spectroscopy (EDS) and selected area electron diffraction (SAED) analysis, respectively, with the employment of the TEM. The electron diffraction pattern of PVP-coated AgNPs was obtained by using a Philips EM 420 TEM at 120 kV.

4.2.2. Determination of Silver Nanoparticle and Dissolved Silver Concentrations

The total silver concentrations (including both AgNPs and dissolved silver) of the AgNP suspensions were determined by digesting the suspensions with 70% HNO_3 in a microwave (Mars 5, CEM, NC) at 175°C and for 4.5 min.[16] The digested solutions were then diluted with DI water in order to reduce the HNO_3 concentration to *ca.* 3.5% before the silver concentrations of the diluted samples were measured by inductively coupled plasma mass spectrometry instrument (ICP-MS) (PerkinElmer Elan DRCII). In order to determine the dissolved silver concentration of a suspension, AgNPs were first removed by filtering the suspension using a 3-kDA centrifugal membrane filter (Nanosep, Pall Corp., NY) at 12,000 *g* (Eppendorf, NY, 13,375 rpm) for 20 min. The filtrate was subsequently diluted with 3.5% HNO_3 and analyzed with ICP-MS. The concentration of silver nanoparticles in the suspension can then be calculated through mass balance.

4.2.3. Solution Chemistry

ACS-grade electrolyte (NaCl, $CaCl_2$, and $MgCl_2$) stock solutions were prepared and filtered using 0.1-μm alumina syringe filters (Anotop 25, Whatman) before use. Humic acid stock solution was prepared by dissolving Suwannee River humic acid (Standard II, International Humic Substances Society) in DI water. Details for the preparation of humic acid stock solution is presented in Chapter 2. The TOC of the humic stock solution was determined to be 174.9 mg/L through UV-persulfate oxidation (Phoenix 8000 TOC analyzer, Dohrmann, OH). The chemical properties of the humic acid can be found elsewhere.[17] All experiments and measurements were performed at pH 7.0 ± 0.1 (buffered with 0.15 mM $NaHCO_3$).

4.2.4. Electrophoretic Mobility Measurements

A ZetaPALS analyzer (Brookhaven, NY) was used to measure the electrophoretic mobilities (EPMs) of citrate- and PVP-coated AgNPs over a range of electrolyte concentrations at 25˚C. For each solution chemistry, 5–10 measurements were conducted for each of at least 3 samples. The zeta (ζ) potentials were converted from the average EPMs by using the tabulated values that were provided by Ottewill and Shaw.[18]

4.2.5. Time-Resolved Dynamic Light Scattering.

Details of the light scattering setup and time-resolved DLS measurements can be found in Chapter 2. For the aggregation experiments in the absence of humic acid, a predetermined volume of electrolyte stock solution was added into a vial containing a diluted AgNP suspension in order to induce nanoparticle aggregation. All vials used for DLS measurements were cleaned according to the method described in Chapter 2.[19, 20] The suspension was briefly mixed for less than 3 s by using a vortex mixer (Vortex Genie 2, Fisher Scientific) operated at its maximum setting. The vial was then quickly inserted into the vat of the light scattering unit and the DLS measurements were started immediately. For the aggregation experiments in the presence of humic acid, a premeasured volume of humic acid stock solution was introduced into a vial which contained a dilute suspension of citrate-coated AgNPs or PVP-coated AgNPs. The mixture was vortexed briefly before an appropriate volume of electrolyte stock solution was added into the mixture to induce aggregation. For all aggregation experiments, the AgNP suspensions used for DLS measurements had a total volume of 1 mL and a AgNP concentration of 1.13 mg/L for citrate-coated AgNPs or 1.01 mg/L for PVP-coated AgNPs (7.5 times dilution from citrate- or PVP-coated AgNP stock suspensions, respectively). The total citrate and PVP concentrations of the final citrate- and PVP-coated AgNP suspensions were 0.13 μM and 0.88 mg/L TOC, respectively.

All DLS measurements were conducted at a scattering angle of 90°. Each autocorrelation function was accumulated over 15 s and the intensity-weighted hydrodynamic diameter was then derived using second-order cumulant analysis (Brookhaven software). Time-resolved DLS measurements were performed over time periods of between 12 min and 3 h in order to achieve a large enough increase in hydrodynamic diameter for accurate derivation of aggregation kinetics.

4.2.6. Determination of Aggregation Kinetics

The early-stage aggregation kinetics of AgNPs can be obtained from the initial rate of change of hydrodynamic diameter, D_h, with time, t, as measured by time-resolved DLS. In the early aggregation stage, the initial aggregation rate constant, k, is proportional to the initial rate of increase in D_h and inversely proportional to the initial primary AgNP concentration in the suspension, N_0:[19, 21]

$$k \propto \frac{1}{N_0}\left(\frac{dD_h(t)}{dt}\right)_{t\to 0} \tag{4.1}$$

A linear least squares regression analysis of the initial increase in D_h was conducted to obtain $(\mathrm{d}D_h(t)/\mathrm{d}t)_{t\to 0}$. For most solution chemistries, this analysis was performed over the time period in which the hydrodynamic diameter increased to 1.3 times of the initial hydrodynamic diameter, $D_{h,0}$. At low electrolyte concentrations, however, the hydrodynamic diameter failed to reach $1.3D_{h,0}$. Under such conditions, the linear regression was performed over a prolonged time period (> 90 min). For all solution chemistries, the y-intercept of the fitted line did not exceed 2 nm in excess of $D_{h,0}$.

The attachment efficiency, α, is used to quantify the aggregation kinetics of AgNPs. It is calculated by normalizing the aggregation rate constant obtained in the solution of interest to the rate constant obtained under favorable (non-repulsive) aggregation conditions, k_{fast} [19-21]:

$$\alpha = \frac{k}{k_{fast}} = \frac{\frac{1}{N_0}\left(\frac{dD_h(t)}{dt}\right)_{t\to 0}}{\frac{1}{(N_0)_{fast}}\left(\frac{dD_h(t)}{dt}\right)_{t\to 0,\, fast}} \tag{4.2}$$

The terms with subscript “fast” refer to favorable conditions. To calculate α in the presence of humic acid, $\left(\frac{dD_h(t)}{dt}\right)_{t\to 0, fast}$ was obtained for the same type of AgNPs in the *absence* of humic acid in the same electrolyte of interest. In such cases, α values exceeding unity indicates that interparticle bridging may be taking place.[22]

4.2.7. Detection of AgNP Dissolution

The degree of nanoparticle dissolution taking place in our systems was determined since dissolution may influence the mechanism of AgNP aggregation. Specifically, the precipitation of AgCl resulting from the increase in Ag^+ concentration due to the dissolution of AgNPs may lead to interparticle bridging between AgNPs, which will in turn enhance the nanoparticle aggregation kinetics.[12] The citrate- and PVP-coated AgNP dissolution experiments were conducted in diffusion-limited regime of the AgNPs at the highest electrolyte concentrations used for the aggregation experiments (455 mM NaCl, 27 mM $CaCl_2$, and 27 mM $MgCl_2$). The citrate- and PVP-coated AgNP concentrations used for the dissolution experiments were 1.07 mg/L and 0.91 mg/L, respectively, (similar to the concentrations used for aggregation experiments) and the total volume for each AgNP suspension was either 550 or 1100 μL. The dissolved silver concentrations were determined 30 min after the addition of electrolyte stock solutions by filtering the samples with the 3-kDa centrifugal membranes and then measuring the filtrate with ICP-MS, as described earlier in the Materials and Methods. Since each aggregation experiment in the diffusion-limited regime took only *ca.* 12 min, the dissolved silver concentrations at the end of the aggregation experiments were expected to be smaller than the dissolved silver concentrations measured in the dissolution experiments. Control experiments were performed by introducing DI water of the same volume as the electrolyte stock solutions, which were added into the other samples, into diluted AgNP suspensions and leaving the suspensions aside for 30 min. The dissolution experiments were performed 4–10 times for each solution chemistry.

4.3. Results and Discussion

4.3.1. Physicochemical Properties of Citrate- and PVP-Coated AgNPs

The size distribution of the citrate-coated AgNPs (Figure 4.1a) was determined by using the Digital Micrograph software (Gatan, CA) to measure the diameters of 210 nanoparticles randomly selected from a TEM grid. A representative TEM image of the AgNPs is presented in the insert. The nanoparticles were observed to be spherical with slight angular features. The number average diameter of the citrate-coated AgNPs was 71.3 nm and the standard deviation was 18.9 nm. Through 20 DLS measurements, the average intensity-weighted hydrodynamic diameter of stable citrate-coated AgNPs prepared in DI water was determined to be 72.5 nm, which is very similar to the number average diameter of the nanoparticles. The average intensity-weighted hydrodynamic diameter of PVP-coated AgNPs obtained from 20 DLS measurements was 66.9 nm.

Absorbance peaks of citrate- and PVP-coated AgNP suspensions were at 431 nm and 418 nm, respectively, as shown in Figure 4.2. These values are within the reported range for AgNPs with the size of 57–87 nm.[12, 15] High-resolution TEM imaging of both AgNPs revealed lattice fringes with different alignments within a single nanoparticle, which are indicative of the polycrystalline nature of AgNPs synthesized through the Tollens' method (Figure 4.3).

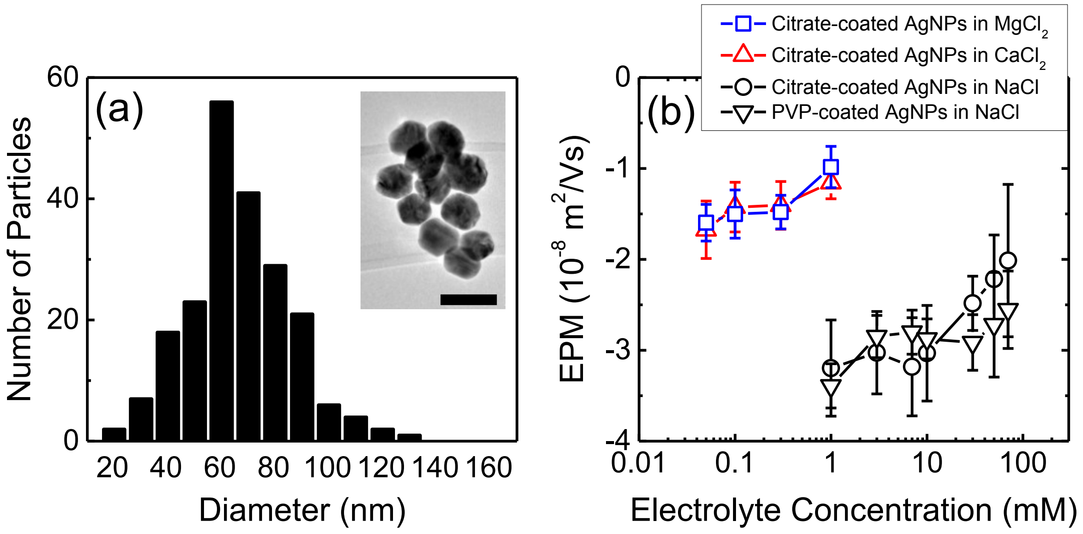

Figure 4.1. (a) Size distribution of 210 citrate-coated AgNPs. The inset presents a representative TEM image of the citrate-coated AgNPs. The scale bar represents 100 nm. (b) Electrophoretic mobilities (EPMs) of citrate- and PVP-coated AgNPs as a function of electrolyte concentration at pH 7.0 and 25˚C. For all measurements, the citrate and PVP concentrations in the suspension were 0.13 μM and 0.88 mg/L TOC, respectively. Each data point represents the mean EPM. Error bars represent standard deviations.

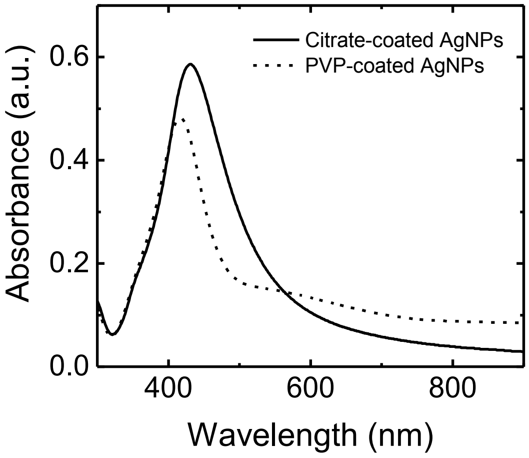

Figure 4.2. Absorbance spectra of citrate- and PVP-coated AgNP stock suspensions. The spectra are expressed in absorbance units (a.u.). The maximum absorption peaks are at 431 nm and 418 nm for citrate- and PVP-coated AgNPs, respectively.

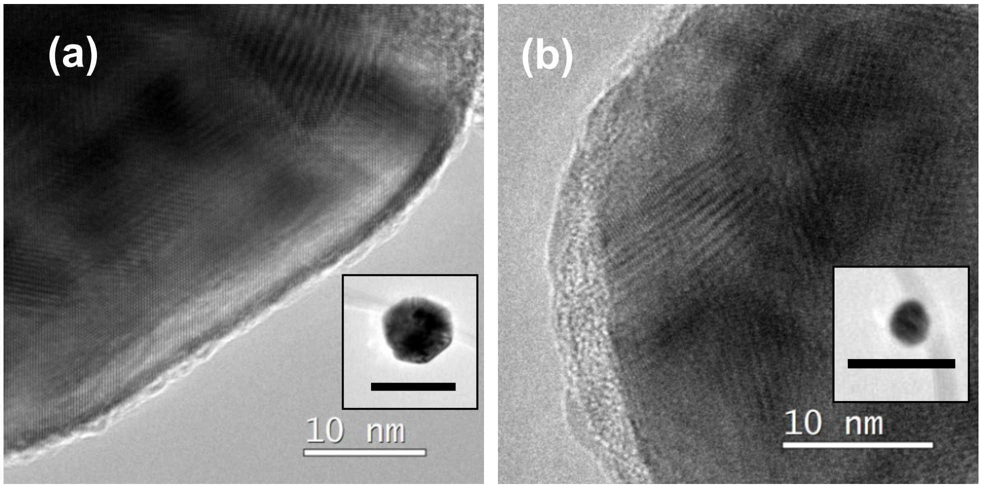

Figure 4.3. High-resolution TEM image of (a) citrate-coated AgNP and (b) PVP-coated AgNP. The insert presents the TEM image of the entire nanoparticle and the scale bar in the insert represents 100 nm.

SAED analysis was performed on citrate- and PVP-coated AgNP clusters and the distances between atomic planes (d-spacing) were determined by measuring the diameters of the first four rings on the diffraction images (Figure 4.4a and Figure 4.5a). The similarity in the first four d-spacing values between the AgNPs (2.38 Å, 2.05 Å, 1.42 Å, 1.23 Å for citrate-coated AgNPs and 2.40 Å, 2.08 Å, 1.50 Å, 1.23 Å for PVP-coated AgNPs) and silver metal[23] (2.36 Å, 2.04 Å, 1.44 Å, 1.23 Å) confirmed that the nanoparticles have the same crystalline structure as bulk silver.

The elements and the qualitative estimate of their abundance in citrate- and PVP-coated AgNPs were obtained by performing TEM-EDS on AgNP samples which were freshly dried on TEM grids. The EDS spectra of randomly selected citrate- and PVP-coated AgNP clusters (Figure 4.4b and Figure 4.5b) indicated that the nanoparticles were mostly composed of silver and the amount of oxygen in the whole cluster was relatively small. Therefore, the results from both SAED and EDS analyses showed that our synthesis method resulted in the production of predominantly zerovalent AgNPs.

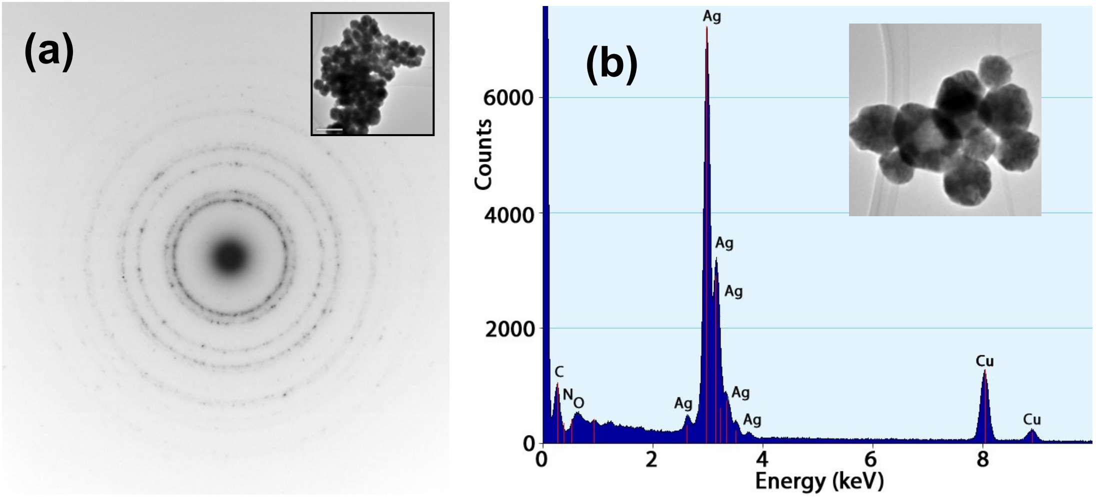

Figure 4.4. (a) TEM-SAED pattern of citrate-coated AgNPs. Insert presents the TEM image of the AgNP cluster used for the SAED analysis. (b) TEM-EDS spectrum of citrate-coated AgNPs. Insert presents the TEM image of the AgNP cluster used for the EDS analysis.

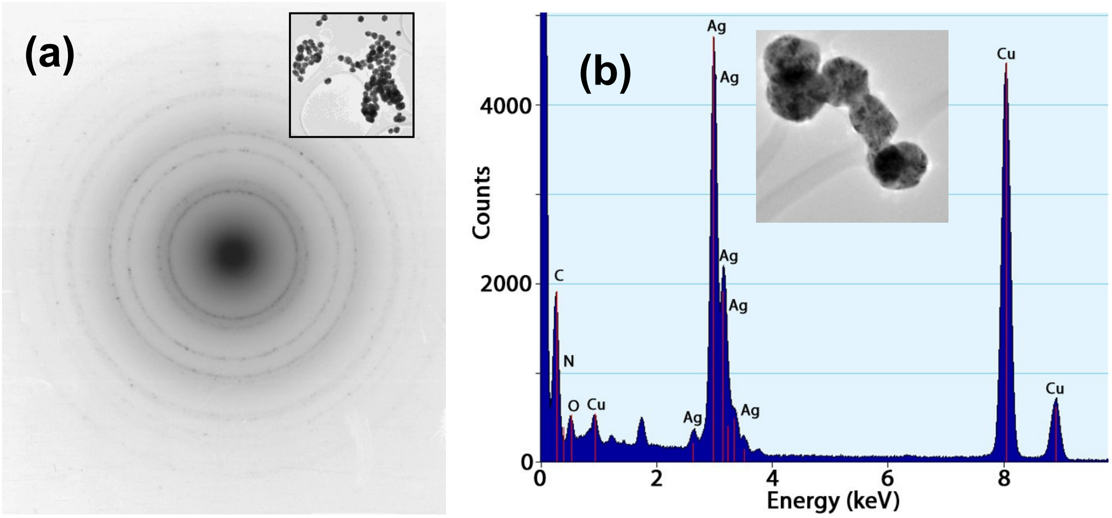

Figure 4.5. (a) TEM-SAED pattern of PVP-coated AgNPs. Insert presents the TEM image of the AgNP cluster used for the SAED analysis. (b) TEM-EDS spectrum of PVP-coated AgNPs. Insert presents the TEM image of the AgNP cluster used for the EDS analysis.

4.3.2. Electrokinetic Properties of Citrate- and PVP-Coated AgNPs

Figure 4.1b presents the EPMs of citrate-coated AgNPs measured over a range of monovalent (NaCl) and divalent ($CaCl_2$ and $MgCl_2$) electrolyte concentrations. The measurements showed that citrate-coated AgNPs were negatively charged over the entire range of monovalent and divalent electrolyte concentrations used in this study. Since the pK_a values of citric acid are 3.13, 4.72, and 6.33,[24] the carboxylic acid groups of citrate molecules are mostly deprotonated at pH 7 and will thus contribute to the surface charge of citrate-coated AgNPs. In addition, the residual side products from AgNP synthesis could also contribute to the negative surface charge of these nanoparticles. With increasing electrolyte concentrations, the EPMs of citrate-coated AgNPs became less negative due to an increase in charge screening (for NaCl) or charge neutralization (for $CaCl_2$ and $MgCl_2$) effects.

Figure 4.1b also presents the EPMs of PVP-coated AgNPs over a range of NaCl concentrations. It was observed that PVP-coated AgNPs had similar EPMs as citrate-coated AgNPs. Since PVP polymers are neutral and the total PVP concentration in the suspension was relatively low (0.88 mg/L TOC), the AgNPs may not be completely coated with PVP and the negative surface charge is likely due to the residual side products which were adsorbed on the nanoparticle surface.

4.3.3. Dissolution of Citrate- and PVP-Coated AgNPs at High Electrolyte Concentrations

Because the precipitation of silver salts may enhance the aggregation kinetics of AgNPs, we performed dissolution experiments at the highest electrolyte concentrations that were used in our aggregation experiments to establish the dissolved silver concentrations under these solution chemistries. These dissolution experiments were performed at 455 mM NaCl, 27 mM $CaCl_2$, and 27 mM $MgCl_2$ for citrate-coated AgNPs and at 455 mM NaCl and 27 mM $CaCl_2$ for PVP-coated AgNPs. These are the electrolyte concentrations at which the nanoparticles underwent diffusion-limited aggregation (to be discussed in the following section). Control experiments were performed in the absence of electrolytes. For these experiments, the samples were prepared in the same manner as for the DLS experiments by diluting the citrate- or PVP-coated AgNP stock suspension 7.5 times before the addition of either the electrolyte solution of interest or DI water (for control experiments).

The dissolved silver concentrations of the citrate- and PVP-coated AgNP suspensions prepared in DI water and electrolyte solutions are presented in Figure 4.6. It should be noted that the initial AgNP and dissolved silver concentrations of citrate- and PVP-coated AgNP suspensions were different because the citrate- and PVP-coated AgNP stock suspensions were prepared separately. The slight increase in dissolved silver concentrations of the citrate- and PVP-coated AgNP suspensions prepared in DI water after 30 min indicated that some dissolution may have occurred. The increase in temperature (from 4 to 25°C) and dissolved oxygen concentration, as well as the decrease in citrate and PVP concentrations, are expected to lead to the slight dissolution of both AgNPs when diluted in DI water.[25-27]

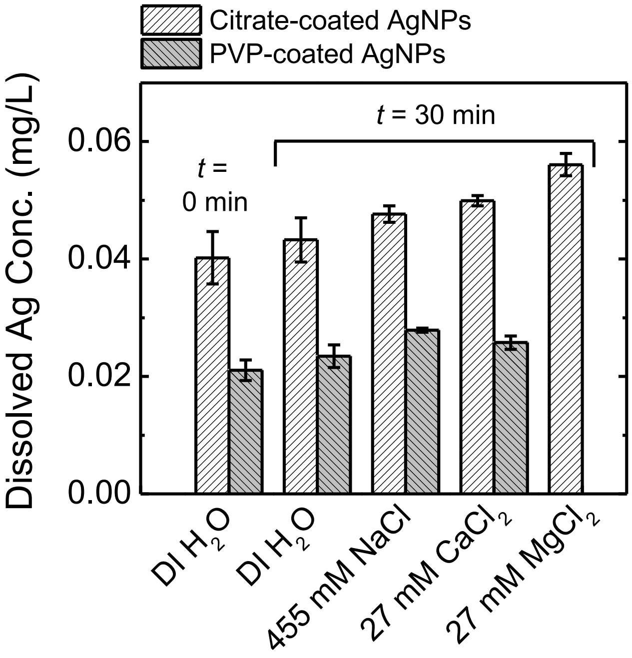

Figure 4.6. Dissolved silver concentrations at either 0 or 30 min after the preparation of citrate- and PVP-coated AgNP suspensions in different solution chemistries at pH 7.0. The initial AgNP concentrations of the citrate- and PVP-coated AgNP suspensions (at *t* = 0 min) were 1.07 mg/L and 0.91 mg/L, respectively. Each bar represents the mean measurement of at least 4 samples. Error bars represent standard deviations.

Also shown in Figure 4.6, citrate- and PVP-coated AgNPs were generally observed to undergo a higher degree of dissolution in all electrolyte solutions than in DI water. These results are consistent to other observations that an increase in ionic strength can enhance AgNP dissolution.[12] The presence of chloride ions in the electrolyte solutions will lead to the formation of soluble silver chloride complexes, such as $AgCl_2^-$ and $AgCl_3^{2-}$,[26] which can accelerate the dissolution of AgNPs. The measured dissolved silver concentrations in solutions of 455 mM NaCl, 27 mM $CaCl_2$, and 27 mM $MgCl_2$ were used as input parameters for the conservative estimation of the concentrations of dissolved silver species in our aggregation experiments at the same solution chemistries

(Visual MINTEQ, Version 3.0). Due to the considerably low dissolved silver concentrations, the simulations confirmed that no precipitation of any silver species (including AgCl) would occur at equilibrium. This result indicates that the minor dissolution of either citrate- or PVP-coated AgNPs in aggregate systems did not lead to precipitation-induced interparticle bridging of AgNPs over the range of NaCl, $CaCl_2$, and $MgCl_2$ concentrations employed in this study.

4.3.4. Aggregation Kinetics of Citrate-Coated AgNPs in Monovalent Electrolyte Solution

Representative aggregation profiles are presented in Figure 4.7. The attachment efficiencies of citrate-coated AgNPs are presented as a function of NaCl concentration in Figure 4.8a. The aggregation behavior of citrate-coated AgNPs in NaCl solutions is consistent with the DLVO theory. At low concentrations of NaCl, the increase in NaCl concentration will elevate the degree of charge screening and hence allow for an increase in aggregation kinetics, as reflected by the rise in attachment efficiency. This regime is known as the reaction-limited regime ($\alpha < 1$). At high NaCl concentrations, the charge of citrate-coated AgNPs is completely screened and the energy barrier between AgNPs is eliminated. Under such conditions, the nanoparticles undergo diffusion-limited aggregation ($\alpha = 1$). In the diffusion-limited regime, the kinetics of aggregation have reached a maximum and are independent of the NaCl concentration. The CCC, which delineates the reaction- and diffusion-limited regimes, was derived by determining the intersection of the extrapolations through both regimes.[19] In NaCl solutions, the CCC of citrate-coated AgNPs was 47.6 mM.

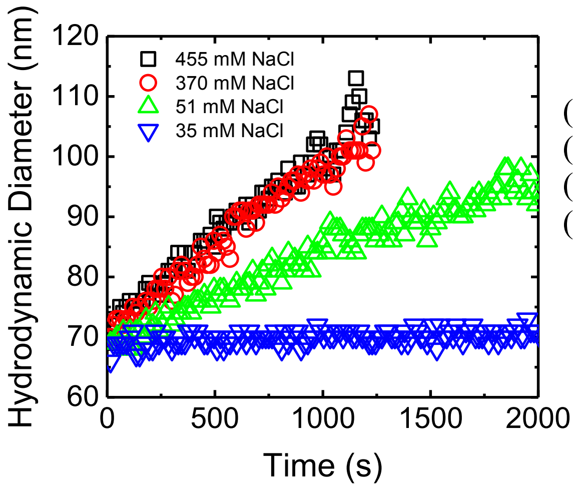

$(dD_h(t)/dt)_{455\ mM} = 0.0290$ nm/s
$(dD_h(t)/dt)_{370\ mM} = 0.0295$ nm/s
$(dD_h(t)/dt)_{51\ mM} = 0.0140$ nm/s
$(dD_h(t)/dt)_{35\ mM} = 0.0012$ nm/s

Figure 4.7. Representative aggregation profiles of citrate-coated AgNPs at four different NaCl concentrations.

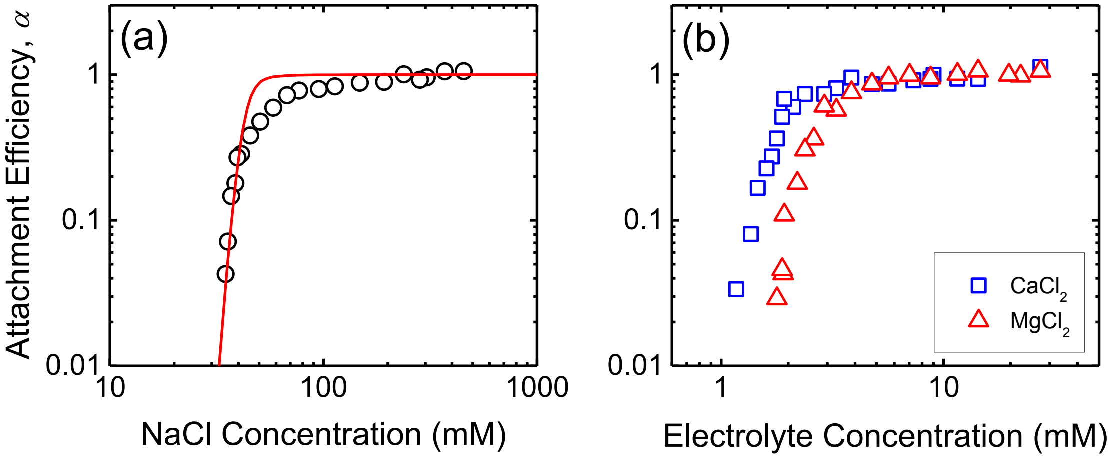

Figure 4.8. Attachment efficiencies of citrate-coated AgNPs as functions of (a) NaCl and (b) $CaCl_2$ and $MgCl_2$ concentrations at pH 7.0. The solid line in a represents DLVO simulation using a Hamaker constant of 3.7 × 10^{-20} J. For all experiments, the citrate concentration in the suspension was 0.13 μM.

Recently, Li *et al.*[12] employed time-resolved DLS to investigate the aggregation kinetics of unmodified AgNPs that were synthesized through the reduction of a Tollens' reagent using D-maltose. In their study, significant AgNP dissolution appeared to have taken place concurrently with nanoparticle aggregation. Li and coworkers detected an immediate and drastic decrease in hydrodynamic diameter (up to 50% decrease) when electrolyte stock solutions (NaCl, $NaNO_3$, or $CaCl_2$) were introduced into the AgNP suspensions. Through TEM imaging, they also observed interconnected AgNPs within AgNP aggregates which were formed in the presence of NaCl, which they attributed to interparticle bridging by AgCl precipitates.[12] In contrast, the degree of dissolution of the citrate- and PVP-coated AgNPs used in this study was too low to result in AgCl precipitation. The considerably higher degree of nanoparticle dissolution in Li *et al.*'s study[12] is possibly due to the absence of capping agent in their systems. In addition, citrate can serve as a reducing agent which will inhibit oxidative dissolution of the citrate-coated AgNPs in our study. Hence, a comparison of the aggregation behavior of AgNPs in both studies demonstrates that both the methods for nanoparticle preparation and the presence of capping agents have significant impacts on the colloidal stability and mechanisms of aggregation of AgNPs.

4.3.5. Comparing Citrate-Coated AgNP Aggregation Kinetics with DLVO Theory

The aggregation kinetics of citrate-coated AgNPs obtained through time-resolved DLS were compared with DLVO theory. The attachment efficiency of aggregating spherical colloidal particles can be calculated by using the following expression which accounts for colloidal and hydrodynamic interactions.[19, 28]

$$\alpha = \frac{\int_0^\infty \beta(h) \frac{\exp\left[V_A(h)/(kT)\right]}{(2a+h)^2} dh}{\int_0^\infty \beta(h) \frac{\exp\left[V_T(h)/(kT)\right]}{(2a+h)^2}} \tag{4.3}$$

where h is the separation distance between two particles, a is the particle radius (35.65 nm, based on the number average diameter of the citrate-coated AgNPs), k is the Boltzmann constant, and T is the absolute temperature (298.15 K). The total interaction energy between two particles, $V_T(h)$, is the sum of the van der Waals attraction, $V_A(h)$, and electrical double layer interaction, $V_R(h)$.

The van der Waals attraction, $V_A(h)$, was calculated using the expression proposed by Gregory [29] that accounts for the electromagnetic retardation effect.

$$V_A(h) = -\frac{Aa}{12h}\left[1 - \frac{bh}{\lambda}\ln\left(1 + \frac{\lambda}{bh}\right)\right] \tag{4.4}$$

where A is the Hamaker constant of the particles in water, λ is the characteristic wavelength for the reaction (100 nm), and b is a constant with a value of 5.32.

Linear superposition approximation was made in the calculation of electrical double layer interaction, $V_R(h)$ [30]

$$V_R(h) = 32\pi a\varepsilon\left(\frac{kT}{Ze}\right)^2 \gamma^2 \exp(-\kappa h) \tag{4.5}$$

where Z is the valence of ions and equal to 1 in NaCl solution, ε is the dielectric constant of water, e is the elementary charge, κ is the Debye-Hückel parameter, and γ is the reduced surface potential, which can be calculated using the equation

$$\gamma = \tanh\left(\frac{Ze\varphi}{4kT}\right) \tag{4.6}$$

with φ is the surface potential.

The function $\beta(h)$ is used to correct for the hydrodynamic interactions between two approaching particles.[19, 31]

$$\beta(h) = \frac{6\left(\frac{h}{a}\right)^2 + 13\left(\frac{h}{a}\right) + 2}{6\left(\frac{h}{a}\right)^2 + 4\left(\frac{h}{a}\right)} \tag{4.7}$$

In this study, ζ potentials, which were converted from the EPMs, were used instead of surface potentials for the calculation of $V_R(h)$.[32] Logarithmic regression analysis was performed on the ζ potentials to derive the relationship between ζ potential and NaCl concentration. This relationship was then used for the calculation of $V_R(h)$. Using the Hamaker constant for citrate-coated AgNPs in aqueous solutions, which is part of the expression for $V_A(h)$, as the single fitting parameter, the experimentally obtained attachment efficiencies were fitted with the theoretical attachment efficiencies (Equation 4.3).

The solid line in Figure 4.8a represents the best-fitting theoretical attachment efficiencies derived using a Hamaker constant of 3.7×10^{-20} J for citrate-coated AgNPs in aqueous solutions. This value falls within the range of values $(2.9 \pm 0.8) \times 10^{-20}$ J suggested by Fornasiero and Grieser.[33] Furthermore, Figure 4.8a shows that the experimentally obtained attachment efficiencies are in remarkable agreement with DLVO simulations. One of the key assumptions of DLVO theory is that the charge on the particle surface is uniformly distributed.[32] Previously, discrepancies between experimental results and theoretical simulations had been observed for other types of particles and these discrepancies were attributed to the heterogeneity of surface charge [32]. In contrast, the good agreement between the experimental results and theoretical simulation in this study may be an indication of a uniform charge distribution on the citrate-coated AgNP surface.

4.3.6. Aggregation Kinetics of Citrate-Coated AgNPs in Divalent Electrolyte Solutions

The aggregation kinetics of citrate-coated AgNPs in $CaCl_2$ and $MgCl_2$ electrolytes are presented in Figure 4.8b. Similar to the inverse stability profile obtained in the presence of NaCl (Figure 4.8a), the presence of the reaction- and diffusion-limited regimes showed that the aggregation kinetics of citrate-coated AgNPs in $CaCl_2$ and $MgCl_2$ electrolytes are controlled by electrostatic interactions. The CCCs of citrate-coated AgNPs in the presence of $CaCl_2$ and $MgCl_2$ were 2.1 mM and 2.7 mM, respectively. These values are much smaller than the CCC obtained in NaCl, since Ca^{2+} and Mg^{2+} ions can neutralize the surface charge of citrate-coated AgNPs through specific interactions with the carboxyl groups of the adsorbed citrate molecules. The results from the aggregation experiments corroborate with the EPM measurements which showed that mobilities of citrate-coated nanoparticles were considerably less negative in the presence of $CaCl_2$ and $MgCl_2$ than in NaCl (Figure 4.1b). In addition, the CCC of citrate-coated AgNPs in $CaCl_2$ is lower than that in $MgCl_2$. This disparity in CCCs is likely due to Ca^{2+} ions having a higher propensity to form complexes with citrate compared with Mg^{2+} ions, as evident from the higher stability constant of monodentate calcium citrate complexes compared to monodentate magnesium-citrate complexes at 0 mM ionic strength and 25°C ($10^{1.4}$ *vs.* $10^{1.0}$).[34] Therefore, Ca^{2+} ions are expected to be more efficient than Mg^{2+} ions in neutralizing the surface charge of citrate-coated AgNPs.

4.3.7. Comparing Aggregation Kinetics of PVP-Coated AgNPs with Citrate-Coated AgNPs

Figure 4.9 presents the inverse stability profiles of PVP- and citrate-coated AgNPs in NaCl and $CaCl_2$ electrolytes. The total PVP concentration in the PVP-coated AgNP suspensions was 0.88 mg/L TOC, which is calculated to be equivalent to 0.14 μM PVP by using a PVP MW of 10 kDa. Therefore, the molar concentration of PVP in the suspensions is comparable to that of citrate in the citrate-coated AgNP suspensions (0.13 μM). When similar concentrations of capping agents were used, the PVP-coated AgNPs were more stable than citrate-coated AgNPs in both electrolytes, as indicated by the considerably higher CCCs of PVP-coated AgNPs. In the presence of NaCl, the CCC of PVP-coated AgNPs was 111.5 mM, compared to 47.6 mM for the citrate-coated AgNPs. In the presence of $CaCl_2$, the CCCs of PVP- and citrate-coated AgNPs were 4.9 mM and 2.1 mM, respectively.

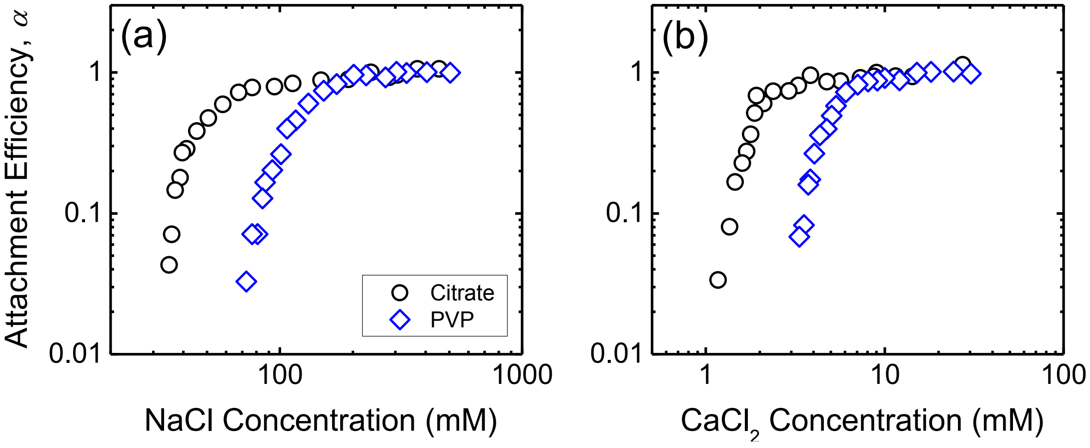

Figure 4.9. Attachment efficiencies of citrate- and PVP-coated AgNPs as functions of (a) NaCl and (b) $CaCl_2$ concentrations at pH 7.0. The attachment efficiencies of citrate-coated AgNPs in a and b are reproduced from Figures 4.8a and b, respectively. For citrate-coated AgNPs, the citrate concentration in the suspension was 0.13 μM. For PVP-coated AgNPs, the PVP concentration in the suspension was 0.88 mg/L TOC (equivalent to 0.14 μM PVP).

Because PVP is an amphiphilic, non-charged polymer, the adsorption of PVP on AgNPs is likely to result in steric repulsion. Since the PVP concentration in the suspension was relatively low (0.88 mg/L TOC), it is expected that the AgNPs were only partially coated with PVP. Thus, sufficient space was likely to be available for PVP polymers to lie relatively flat on the nanoparticle surface with some polymer segments protruding into the bulk solution.[35] However, the existence of the reaction- and diffusion-limited regimes in the inverse stability profiles in both NaCl and $CaCl_2$ solutions indicated that electrostatic interaction still played a significant role in controlling the stability of PVP-coated AgNPs. Trace amount of residual side products from the AgNP synthesis process on the nanoparticle surface are likely the origin of the negative surface charge of the PVP-coated AgNPs.

At higher PVP concentrations, the PVP coverage will be increased and significant sections of adsorbed PVP polymers will be expected to extend into the bulk solution,[35] thus leading to steric repulsion to become the major contributor to the stability of PVP-coated AgNPs. In the study of Badawy *et al.*[11], the stability of AgNPs in PVP solutions with a concentration of 2,500 mg/L, which is much higher than that used in this study, was investigated. The authors found that the ζ potential, which was close to neutral (*ca.* –7 mV), and hydrodynamic diameter of PVP-coated AgNPs remained constant over a wide range of pH conditions. Their observation confirmed that steric repulsion was the dominant contributor to the high stability of the AgNPs and that the contribution by electrostatic interactions was minor at elevated PVP concentrations.

4.3.8. Influence of Humic Acid on Aggregation Kinetics of Citrate- and PVP-Coated AgNPs

The aggregation kinetics of citrate-coated AgNPs in the absence and presence of humic acid are presented as functions of NaCl concentrations in Figure 4.10a. The presence of humic acid (1 mg/L TOC) increased the CCC from 47.6 mM to 72.1 mM NaCl. Since humic acid contains negatively charged carboxyl groups, the adsorption of these macromolecules on the surface of citrate-coated AgNPs is very likely to result in electrosteric repulsion and thus increases the stability of the citrate-coated AgNPs. Although both citrate-coated AgNPs and humic acid are negatively charged at pH 7.0, humic acid may still adsorb on the modified nanoparticles through hydrophobic interaction. It is also possible that the nanoparticles were not completely coated with citrate and there were still available surface sites for humic acid adsorption to take place

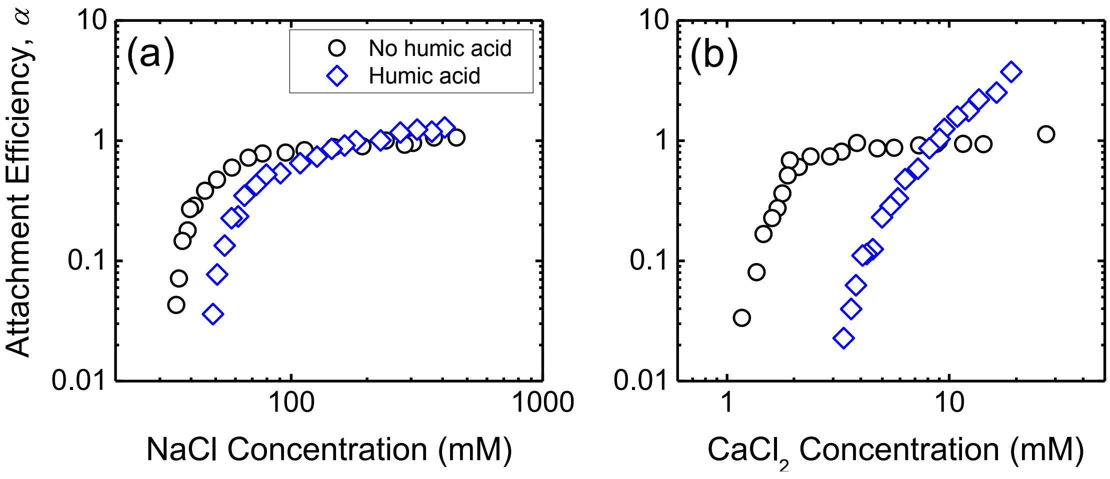

Figure 4.10. Attachment efficiencies of citrate-coated AgNPs in the absence and in the presence of humic acid (1 mg/L TOC) as functions of (a) NaCl and (b) $CaCl_2$ concentrations at pH 7.0. The attachment efficiencies of citrate-coated AgNPs in the absence of humic acid in a and b are reproduced from Figures 4.8a and b, respectively. For all experiments, the citrate concentration in the suspension was 0.13 µM.

The aggregation behavior of citrate-coated AgNPs in the presence of humic acid and $CaCl_2$ is dissimilar from that in NaCl, as shown in Figure 4.10b. Specifically, no distinct reaction- and diffusion-limited regimes were observed in the inverse stability profile. When the concentration of $CaCl_2$ was smaller than 9 mM, the citrate-coated AgNPs were more stable in the presence than in the absence of humic acid due to electrosteric stabilization. At $CaCl_2$ concentrations above 9 mM, the attachment efficiencies were higher than unity and increased with increasing $CaCl_2$ concentration. Similarly, enhanced aggregation of fullerene,[22] gold,[36] and silicon[37] nanoparticles was previously observed in the presence of humic acid at high $CaCl_2$ concentrations. Chen and Elimelech[22] hypothesized that the enhanced aggregation was due to interparticle bridging of nanoparticles by humic acid aggregates which were created through the complex formation between humic acid macromolecules and Ca^{2+} ions.

PVP-coated AgNPs exhibited similar aggregation behavior in the presence of humic acid as that of citrate-coated AgNPs in both NaCl and $CaCl_2$ electrolytes (Figure 4.11). In NaCl solutions, the presence of humic acid increased the CCC of PVP-coated AgNPs from 111.5 mM to 155.1 mM. In the presence of $CaCl_2$, the PVP-coated AgNPs were more stable in the presence than in the absence of humic acid at $CaCl_2$ concentrations below 18 mM. At $CaCl_2$ concentrations above 18 mM, enhanced aggregation of PVP-coated AgNPs occurred in the presence of humic acid. However, even at the highest $CaCl_2$ concentration employed (30 mM), the enhancement in aggregation kinetics of PVP-coated AgNPs (α = 1.6) was not as dramatic as that of citrate-coated AgNPs (α = 3.7 at 19 mM $CaCl_2$). The smaller enhancement in aggregation kinetics may be an indication that the adsorbed PVP can cause steric hindrance to interparticle bridging by the humic acid aggregates.

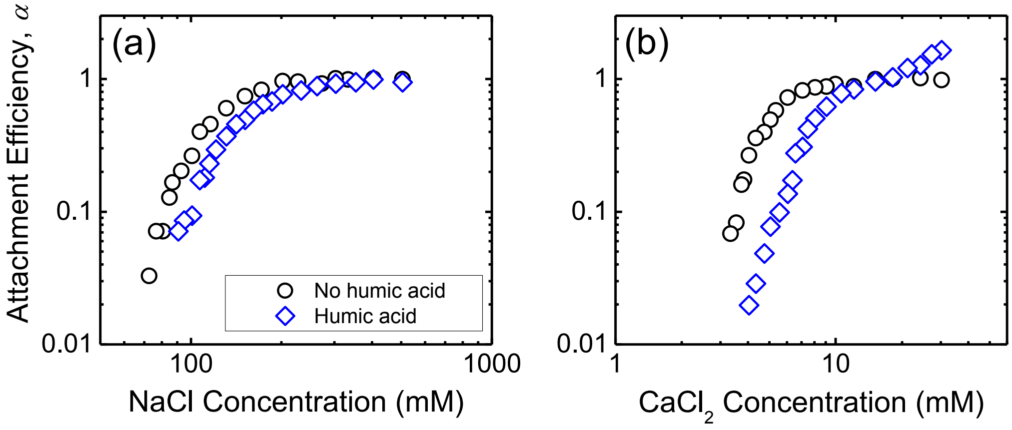

Figure 4.11. Attachment efficiencies of PVP-coated AgNPs in the absence and in the presence of humic acid (1 mg/L TOC) as functions of (a) NaCl and (b) $CaCl_2$ concentrations at pH 7.0. The attachment efficiencies of PVP-coated AgNPs in the absence of humic acid in a and b are reproduced from Figures 4.9a and b, respectively. For all experiments, the PVP concentration in the suspension was 0.88 mg/L TOC.

4.3.9. Environmental Implications

The aggregation kinetics of citrate-coated AgNPs are shown to be in excellent agreement with DLVO theory. The Hamaker constant of citrate-coated AgNPs derived from this study is a critical parameter for the modeling and prediction of the fate and transport of these nanoparticles in aquatic systems.[38] PVP-coated AgNPs are significantly more stable than citrate-coated AgNPs, likely due to the steric repulsion imparted by the adsorbed PVP molecules. Since the CCCs for both AgNPs are much higher than typical monovalent and divalent salt concentrations in freshwater systems, both AgNPs are expected to be highly mobile in these environments. While humic acid elevates the colloidal stability of both citrate- and PVP-coated AgNPs in NaCl and at low concentrations of $CaCl_2$, it enhances the aggregation kinetics at high $CaCl_2$ concentrations. Similar studies should be conducted to establish the effects of other key components of NOM, such as fulvic acids and polysaccharides, on the aggregation kinetics of modified AgNPs. In addition, further research is required to assess the long-term reversibility of the adsorption of citrate and PVP on AgNPs, which will have important implications for the aggregation behavior and persistence of these nanoparticles in aquatic systems.

4.4. References

1. McFarland, A. D.; Van Duyne, R. P., Single silver nanoparticles as real-time optical sensors with zeptomole sensitivity. *Nano Lett* **2003,** *3*, (8), 1057-1062.

2. Panáček, A.; Kvítek, L.; Prucek, R.; Kolár, M.; Večcřová, R.; Pizúrová, N.; Sharma, V. K.; Nevěčná, T. j.; Zbořil, R., Silver colloid nanoparticles: synthesis, characterization, and their antibacterial activity. *J. Phys. Chem. B* **2006,** *110*, 16248-16253.

3. Sharma, V. K.; Yngard, R. A.; Lin, Y., Silver nanoparticles: Green synthesis and their antimicrobial activities. *Advances in Colloid and Interface Science* **2009,** *145*, (1-2), 83-96.

4. Sondi, I.; Salopek-Sondi, B., Silver nanoparticles as antimicrobial agent: a case study on *E. coli* as a model for Gram-negative bacteria. *Journal of Colloid and Interface Science* **2004,** *275*, (1), 177-182.

5. Schimpf, M. E.; Caldwell, K.; Giddings, J. C., *Field flow fractionation handbook*. Wiley-Interscience: New York, 2000; p xviii, 592 p.

6. Benn, T. M.; Westerhoff, P., Nanoparticle silver released into water from commercially available sock fabrics. *Environ Sci Technol* **2008,** *42*, (11), 4133-4139.

7. Li, Q. L.; Mahendra, S.; Lyon, D. Y.; Brunet, L.; Liga, M. V.; Li, D.; Alvarez, P. J. J., Antimicrobial nanomaterials for water disinfection and microbial control: Potential applications and implications. *Water Research* **2008,** *42*, (18), 4591-4602.

8. AshaRani, P. V.; Mun, G. L. K.; Hande, M. P.; Valiyaveettil, S., Cytotoxicity and Genotoxicity of Silver Nanoparticles in Human Cells. *ACS Nano* **2009,** *3*, (2), 279-290.

9. Kim, S.; Choi, J. E.; Choi, J.; Chung, K. H.; Park, K.; Yi, J.; Ryu, D. Y., Oxidative stress-dependent toxicity of silver nanoparticles in human hepatoma cells. *Toxicol in Vitro* **2009,** *23*, (6), 1076-1084.

10. Choi, O.; Hu, Z. Q., Size dependent and reactive oxygen species related nanosilver toxicity to nitrifying bacteria. *Environ Sci Technol* **2008,** *42*, (12), 4583-4588.

11. El Badawy, A. M.; Luxton, T. P.; Silva, R. G.; Scheckel, K. G.; Suidan, M. T.; Tolaymat, T. M., Impact of Environmental Conditions (pH, Ionic Strength, and Electrolyte Type) on the Surface Charge and Aggregation of Silver Nanoparticles Suspensions. *Environ Sci Technol* **2010,** *44*, (4), 1260-1266.

12. Li, X.; Lenhart, J. J.; Walker, H. W., Dissolution-Accompanied Aggregation Kinetics of Silver Nanoparticles. *Langmuir* **2010,** *26*, (22), 16690-16698.

13. Chen, K. L.; Smith, B. A.; Ball, W. P.; Fairbrother, D. H., Assessing the colloidal properties of engineered nanoparticles in water: case studies from fullerene C-60 nanoparticles and carbon nanotubes. *Environmental Chemistry* **2010,** *7*, (1), 10-27.

14. Yin, Y.; Li, Z.-Y.; Zhong, Z.; Gates, B.; Xia, Y.; Venkateswaran, S., Synthesis and characterization of stable aqueous dispersions of silver nanoparticles through the Tollens process. *J. Matter. Chem.* **2002,** *12*, 552-527.

15. Kvítek, L.; Prucek, R.; Panáek, A.; Novotný, R.; Hrbáč, J.; Zbořil, R., The influence of complexing agent concentration on particle size in the process of SERS active silver colloid synthesis. *J. Mater. Chem* **2005,** *15*, 1099-1105.

16. Method 3051A: Microwave assisted acid digestion of sediments, sludges, soils, and oils. In *Test Methods for Evaluating Solid Waste, Physical/Chemical Methods*, Environmental Protection Agency: 2007.

17. Hong, S. K.; Elimelech, M., Chemical and physical aspects of natural organic matter (NOM) fouling of nanofiltration membranes. *Journal of Membrane Science* **1997,** *132*, (2), 159-181.

18. Ottewill, R. H.; Shaw, J. N., Electrophoretic Studies On Polystyrene Latices. *J. Electroanal. Chem.* **1972,** *37*, (Jun), 133-142.

19. Chen, K. L.; Elimelech, M., Aggregation and Deposition Kinetics of Fullerene (C60) Nanoparticles. *Langmuir* **2006,** *22*, (26), 10994-11001.

20. Chen, K. L.; Mylon, S. E.; Elimelech, M., Aggregation kinetics of alginate-coated hematite nanoparticles in monovalent and divalent electrolytes. *Environ Sci Technol* **2006,** *40*, (5), 1516-1523.

21. Holthoff, H.; Egelhaaf, S.; Borkovec, M.; Schurtenberger, P.; Sticher, H., Coagulation rate measurements of colloidal particles by simultaneous static and dynamic light scattering. *Langmuir* **1996,** *12*, (23), 5541-5549.

22. Chen, K. L.; Elimelech, M., Influence of humic acid on the aggregation kinetics of fullerene (C-60) nanoparticles in monovalent and divalent electrolyte solutions. *Journal of Colloid and Interface Science* **2007,** *309*, (1), 126-134.

23. FIZ Karlsruhe, ICSD Web, Database #44387. http://icsd.fiz-karlsruhe.de/

24. Benjamin, M. M., *Water Chemistry*. Boston: McGraw-Hill: 2002.

25. Liu, J.; Sonshine, D. A.; Shervani, S.; Hurt, R. H., Controlled release of biologically active silver from nanosilver surfaces. *ACS Nano* **2010,** *4*, (11), 6903-13.

26. Liu, J. Y.; Hurt, R. H., Ion Release Kinetics and Particle Persistence in Aqueous Nano-Silver Colloids. *Environ Sci Technol* **2010,** *44*, (6), 2169-2175.

27. Kittler, S.; Greulich, C.; Diendorf, J.; Koller, M.; Epple, M., Toxicity of Silver Nanoparticles Increases during Storage Because of Slow Dissolution under Release of Silver Ions. *Chemistry of Materials* **2010,** *22*, (16), 4548-4554.

28. Mcgown, D. N. L.; Parfitt, G. D., Improved Theoretical Calculation of Stability Ratio for Colloidal Systems. *Journal of Physical Chemistry* **1967,** *71*, (2), 449-&.

29. Gregory, J., Approximate Expressions for Retarded van der Waals Interaction. *Journal of Colloid and Interface Science* **1981,** *83*, (1), 138-145.

30. Gregory, J., Interaction of Unequal Double-Layers at Constant Charge. *Journal of Colloid and Interface Science* **1975,** *51*, (1), 44-51.

31. Honig, E. P.; Roeberse.Gj; Wiersema, P. H., Effect of Hydrodynamic Interaction on Coagulation Rate of Hydrophobic Colloids. *Journal of Colloid and Interface Science* **1971,** *36*, (1), 97-109.

32. Elimelech, M.; Gregory, J.; Jia, X.; Williams, R. A., *Particle deposition and aggregation: measurement, modelling, and simulation*. Butterworth-Heinemann: Oxford; Boston, 1995; p xv, 441 p.

33. Fornasiero, D.; Grieser, F., The Kinetics of Electrolyte Induced Aggregation of Carey Lea Silver Colloids. *Journal of Colloid and Interface Science* **1991,** *141*, (1), 168-179.

34. Martell, A. E.; Smith, R. M.; Motekaitis, R. J., NIST Critically Selected Stability Constants of Metal Complexes Database. In National Institute of Science and Technology: Gaithersburg, MD, 2004.

35. Robinson, S.; Williams, P. A., Inhibition of protein adsorption onto silica by polyvinylpyrrolidone. *Langmuir* **2002,** *18*, (23), 8743-8748.

36. Stankus, D. P.; Lohse, S. E.; Hutchison, J. E.; Nason, J. A., Interactions between Natural Organic Matter and Gold Nanoparticles Stabilized with Different Organic Capping Agents. *Environ Sci Technol* **2010**, ASAP.

37. Liu, X.; Wazne, M.; Chou, T.; Xiao, R.; Xu, S., Influence of Ca2+ and Suwannee River Humic Acid on aggregation of silicon nanoparticles in aqueous media. *Water Research* **2011,** *45*, (1), 105-112.

38. Petosa, A. R.; Jaisi, D. P.; Quevedo, I. R.; Elimelech, M.; Tufenkji, N., Aggregation and Deposition of Engineered Nanomaterials in Aquatic Environments: Role of Physicochemical Interactions. *Environ Sci Technol* **2010,** *44*, (17), 6532-6549.

Chapter 5. Heteroaggregation Reduces Antibacterial Activity of Silver Nanoparticles: Evidence for Nanoparticle–Cell Proximity Effects*

---

*This chapter will be submitted as a manuscript with co-authors Michael McCaffery and Kai Loon Chen to *Environmental Science and Technology Letters*. Co-author Michael McCaffery provided cryogenic-TEM images and helped with minor editing of the manuscript. Co-author Kai Loon Chen helped with data interpretation and manuscript editing.

5.1. Introduction

Due to their antimicrobial properties, silver nanoparticles (AgNPs) are being used as deodorizers and antimicrobial agents in consumer products, such as socks, bandages, and food containers.[1-3] It has been estimated that about 320 tons of AgNPs are currently produced and used worldwide each year.[4] Through the use and disposal of silver-containing products, AgNPs are likely to be released into the environment[1, 4-7] and thus may cause adverse effects on the environment and on human health.[3, 8]

While various mechanisms have been proposed for the cytotoxicity of AgNPs,[3, 9-18] the dissolution of AgNPs resulting in the release and cellular uptake of Ag^+ ions has been shown to be one of the key mechanisms for the inactivation of microorganisms.[3, 12, 15, 17, 18] Once Ag^+ ions are released,[19-21] they can bind to sulfur- and phosphorus-containing compounds (*e.g.*, proteins and DNA) located inside the cells or on the cell membranes.[3, 10, 22] These interactions could affect cellular processes, such as respiration and division, and thus eventually lead to cell death.[3, 10, 22] Recently, the close proximity between AgNPs and bacterial cells has been discovered to be a critical factor that controls the efficacy of AgNPs to inactivate bacteria.[23-25] Bondarenko *et al.*[23] demonstrated that the toxicity of AgNPs was reduced by more than twenty times when the direct contact between AgNPs and *Escherichia coli* was prevented by using a dialysis membrane to separate the nanoparticles and bacteria in the suspension.[23] McQuillan *et al.*[24] showed that the growth of *E. coli* was completely inhibited under aerobic conditions in the presence of 100 mg/L AgNPs even when the background dissolved silver concentration was not high enough to cause growth inhibition. The authors postulated that the dissolution of the AgNPs that were attached on the cell membranes resulted in a locally high Ag^+ concentration at the nanoparticle–cell interface and hence caused the inactivation of the *E. coli* cells.[24]

When AgNPs are released into the natural and engineered aquatic systems, they are likely to undergo heteroaggregation (or aggregation between two types of colloids) with naturally occurring colloids (NOCs) due to the ubiquity of NOCs.[26-28] Thus, heteroaggregation is expected to be a key process that controls the environmental fate, transport, and toxicity of AgNPs.[29] The effect of heteroaggregation on the antimicrobial activity of AgNPs, however, has not been investigated to date. In light of recent revelations that the antimicrobial properties of AgNPs is strongly dependent on the proximity between AgNPs and cells, it is conceivable that heteroaggregation may prevent the close proximity between AgNPs and bacterial cells and hence diminish the cytotoxicity of the nanoparticles.

In this chapter, it is shown for the first time that heteroaggregation between citrate-coated AgNPs and hematite nanoparticles (HemNPs), a model NOC, can reduce the antimicrobial activity of AgNPs toward *E. coli* cells. AgNPs and HemNPs were allowed to undergo heteroaggregation at three different number concentration ratios to produce heteroaggregates of different conformations. *E. coli* cells were then exposed to these heteroaggregates and the antimicrobial activity of AgNPs was found to depend on the structures of the heteroaggregates. A mechanism for the reduction of the AgNP antimicrobial effects through heteroaggregation was proposed. The results of this study will have important implications for the prediction of the ecological and health impacts of AgNPs and potentially other types of inorganic nanoparticles that can dissolve in aqueous systems.

5.2. Materials and Methods

5.2.1. Preparation of Nanoparticles

Unmodified AgNPs were synthesized by ultrasonicating a mixture of Tollens' reagent and glucose as presented in Chapter 4. To prepare citrate-coated AgNPs, the suspension of unmodified AgNPs (*ca.* 520 mL) was divided into smaller portions. Each portion had a volume of 10 mL and was contained in a 50 mL centrifuge tube. The suspensions in the centrifuge tubes were then centrifuged at 3,650 g (Avanti centrifuge J-20 XPI, Beckman Coulter Inc., Brea, CA) and 15°C for 60 min. After centrifugation, 9 mL supernatant was withdrawn from each centrifuge tube and replaced by the same volume of 1 μM trisodium citrate solution. This cleaning process was repeated twice. In order to concentrate the AgNPs, the suspension was centrifuged for one more time with the same parameters and 9 mL of supernatant was removed. The remaining suspensions (1 mL per one centrifuge tube) were ultrasonicated for *ca.* 2 min to re-suspend the AgNPs on the bottom of the centrifuge tube. The concentrated AgNP suspensions were then mixed and further ultrasonicated for 30 min at 25°C to break up the AgNP aggregates that may have formed during the centrifugation process. The final suspension (herein to be referred to as *AgNP stock suspension*) was divided into three portions with equal volume, contained in tightly capped Pyrex bottles, and stored in the dark at 4°C. The mass concentration of AgNPs in the stock suspension was determined to be 58.8 mg/L through inductively coupled plasma mass spectrometry (ICP-MS, PerkinElmer Elan DRC II). Details for the determination of dissolved silver in the suspension of interested was described in Chapter 4. HemNPs were synthesized through the forced hydrolysis of $FeCl_3$[30-32] and the mass concentration of HemNPs in the stock suspension was determined to be 4.4 g/L through gravimetric analysis. The experiments in Chapter 2 and Chapter 4 have shown, through transmission electron microscopy (TEM) imaging, that both AgNPs and HemNPs synthesized using these methods were mostly spherical. The hydrodynamic diameters of AgNPs and HemNPs were determined by dynamic light scattering (DLS) (BI-200SM and BI-9000AT, Brookhaven, NY) to be 64.6 nm and 82.4 nm, respectively. The number concentrations of the AgNPs and HemNPs in their respective stock suspensions were calculated to be 3.97×10^{13} particles/L and 2.83×10^{15} mg/L.

5.2.2. Electrophoretic Mobility Measurements

The electrophoretic mobilities (EPMs) of the citrate-coated AgNPs and HemNPs were measured in deionized (DI) water (Millipore, MA) with no pH adjustment (*ca.* pH 5.5) at 25°C using a zeta potential analyzer (ZetaPALS, Brookhaven, NY). The concentrations of AgNPs and HemNPs used for these measurements were 2.6 mg/L and 1.5 mg/L, respectively. For each type of nanoparticles, at least three nanoparticle samples were prepared and 10 EPM measurements were performed on each sample. The measured EPMs of AgNPs and HemNPs were -2.68×10^{-8} $m^2V^{-1}s^{-1}$ (standard deviation = 0.17×10^{-8} $m^2V^{-1}s^{-1}$) and 1.1×10^{-8} $m^2V^{-1}s^{-1}$ (standard deviation = 0.48×10^{-8} $m^2V^{-1}s^{-1}$), respectively.

5.2.3. Heteroaggregation of AgNPs and HemNPs

The heteroaggregation of AgNPs and HemNPs was investigated by preparing binary suspensions composed of citrate-coated AgNPs and HemNPs in DI water without pH adjustment (*ca.* pH 5.5). Since AgNPs and HemNPs were oppositely charged under such conditions, they underwent favorable heteroaggregation due to electrostatic attraction. For the heteroaggregation experiments, the concentration of AgNPs was fixed at 2.6 mg/L (1.75 × 10^{12} particles/L) and three concentrations of HemNPs (1.5, 6.0, and 20.0 mg/L or 9.66 × 10^{11}, 3.86 × 10^{12}, and 1.29 × 10^{13} particles/L, respectively) were employed in order to allow for heteroaggregation to take place at low, medium, and high HemNP/AgNP number concentration ratios (*i.e.*, 0.6, 2.2, and 7.4, respectively). During the heteroaggregation process, the intensity-weighted hydrodynamic diameters of the heteroaggregates were measured every 15 s through time-resolved DLS. Details of the light scattering setup and time-resolved DLS measurements were described in Chapter 2.

For the heteroaggregation experiments, predetermined volumes of (i) DI water, (ii) AgNP stock suspension, and (iii) diluted HemNP stock suspensions were added into a disposable borosilicate vial (VWR). The mixture was then briefly vortexed and immediately inserted into the light scattering system for DLS measurements. The vials were thoroughly clean with a cleaning solution (Merck KGaA, Darmstadt, Germany) and DI water before being used.

Based on the results from DLS measurement, three HemNP/AgNP ratios (*i.e.*, 0.4, 2.2, and 13.0) were selected to evaluate the effect of heteroaggregation on the antimicrobial activity of AgNPs. To prepare the heteroaggregates for toxicity experiments, predetermined volume of DI water was firstly transferred into a 50 mL centrifuge tube. AgNP and HemNP stock suspensions were then added into the centrifuge tube to obtain a AgNP concentration of 2.6 mg/L AgNPs and HemNP concentrations of 1.2, 5.9, and 35.3 mg/L. Up to this point, the volume of the mixture in the centrifuge tube was 8.5 mL. The nanoparticles were allowed to undergo heteroaggregation for 15 min before being used for experiments evaluating the effect of heteroaggregation on the antimicrobial activity of AgNPs.

5.2.4. Preparation of Bacteria

The experiments evaluating the effect of heteroaggregation on the antimicrobial activity of AgNPs were conducted with *Escherichia coli* K-12 (ATCC 25404) bacteria. Fresh *E.coli* colonies were firstly formed overnight on Lysogeny agar plates (prepared from LB Broth, Miller – Fisher and Bacto Agar - Becton, Dickinson and Company, NJ) at 37°C from frozen bacterial culture. The composition of the Lysogeny broth (LB) medium is presented in Table 5.1. The agar plates with the bacterial colonies were sealed with parafilm, stored at 4°C, and used within three days after preparation. To prepare a bacterial suspension, one colony from the agar plate was transferred into 50 mL of LB medium. The mixture was incubated overnight at 37°C and 250 rpm shaking speed. Following that, 50 µL of the overnight culture was transferred into 25 mL of LB medium and the mixture was again incubated at 37°C and 250 rpm shaking speed for about 3 h until the optical density of the bacterial mixture at 600 nm (OD_{600}) reached 0.8 absorbance unit (a.u.) (mid-exponential growth phase).

10 mL of the bacteria culture ($OD_{600} \sim 0.8$) was transferred into two 50 mL centrifuge tubes (5 mL bacterial culture in each tube). After 5 min of centrifugation at 2000 *g* (Avanti centrifuge J-20 XPI, Beckman Coulter Inc., Brea, CA) and 25°C, 4.5 mL of supernatant was removed from each tube and replaced with 3.8 mL of phosphate-reduced Davis minimal medium (herein to be referred to as DM medium) that did not contain glucose to minimize the growth of the bacteria. The DM medium was prepared in our laboratory and its composition is presented in Table 5.1. The DM medium was sterilized by filtering the medium through a 0.22 µm cellulose acetate filter (Corning,

NY) before use. The *E. coli* suspension prepared in the DM medium had an OD_{600} *ca.* 0.9 and will be referred to as the *bacterial stock suspension*.

Table 5.1. Compositions of growth media

Ingredients	Amount (g in 1000 mL DI water)
Lysogeny Broth (LB) medium	
Tryptone	10.0
Yeast extract	5.0
NaCl	10.0
Phosphate-reduced Davis minimal (DM) medium[33]	
K_2HPO_4	0.7
KH_2PO_4	0.2
$(NH_4)_2SO_4$	1.0
Glucose	1.0
Sodium citrate	0.5
$MgSO_4.7H_2O$	0.1

5.2.5. Evaluation of the Effects of Heteroaggregation on Antimicrobial Activity of AgNPs

In these experiments, the *E. coli* bacteria were exposed to AgNPs, HemNPs, AgNP–HemNP heteroaggregates, and $AgNO_3$ in DM medium. The DM medium was used because it has a relatively low ionic strength (*ca*. 43 mM), and hence can minimize the homoaggregation of the nanoparticles during incubation.[33-35] All the experiments were conducted in 50-mL centrifuge tubes. Predetermined volumes of (i) DI water, (ii) nanoparticle stock suspensions or $AgNO_3$ stock solution, (iii) concentrated DM medium (10-time concentrated), and (iv) bacterial stock suspension were transferred into the centrifuge tubes under sterile conditions to obtain the final suspensions (10 mL). The suspensions were incubated for 8 h at 37°C and 250-rpm shaking speed in an incubator (WVR). During incubation, a spectrophotometer (UV 1800, Shimadzu) was used to measure hourly the OD_{600} of the suspensions to construct the growth curves of the *E. coli* cells. For all experiments, the initial OD_{600} of bacteria was *ca.* 0.045, which was 20 times less than that of the bacterial stock suspension. By obtaining the *E. coli* growth curves over a range of AgNP concentrations, it was determined that the lowest AgNP concentration that can completely inhibit the bacterial growth was 2.2 mg/L AgNPs (Figure 5.1). Experiments at AgNP concentrations of 1.47, 1.76, 2.06, 2.50, and 2.79 mg/L presented Figure 5.1 were conducted once. All of the other experiments were conducted at least three times. Abiotic control experiments were also conducted with DM medium only and with 30 mg/L HemNPs in DM medium and to make sure that DM medium and the HemNP stock suspension were free of bacteria. Since the growth curves obtained from abiotic experiments were flat (Figure 5.2), it was concluded that there was no bacterial contamination in both DM medium and HemNP stock suspension.

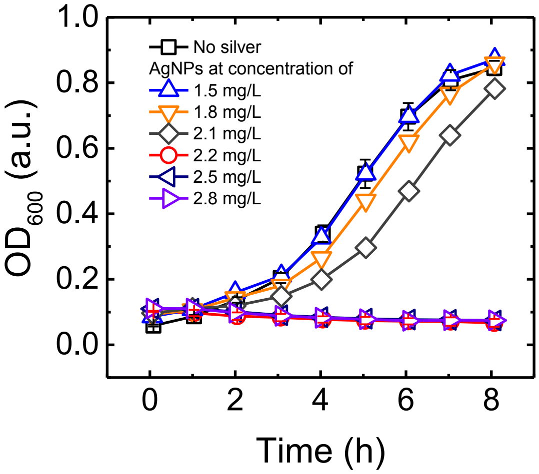

Figure 5.1. Growth curves of *E.coli* at different AgNP concentrations.

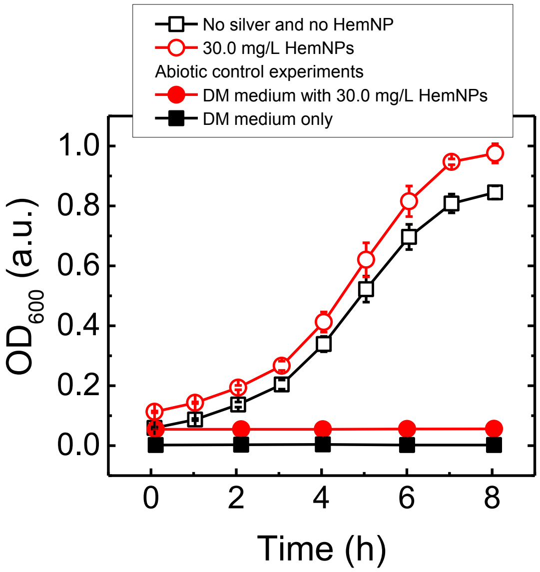

Figure 5.2. Growth curves of *E. coli* bacteria in the absence and presence of 30.0 mg/L HemNPs and growth curves from abiotic control experiments. 30.0 mg/L was the highest HemNP concentration used to evaluate the effects of heteroaggregation on the antimicrobial activity of AgNPs in this study. The "No silver and no HemNP" curve is the "No silver" curve in Figure 5.1. All the experiments were repeated at least three times. Error bars represent standard deviation.

The number of viable bacterial cells in the bacterial suspension was also determined by using a spread plating technique. After the bacteria were incubated with nanoparticles of interest for 2 h, 100 μL of bacterial suspension was diluted 10^3 to 10^6 times with DM medium without glucose. Afterward, 100 μL of the diluted bacterial suspension was spread on the LB agar plates and incubated at 37°C. After *ca.* 20 h of incubation, the number of colonies formed on the agar plates was enumerated and the number of viable bacterial cells in the bacterial suspension before dilution was calculated. For each experimental condition, one bacterial suspension was collected and the number of viable bacterial cells in that suspension was calculated from at least five agar plates.

5.2.6. Determination of Dissolved Silver Concentrations at the Beginning and End of Incubation in the Absence of Bacteria

In order to determine the influence of HemNPs on the dissolved silver concentrations in a suspension, the dissolved silver concentrations at different HemNP/AgNP ratios were measured using the ICP-MS. For this investigation, predetermined volumes of (i) DI water, (ii) AgNP and HemNP stock suspensions, (iii) concentrated DM medium (10-time concentrated), and (iv) diluted mixture of LB and glucose-free DM media was transferred into 50-mL centrifuge tubes under sterile conditions to obtain 1.0 – 1.5 mL of final suspensions having different HemNP/AgNP ratios (*i.e.*, 0.0, 0.4, 2.2, and 13.0). The diluted mixture used in Step iv had the same solution chemistry as the dispensing solution of the bacterial stock suspension. The final suspensions had a AgNP concentration of 2.2 mg/L and a HemNP concentration of 0, 1.0, 5.0, 30.0 mg/L.

Immediately after the diluted mixture of LB and glucose-free DM was added into the centrifuge tubes (t = 0 h), the final suspensions were placed into an incubator for 8 h of incubation at 37°C and 250-rpm shaking speed. At t = 0 h, six 500-μL samples were withdrawn from each of the suspensions containing only AgNPs and no HemNPs (HemNP/AgNP ratio = 0) for the determination of dissolved silver concentration. At t = 8 h, six 500-μL samples were withdrawn from each of the suspensions containing both AgNPs and HemNPs (and also the suspension containing only AgNPs and no HemNPs) for the determination of dissolved silver concentrations.

5.2.7. Cryo-TEM Imaging of Heteroaggregates

The AgNP–HemNP heteroaggregates were observed through cryogenic TEM (cryo-TEM). The procedure is similar to that described in Chapter 2. Briefly, 10 μL of heteroaggregate suspension was deposited on an ionized holey-carbon grid. The grid was blotted with filter paper to obtain a thin water layer and then rapidly plunged into liquid ethane using an automated vitrification robot (VitrobotTM) (FEI Vitrobot Mark IV, Hillsboro, OR). The parameters for blotting and plunging are presented in Table 5.2. Afterward, the vitrified specimen was transferred into the TEM using a cryo workstation filled with liquid nitrogen (Gatan 626 workstation, Pleasanton, CA). A cryo holder (Gatan 626 70° single tilt liquid nitrogen holder, Pleasanton, CA) was used to hold the specimen in the TEM while keeping its temperature during imaging process at –174°C monitored continuously by a cold stage controller (SmartSet 900, Gatan, Pleasanton, CA). The images of the vitreous specimen were taken by an Eagle 2K CCD camera (FEI, Hillsboro, OR) mounted in the on-axis position of a Tecnai 12 TWIN transmission microscope operated at 100 kV.

Table 5.2. Blotting and plunging parameters for Cryo-TEM imaging

Parameter	**Value**
Blot time	1 s
Wait time [a]	0 s
Drain time [b]	0 s
Blot force [c]	1
Blot total [d]	1

[a] Time between blotting.

[b] Wait time between blotting and vitrification

[c] Scale from 0 to 10 with the increment of 1.0

[d] Number of blotting

5.3. Results and Discussion

5.3.1. AgNPs Completely Inhibit Bacterial Growth at Sub-Lethal Concentration of Dissolved Silver in Bulk Solution

The growth curves of *E. coli* in the absence and presence of 2.2 mg/L citrate-coated AgNPs are presented in Figure 5.3. This data was extracted from Figure 5.1. The initial dissolved silver concentration in the DM medium containing 2.2 mg/L AgNPs (t = 0 h) was determined to be 19 μg/L (expressed as mass of Ag, standard deviation = 4 μg/L). After 8 h of incubation, the OD_{600} of the bacterial suspension containing no AgNPs increased by 0.79 absorbance units (a.u.). In contrast, the optical density of the bacterial suspension containing the AgNPs decreased by 0.03 a.u., which indicated that the growth of bacteria was completely inhibited.

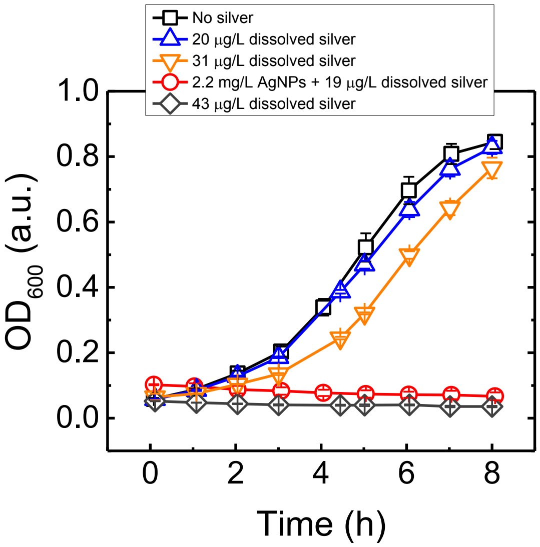

Figure 5.3. Growth curves of *E. coli* in the presence of 2.2 mg/L AgNPs (1.49 × 10^{12} particles/L) and different dissolved silver concentrations. The “No silver” curve is reproduced from Figure 5.1 and is also the “No silver and no HemNP” curve presented in Figure 5.2. The “2.2 mg/L AgNPs + 19 μg/L dissolved silver” is the “2.2 mg/L” curve presented in Figure 5.1. All the experiments were repeated at least three times. Error bars represent standard deviations

In a separate experiment, 2.2 mg/L AgNPs was incubated in a DM medium that did not contain any *E. coli* cells. After 8 h of incubation, the dissolved silver concentration was 18 μg/L (standard deviation = 6 μg/L), which was similar to the initial dissolved silver concentration (= 19 μg/L). Thus, the AgNPs did not to undergo observable dissolution during the 8 h of incubation. The presence of 1.9 mM of citrate in the DM medium was likely to result in the adsorption of a layer of citrate on the AgNP surface that inhibited nanoparticle dissolution.[36]

To determine whether the bacterial growth was inhibited by the dissolved silver present (= 19 μg/L) in the DM medium containing AgNPs, additional *E. coli* growth curves were obtained in the presence of $AgNO_3$ at dissolved silver concentrations of 20 μg/L, 31 μg/L, and 43 μg/L (Figure 5.3). The growth curve obtained in the presence of 20 μg/L dissolved silver and the growth curve obtained in the absence of AgNPs or dissolved silver were identical, thus demonstrating that the dissolved silver concentration of 20 μg/L was not high enough to retard bacterial growth. Therefore, the complete inhibition of bacterial growth observed previously in the presence of 2.2 mg/L AgNPs cannot be solely explained by the dissolved silver in the DM media (= 19 μg/L). As the dissolved silver concentration was increased from 20 to 31 and 43 μg/L, the degree of bacterial growth decreased and the growth was completely inhibited at the dissolved silver concentration of 43 μg/L.

5.3.2. Heteroaggregation with HemNPs Reduces Antibacterial Activity of AgNPs

Figure 5.4a presents the hydrodynamic diameters of AgNPs and HemNPs when prepared separately in DI water, as well as the hydrodynamic diameters when AgNPs and HemNPs were mixed in DI water at a HemNP/AgNP ratio of 2.2. When the AgNPs and

HemNPs were prepared separately, their hydrodynamic diameters remained stable with time. Because both nanoparticles were charged, they were stable to homoaggregation due to electrostatic repulsion as presented in Chapter 2 and Chapter 4. Conversely, when AgNPs and HemNPs were mixed to form a binary suspension, the hydrodynamic diameter increased quickly. Since both nanoparticles were oppositely charged, they underwent fast heteroaggregation through electrostatic attraction.

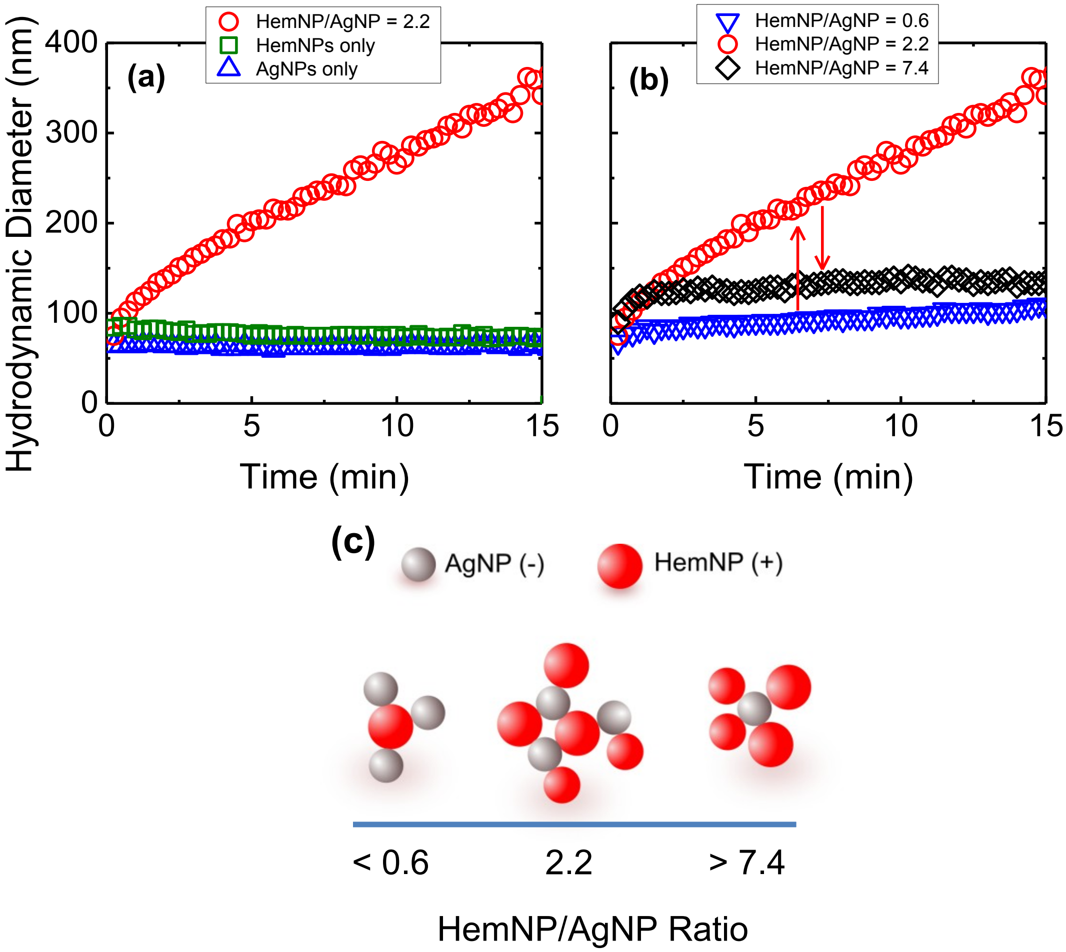

Figure 5.4. (a) Heteroaggregation profile obtained from a binary suspension containing both AgNPs (2.6 mg/L) and HemNPs (6.0 mg/L) resulting in a HemNP/AgNP number concentration ratio of 2.2. Also presented are homoaggregation profiles obtained from suspensions containing either AgNPs (2.6 mg/L) or HemNPs (6.0 mg/L). (b) Heteroaggregation profiles at different HemNP/AgNP ratios. The AgNP number concentration was fixed at 1.75×10^{12} particles/L (2.6 mg/L) while the number concentrations of HemNPs were $9.66 \times 10^{11} – 1.29 \times 10^{13}$ particles/L. All

profiles in (a) and (b) were obtained in DI water at unadjusted pH (*ca.* pH 5.5). (c) Expected heteroaggregate structures at different HemNP/AgNP ratios.

The hydrodynamic diameters measured during the heteroaggregation of AgNPs and HemNPs at HemNP/AgNP ratios of 0.6, 2.2, and 7.4 are presented in Figure 5.4b. It is important to note that, within the range of HemNP/AgNP ratios employed in this study (0.6–7.4), the amount of light scattered by the AgNPs in the binary suspensions was comparable to the light scattered by the HemNPs (Table 5.3). Hence, heteroaggregation between AgNPs and HemNPs will result in an observable increase in the intensity-weighted hydrodynamic diameter. At a low HemNP/AgNP ratio of 0.6, the hydrodynamic diameter was observed to increase slowly. When the HemNP/AgNP ratio was raised to 2.2, conversely, the hydrodynamic diameter increased quickly, which was indicative of fast heteroaggregation. At a high HemNP/AgNP ratio of 7.4, the hydrodynamic diameter increased quickly to 134 nm after 6.5 min and then reached a plateau. The structures of the heteroaggregates formed at these three different HemNP/AgNP ratios are expected to be similar to heteroaggregates composed of oppositely charged colloids[37-39] and are presented in Figure 5.4c. At low HemNP/AgNP ratios (< 0.6), AgNPs outnumbered HemNPs, resulting in the attachment of several AgNPs to each HemNP to form stable, small heteroaggregates.[37] As the HemNP/AgNP ratio was increased to 2.2, however, heteroaggregation occurred quickly due to the plentiful opportunities for the attachment between HemNPs and AgNPs which enabled the fast formation of relatively large heteroaggregates. At high HemNP/AgNP ratios (> 7.4), similar to the case of low HemNP/AgNP ratios, HemNPs outnumbered the AgNPs, thus favoring the formation of stable, small heteroaggregates composed of several HemNPs attached to each AgNP.[38]

Table 5.3. Scattered light intensity (average of four DLS measurements) of AgNPs and HemNPs

Sample	**Scattered light intensity (kcps)**
2.6 mg/L AgNPs$^{(1)}$	353.5
1.5 mg/L HemNPs$^{(2)}$	124.0
6.0 mg/L HemNPs$^{(3)}$	434.8
20.0 mg/L HemNPs$^{(4)}$	1054.0

$^{(1)}$: AgNP concentration used in all heteroaggregation experiments
$^{(2)}$: HemNP/AgNP ratio = 0.6
$^{(3)}$: HemNP/AgNP ratio = 2.2
$^{(4)}$: HemNP/AgNP ratio = 7.4

Based on the results from the heteroaggregation experiments, HemNP/AgNP ratios of 0.4, 2.2, and 13.0 were employed to evaluate the effects of heteroaggregation on the antimicrobial activity of AgNPs. The growth curves of *E. coli* were obtained in the presence of heteroaggregates prepared at these three HemNP/AgNP ratios. The AgNP concentration employed for this series of experiments was 2.2 mg/L (1.49×10^{12} particles/L) while the HemNP concentrations used were 1.0, 5.0, and 30.0 mg/L (6.45×10^{11}, 3.22×10^{12}, and 1.93×10^{13}, respectively). Additional experiments were conducted to verify that the HemNPs even at the highest concentration of 30.0 mg/L did not inhibit the growth of the *E. coli* cells (Figure 5.2). The growth curves of *E. coli* at different HemNP/AgNP ratio is presented in Figure 5.5. The increase in the optical density of the bacterial suspensions in the presence of the AgNP–HemNP heteroaggregates after 2 h ($\Delta OD_{600,\ 2h}$) and 8 h ($\Delta OD_{600,\ 8h}$) of incubation are shown in Figure 5.6. This data was extracted from the growth curves in Figure 5.4. Figure 5.6a shows that heteroaggregation at the high and medium HemNP/AgNP ratios of 13.0 and 2.2, respectively, reduced the antimicrobial activities of the AgNPs considerably, as reflected by the increase in the OD_{600} at both 2 and 8 h. In contrast, heteroaggregation at a low HemNP/AgNP ratio of 0.4 did not result in any observable increase in the OD_{600} at 2 and 8 h, indicating that heteroaggregation at this nanoparticle ratio did not reduce the antimicrobial activity of AgNPs. Interestingly, heteroaggregation at the high HemNP/AgNP ratio of 13.6 resulted in a larger reduction in the antimicrobial activity of AgNPs compared to heteroaggregation at the medium HemNP/AgNP ratio of 2.2. The numbers of viable bacterial cells present in the heteroaggregate suspensions after 2 h of incubation are presented in Figure 5.6b. This figure shows that the number of viable bacterial cells increased with increasing HemNP/AgNP ratios, which is in agreement with the results presented in Figure 5.6a.

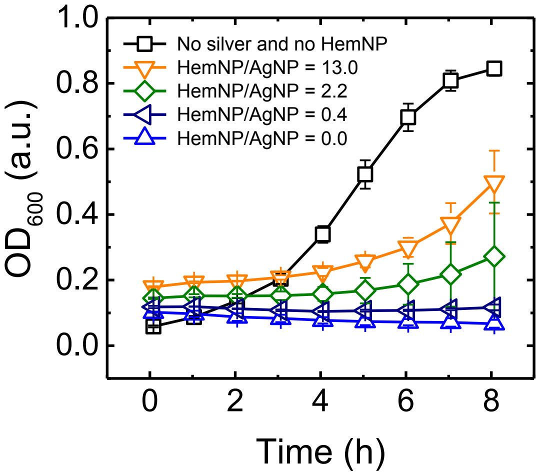

Figure 5.5. Growth curves of *E. coli* bacteria in the presence of AgNP–HemNP heteroaggregates prepared at different HemNP/AgNP ratios. The AgNP and initial dissolved silver concentrations in the growth medium were 2.2 mg/L (1.49×10^{12} particles/L) and 19 μg/L, respectively. The number concentrations of HemNPs were 6.45×10^{11} – 1.93×10^{13} particles/L. The "No silver and no HemNP" is the "No silver" curves in Figure 5.1 and 5.3. It is also the "No silver and no HemNP" curve in Figure 5.2. Error bars represent the standard deviation of at least three repeated experiments.

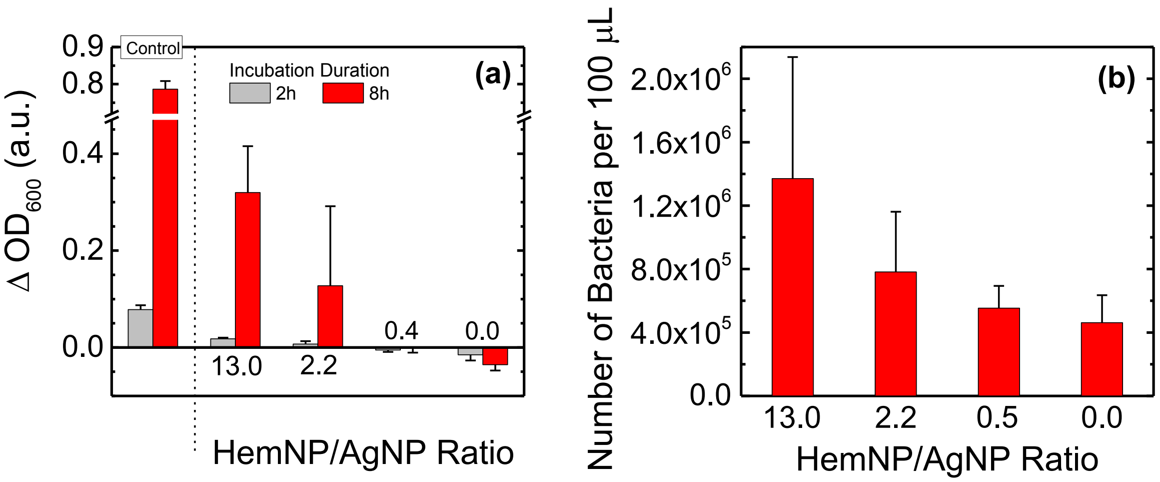

Figure 5.6. (a) Increase in optical density of the bacterial suspensions at 600 nm after 2 h and 8 h of incubation in the presence of heteroaggregates formed at different HemNP/AgNP ratios. Control suspension did not contain AgNPs or HemNPs. All the experiments were repeated at least three times. (b) The number of viable bacterial cells present in the bacterial suspensions containing heteroaggregates formed at different HemNP/AgNP ratios after 2 h of incubation. In (a) and (b), the AgNP number concentration was fixed at 1.49×10^{12} particles/L (or 2.2 mg/L), while the number concentrations of HemNPs were varied. Error bars represent standard deviations.

5.3.3. Heteroaggregation Inhibits Direct Contact or Close Proximity between AgNPs and Bacterial Cells

Since the antimicrobial activity of AgNPs was most greatly reduced in the presence of heteroaggregates formed at the highest HemNP/AgNP ratio of 13.0, cryo-TEM imaging was employed to examine the structure of the heteroaggregates at this nanoparticle ratio. A representative cryo-TEM image of a heteroaggregate is presented in Figure 5.7a. AgNPs can be differentiated from HemNPs in the TEM image since HemNPs had crevices on their surface[40, 41] while the surface of AgNPs was considerably smoother.[42] In addition, since silver is more electron dense than iron due to its higher atomic number (47 *vs.* 26), such that even AgNPs which were smaller than the HemNPs appeared significantly darker than the HemNPs on the TEM images. During cryo-TEM imaging, it was observed that most the AgNPs were in contact with HemNPs and not many isolated AgNPs were found. A considerable number of AgNPs were surrounded by HemNPs to form heteroaggregate structures (Figure 5.7a) similar to that presented in Figure 5.4c at the HemNP/AgNP ratio > 7.4.

In a separate experiment, the influence of heteroaggregation on the concentration of dissolved silver in a DM medium that did not contain *E. coli* cells was investigated. Figure 5.7b presents the dissolved silver concentrations in the medium after 8 h of incubation with the heteroaggregates prepared at a AgNP concentration of 2.2 mg/L and HemNP concentrations of 1.0, 5.0, and 30 mg/L. The dissolved silver concentration was found to decrease as the HemNP/AgNP ratio (or HemNP concentration) was increased. This finding could be explained by the adsorption of dissolved silver on the surface of the HemNPs, which was expected to be coated with citrate that was present in the DM medium. It is important to note that the increase in bacterial growth with increasing HemNP concentration (as shown in Figure 5.6) cannot be explained by the loss in dissolved silver due to the adsorption of silver on the HemNPs since even the dissolved silver concentration in the absence of HemNPs (= 19 μg/L) was not high enough to cause any observable inhibition effect on bacterial growth (as shown in Figure 5.3, 20 μg/L dissolved silver did not inhibit bacterial growth).

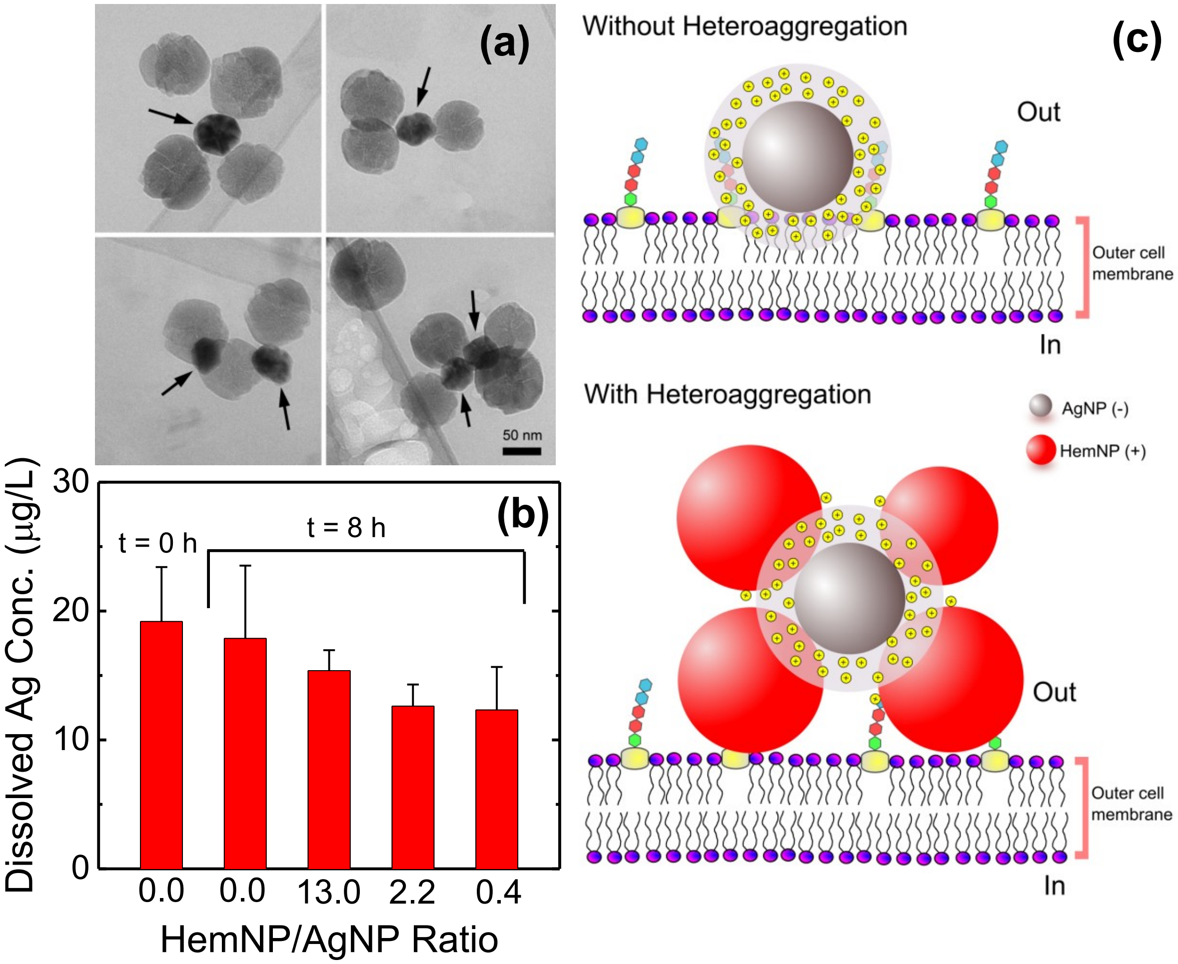

Figure 5.7. Representative cryo-TEM images of heteroaggregates formed at a HemNP/AgNP ratio of 13.0. Arrows point to AgNPs. The heteroaggregates were prepared in DI water at AgNP and HemNP concentrations of 2.6 mg/L (1.75 × 10^{12} particles/L) and 35.3 mg/L (2.27 × 10^{13} particles/L), respectively. (b) Dissolved silver concentrations in DM medium at the beginning of (*t* = 0 h) and the end of incubation (*t* = 8 h) in the absence of bacteria. The AgNP number concentration was fixed at 1.49 × 10^{12} particles/L (or 2.2 mg/L), while the number concentrations of HemNPs were varied. Error bars represent standard deviations. (c) Proposed effects of heteroaggregation on antimicrobial activity of AgNPs.

In light of the observed effects of heteroaggregation on the antimicrobial activity of AgNPs and results from cryo-TEM imaging, a mechanism for the reduction in the antimicrobial activity of AgNPs through heteroaggregation is proposed and illustrated in

Figure 5.7c. Surrounding each AgNP, it is speculated that there is a "cloud" of dissolved silver since silver ions could adsorb on AgNP surface[12, 19, 43] or form complexes with the layer of citrate coating the AgNPs.[36] Furthermore, the silver ions are likely to accumulate in the electric double layer surrounding the negatively charged citrate-coated AgNPs through electrostatic attraction. Thus, the concentration of dissolved silver in the silver cloud is likely to be considerably higher than that in the bulk solution (*i.e.*, far away from the surface of AgNPs). In the absence of HemNPs, AgNPs are able to attach to or come into close proximity with the bacteria and hence the bacteria may be exposed to a dissolved silver concentration that is comparatively higher than that of the bulk solution. Additionally, the low pH environment on the bacterial surface due to the extrusion of H^+ ions by the bacterial cell during aerobic respiration can enhance the dissolution of AgNPs when they are in close proximity with the bacterial surface[3, 20, 23, 24, 44-46] and thus lead to the bacterial cell to be exposed to a higher concentration of dissolved silver.

Conversely, in the presence of high concentrations of HemNPs, as heteroaggregation takes place, the AgNPs are surrounded by HemNPs (Figure 5.7a). Thus, the HemNPs prevent the AgNPs from coming into direct contact or close proximity with the bacterial cells (Figure 5.7c). Thus, the bacterial cell cannot be exposed to the elevated silver concentrations within the silver cloud surrounding the AgNPs.

5.4. References

1. Benn, T. M.; Westerhoff, P., Nanoparticle silver released into water from commercially available sock fabrics. *Environ Sci Technol* **2008,** *42*, (11), 4133-4139.

2. Wijnhoven, S. W. P.; Peijnenburg, W. J. G. M.; Herberts, C. A.; Hagens, W. I.; Oomen, A. G.; Heugens, E. H. W.; Roszek, B.; Bisschops, J.; Gosens, I.; Van de Meent, D.; Dekkers, S.; De Jong, W. H.; Van Zijverden, M.; Sips, A. J. A. M.; Geertsma, R. E.,

Nano-silver - a review of available data and knowledge gaps in human and environmental risk assessment. *Nanotoxicology* **2009,** *3*, (2), 109-U78.

3. Marambio-Jones, C.; Hoek, E. M. V., A review of the antibacterial effects of silver nanomaterials and potential implications for human health and the environment. *Journal of Nanoparticle Research* **2010,** *12*, (5), 1531-1551.

4. Nowack, B.; Krug, H. F.; Height, M., 120 Years of Nanosilver History: Implications for Policy Makers. *Environ Sci Technol* **2011,** *45*, (4), 1177-1183.

5. Farkas, J.; Peter, H.; Christian, P.; Urrea, J. A. G.; Hassellov, M.; Tuoriniemi, J.; Gustafsson, S.; Olsson, E.; Hylland, K.; Thomas, K. V., Characterization of the effluent from a nanosilver producing washing machine. *Environ Int* **2011,** *37*, (6), 1057-1062.

6. Geranio, L.; Heuberger, M.; Nowack, B., The Behavior of Silver Nanotextiles during Washing. *Environ Sci Technol* **2009,** *43*, (21), 8113-8118.

7. Kulthong, K.; Srisung, S.; Boonpavanitchakul, K.; Kangwansupamonkon, W.; Maniratanachote, R., Determination of silver nanoparticle release from antibacterial fabrics into artificial sweat. *Part Fibre Toxicol* **2010,** *7*.

8. Ivask, A.; George, S.; Bondarenko, O.; Kahru, A., Metal-Containing Nano-Antimicrobials: Differentiating the Impact of Solubilized Metals and Particles. In *Nano-Antimicrobials*, Cioffi, N.; Rai, M., Eds. Springer Berlin Heidelberg: 2012; pp 253-290.

9. Sondi, I.; Salopek-Sondi, B., Silver nanoparticles as antimicrobial agent: a case study on *E. coli* as a model for Gram-negative bacteria. *Journal of Colloid and Interface Science* **2004,** *275*, (1), 177-182.

10. Morones, J. R.; Elechiguerra, J. L.; Camacho, A.; Holt, K.; Kouri, J. B.; Ramirez, J. T.; Yacaman, M. J., The bactericidal effect of silver nanoparticles. *Nanotechnology* **2005,** *16*, (10), 2346-2353.

11. Pal, S.; Tak, Y. K.; Song, J. M., Does the antibacterial activity of silver nanoparticles depend on the shape of the nanoparticle? A study of the gram-negative bacterium Escherichia coli. *Applied and Environmental Microbiology* **2007,** *73*, (6), 1712-1720.

12. Lok, C. N.; Ho, C. M.; Chen, R.; He, Q. Y.; Yu, W. Y.; Sun, H.; Tam, P. K. H.; Chiu, J. F.; Che, C. M., Silver nanoparticles: partial oxidation and antibacterial activities. *Journal of Biological Inorganic Chemistry* **2007,** *12*, (4), 527-534.

13. Choi, O.; Hu, Z. Q., Size dependent and reactive oxygen species related nanosilver toxicity to nitrifying bacteria. *Environ Sci Technol* **2008,** *42*, (12), 4583-4588.

14. Navarro, E.; Piccapietra, F.; Wagner, B.; Marconi, F.; Kaegi, R.; Odzak, N.; Sigg, L.; Behra, R., Toxicity of Silver Nanoparticles to Chlamydomonas reinhardtii. *Environ Sci Technol* **2008,** *42*, (23), 8959-8964.

15. Sotiriou, G. A.; Pratsinis, S. E., Antibacterial Activity of Nanosilver Ions and Particles. *Environ Sci Technol* **2010,** *44*, (14), 5649-5654.

16. Levard, C.; Hotze, E. M.; Lowry, G. V.; Brown, G. E., Environmental Transformations of Silver Nanoparticles: Impact on Stability and Toxicity. *Environ Sci Technol* **2012,** *46*, (13), 6900-6914.

17. Xiu, Z. M.; Zhang, Q. B.; Puppala, H. L.; Colvin, V. L.; Alvarez, P. J., Negligible particle-specific antibacterial activity of silver nanoparticles. *Nano Lett* **2012,** *12*, (8), 4271-5.

18. Levard, C.; Mitra, S.; Yang, T.; Jew, A. D.; Badireddy, A. R.; Lowry, G. V.; Brown, G. E., Effect of Chloride on the Dissolution Rate of Silver Nanoparticles and Toxicity to E. coli. *Environ Sci Technol* **2013,** *47*, (11), 5738-5745.

19. Liu, J. Y.; Hurt, R. H., Ion Release Kinetics and Particle Persistence in Aqueous Nano-Silver Colloids. *Environ Sci Technol* **2010,** *44*, (6), 2169-2175.

20. Xiu, Z. M.; Zhang, Q. B.; Puppala, H. L.; Colvin, V. L.; Alvarez, P. J. J., Negligible Particle-Specific Antibacterial Activity of Silver Nanoparticles. *Nano Lett* **2012,** *12*, (8), 4271-4275.

21. Zhang, W.; Yao, Y.; Sullivan, N.; Chen, Y. S., Modeling the Primary Size Effects of Citrate-Coated Silver Nanoparticles on Their Ion Release Kinetics. *Environ Sci Technol* **2011,** *45*, (10), 4422-4428.

22. Bragg, P. D.; Rainnie, D. J., The effect of silver ions on the respiratory chain of Escherichia coli. *Canadian journal of microbiology* **1974,** *20*, (6), 883-9.

23. Bondarenko, O.; Ivask, A.; Kakinen, A.; Kurvet, I.; Kahru, A., Particle-Cell Contact Enhances Antibacterial Activity of Silver Nanoparticles. *Plos One* **2013,** *8*, (5).

24. McQuillan, J. S.; Infante, H. G.; Stokes, E.; Shaw, A. M., Silver nanoparticle enhanced silver ion stress response in Escherichia coli K12. *Nanotoxicology* **2012,** *6*, 857-66.

25. Chen, K. L.; Bothun, G. D., Nanoparticles Meet Cell Membranes: Probing Nonspecific Interactions using Model Membranes. *Environ Sci Technol* **2013**.

26. Elimelech, M.; Gregory, J.; Jia, X.; Williams, R. A., *Particle deposition and aggregation: measurement, modelling, and simulation*. Butterworth-Heinemann: Oxford; Boston, 1995; p xv, 441 p.

27. Lin, W.; Kobayashi, M.; Skarba, M.; Nu, C. D.; Galletto, P.; Borkovec, M., Heteroaggregation in binary mixtures of oppositely charged colloidal particles. *Langmuir* **2006,** *22*, (3), 1038-1047.

28. Chen, K. L.; Smith, B. A.; Ball, W. P.; Fairbrother, D. H., Assessing the colloidal properties of engineered nanoparticles in water: case studies from fullerene C(60) nanoparticles and carbon nanotubes. *Environ Chem* **2010,** *7*, (1), 10-27.

29. Lowry, G. V.; Gregory, K. B.; Apte, S. C.; Lead, J. R., Transformations of Nanomaterials in the Environment. *Environ Sci Technol* **2012,** *46*, (13), 6893-6899.

30. Chen, K. L.; Mylon, S. E.; Elimelech, M., Aggregation kinetics of alginate-coated hematite nanoparticles in monovalent and divalent electrolytes. *Environ Sci Technol* **2006,** *40*, (5), 1516-1523.

31. Chen, K. L.; Mylon, S. E.; Elimelech, M., Enhanced aggregation of alginate-coated iron oxide (hematite) nanoparticles in the presence of calcium, strontium, and barium cations. *Langmuir* **2007,** *23*, (11), 5920-5928.

32. Matijevic, E.; Scheiner, P., Ferric hydrous oxide sols: III. Preparation of uniform particles by hydrolysis of Fe(III)-chloride, -nitrate, and -perchlorate solutions. *Journal of Colloid and Interface Science* **1978,** *63*, (3), 509-524.

33. Lyon, D. Y.; Adams, L. K.; Falkner, J. C.; Alvarez, P. J. J., Antibacterial activity of fullerene water suspensions: Effects of preparation method and particle size. *Environ Sci Technol* **2006,** *40*, (14), 4360-4366.

34. Brunet, L.; Lyon, D. Y.; Hotze, E. M.; Alvarez, P. J.; Wiesner, M. R., Comparative photoactivity and antibacterial properties of C60 fullerenes and titanium dioxide nanoparticles. *Environ Sci Technol* **2009,** *43*, (12), 4355-60.

35. Lyon, D. Y.; Alvarez, P. J., Fullerene water suspension (nC60) exerts antibacterial effects via ROS-independent protein oxidation. *Environ Sci Technol* **2008,** *42*, (21), 8127-32.

36. Liu, J. Y.; Sonshine, D. A.; Shervani, S.; Hurt, R. H., Controlled Release of Biologically Active Silver from Nanosilver Surfaces. *Acs Nano* **2010,** *4*, (11), 6903-6913.

37. Furusawa, K.; Anzai, C., Heterocoagulation Behavior of Polymer Lattices with Spherical Silica. *Colloid Surface* **1992,** *63*, (1-2), 103-111.

38. Yates, P. D.; Franks, G. V.; Biggs, S.; Jameson, G. J., Heteroaggregation with nanoparticles: effect of particle size ratio on optimum particle dose. *Colloid Surface A* **2005,** *255*, (1-3), 85-90.

39. Islam, A. M.; Chowdhry, B. Z.; Snowden, M. J., Heteroaggregation in colloidal dispersions. *Advances in Colloid and Interface Science* **1995,** *62*, (2-3), 109-136.

40. Huynh, K. A.; McCaffery, J. M.; Chen, K. L., Heteroaggregation of Multiwalled Carbon Nanotubes and Hematite Nanoparticles: Rates and Mechanisms. *Environ Sci Technol* **2012,** *46*, (11), 5912-5920.

41. Johnsen, R. E.; Knudsen, K. D.; Molenbroek, A. M., Microstructural changes in porous hematite nanoparticles upon calcination. *J Appl Crystallogr* **2011,** *44*, 495-502.

42. Huynh, K. A.; Chen, K. L., Aggregation Kinetics of Citrate and Polyvinylpyrrolidone Coated Silver Nanoparticles in Monovalent and Divalent Electrolyte Solutions. *Environ Sci Technol* **2011**, (45), 5564-5571.

43. Henglein, A., Colloidal silver nanoparticles: Photochemical preparation and interaction with O-2, CCl4, and some metal ions. *Chemistry of Materials* **1998,** *10*, (1), 444-450.

44. Kemper, M. A.; Urrutia, M. M.; Beveridge, T. J.; Koch, A. L.; Doyle, R. J., Proton Motive Force May Regulate Cell Wall-Associated Enzymes of Bacillus-Subtilis. *J Bacteriol* **1993,** *175*, (17), 5690-5696.

45. Koch, A. L., The Ph in the Neighborhood of Membranes Generating a Protonmotive Force. *J Theor Biol* **1986,** *120*, (1), 73-84.

46. Madigan, M. T.; Martinko, J. M.; Dunlap, P. V.; Clark, D. P., *Biology of Microorganisms, 12th Edition*. Pearson: 2009.

Chapter 6. Conclusions and Key Contributions

6.1. Conclusions

Investigation of the rates and mechanisms of the heteroaggregation between multiwalled CNTs and HemNPs, a model naturally occurring colloid, were as described in Chapter 2. The effect of humic acid on the heteroaggregation rates was also discussed in this chapter. The disaggregation behavior and strength of heteroaggregates composed of multiwalled CNTs and HemNPs were studied in different solution chemistries, and this work has been described in Chapter 3. Chapter 4 describes the influences of different coating agents on the colloidal stability and homoaggregation kinetics of AgNPs in monovalent and divalent electrolyte solutions. Finally, the effects of heteroaggregation on the antimicrobial activity of AgNPs toward *E. coli* are presented in Chapter 5.

As discussed in Chapter 2, the rates and mechanisms of heteroaggregation between oppositely charged CNT and HemNPs at low ionic strength condition were obtained using time-resolved DLS and cryo-TEM imaging. The heteroaggregation rate was found to depend on the CNT/HemNP concentration ratio. Because of the bridging effect, the heteroaggregation rate increased with an initial increase in CNT/HemNP ratio, and then reached a maximum value at an optimal relative concentration. At this CNT/HemNP ratio, the maximum heteroaggregation rate was 3.3 times higher than the favorable homoaggregation rate of HemNPs. Afterward, further increase in CNT/HemNP ratio led to a decrease in heteroaggregation rate, possibly through blocking effect. In the presence of Suwanee River humic acid, the trends in the variation of the CNT–HemNP heteroaggregation rate with relative concentration were similar to that in the absence of humic acid. However, as the Suwanee River humic acid concentration was increased, the maximum aggregate growth rate decreased because of the lessening in the available surface area of the HemNPs that CNTs could attach to through favorable electrostatic interaction. Furthermore, the trends for the heteroaggregation rates in two other binary suspensions (*i.e.*, GO nanosheets + HemNPs and C_{60} nanoparticles + HemNPs) were found to be similar to that of CNTs and HemNPs. This observation likely indicated that C_{60} nanoparticles and GO nanosheets underwent heteroaggregation with HemNPs through similar mechanisms as those for CNTs and HemNPs.

Chapter 3 presents the results obtained from the study of disaggregation of heteroaggregates composed of CNTs and HemNPs using time-resolved DLS and ultrasound. The heteroaggregates were first formed through favorable heteroaggregation, and then disaggregated by ultrasound at different ultrasonication durations. When the solution chemistry was unchanged, the heteroaggregates undergo partial disaggregation and heteroaggregate re-growth was observed after ultrasonication. Conversely, when the pH was raised to 11.0 immediately before ultrasonication, the heteroaggregates were almost completely disaggregated and no aggregation took place after disaggregation. Similarly, the introduction of Suwannee River humic acid immediately before ultrasonication led to a near complete disaggregation of the CNT–HemNP heteroaggregates and no further aggregation occurred after disaggregation. With the consideration of DLVO interactions together with Born repulsion, it was speculated that these changes in solution chemistry reduced the depth of the primary energy minium through the increase in electrostatic repulsion (at elevated pH) or the introduction of electrosteric repulsion (in the presence of humic acid) between CNTs and HemNPs. Hence, the particle–particle bonds within the heteroaggregates were likely to be weakened through the increase in pH or the adsorption of humic acid on the nanoparticles, hence increasing the propensities for the heteroaggregates to underwent disaggregation with the changes in solution chemistry.

The findings from the study on the homoaggregation kinetics of citrate- and PVP-coated AgNPs in monovalent (NaCl) and divalent ($CaCl_2$ and $MgCl_2$) electrolyte solutions using time-resolved DLS are presented in Chapter 4. The homoaggregation kinetics of citrate-coated AgNPs in NaCl were in excellent agreement with the simulations based on DLVO theory, and the derived Hamaker constant of the citrate-coated AgNPs in aqueous solutions was 3.7×10^{-20} J. Divalent electrolytes were more efficient in destabilizing the citrate-coated AgNPs, as indicated by the considerably lower CCCs (2.1 mM $CaCl_2$ and 2.7 mM $MgCl_2$ *vs.* 47.6 mM NaCl). The PVP-coated AgNPs were significantly more stable than citrate-coated AgNPs in both NaCl and $CaCl_2$, which was likely due to steric repulsion imparted by the large, noncharged polymers. The addition of Suwannee River humic acid resulted in the adsorption of the macromolecules on both citrate- and PVP-coated AgNPs. The adsorption of humic acid induces additional electrosteric repulsion that elevated the stability of both nanoparticles in suspensions containing NaCl or low concentrations of $CaCl_2$. Conversely, enhanced aggregation occurred for both nanoparticles at high $CaCl_2$ concentrations due to interparticle bridging by humic acid aggregates.

The effects of heteroaggregation on the antimicrobial activity of citrate-coated AgNPs are presented in Chapter 5. When *E. coli* bacteria prepared in phosphate-reduced Davis minimal medium were exposed to 2.2 mg/L AgNPs, bacterial growth was completely inhibited during the 8 h of incubation. It was also found that the dissolved silver concentration in the bulk solution was not high enough to retard the bacterial growth. As AgNPs underwent heteroaggregation at HemNP/AgNP number concentration ratios of 2.2 and 13.0, the toxicity of AgNPs was reduced. The reduction in the antimicrobial activity of AgNPs was also found to be larger at the HemNP/AgNP ratio of 13.0 than at the ratio of 2.2. At the HemNP/AgNP ratio of 13.0, it was observed through cryo-TEM imaging that a considerable number of AgNPs was surrounded by HemNPs to form small and stable heteroaggregates composed of several HemNPs attached to each AgNP. Surrounding each AgNP, it was speculated that there was a "cloud" containing dissolved silver at concentration higher than that in the bulk solution. In the absence of HemNPs, AgNPs could attach to or come into close proximity with the bacteria. Thus, the bacterial growth was inhibited due to the exposure of bacteria to high dissolved silver concentration in the cloud. As heteroaggregation took place, the HemNPs surrounding AgNPs prevented the AgNPs from having direct contact or being in the close proximity with the bacterial cells. The bacteria therefore could not be exposed to the elevated dissolved silver concentrations in the cloud and the bacterial growth inhibition was reduced.

6.2. Key Contributions

In this dissertation work, homoaggregation, heteroaggregation, and disaggregation experiments were systematically conducted to obtain a better understanding of the behavior of engineered nanomaterials in the aqueous environments. New information regarding the effect of heteroaggregation on the antimicrobial activity of AgNPs was also obtained. Overall, the findings from this dissertation will enable a more accurate prediction of the fate, transport, and effects of engineered nanomaterials in natural and engineered aquatic systems. Specific contributions of this dissertation work are described below:

- **Gained understanding on the heteroaggregation behavior of engineered nanomaterials.** The results presented in this dissertation work showed that the rates of heteroaggregation between nanomaterials of different shapes (*e.g.*, CNTs, C_{60} nanoparticles, and GO nanosheets) and HemNPs depended on the relative concentrations of nanomaterials. An optimal relative concentration was required to achieve fast heteroaggregation rates. This finding is useful not only for the prediction of the environmental fate and transport of engineered nanomaterials in natural aquatic systems, but also for the application of heteroaggregation for the removal of these nanomaterials from industrial wastewaters. HemNPs potentially can be employed in industrial wastewater treatment facilities as a coagulant for the treatment of wastewaters containing negatively charged carbon-based nanomaterials.
- **Provided new insights to the disaggregation of heteroaggregates.** CNT–HemNP heteroaggregates were demonstrated to undergo disaggregation, especially when solution chemistries were changed to enhance the repulsion between CNTs and HemNPs. The CNT–HemNP interactions were speculated to be substantially weakened with the changes in solution chemistry (*e.g.*, by increasing pH or introducing humic acid), thus resulting in an increase in the propensity for the heteroaggregates to undergo disaggregation.
- **Demonstrated that the colloidal stability of silver nanoparticles strongly depends on their coatings.** At similar molar concentrations,

polyvinylpyrrolidone (PVP) was a more effective stabilizer than citrate for AgNPs in both monovalent (NaCl) and divalent ($CaCl_2$ and $MgCl_2$) electrolyte solutions. The findings are not only useful for the prediction of the environmental fate and transport of AgNPs, but also valuable for biomedical or industrial applications, in which AgNPs are required to be stable at high ionic strength conditions.

- **Derived Hamaker constant of citrate-coated AgNPs.** The aggregation behavior of citrate-coated AgNPs was found to be in excellent agreement with the DLVO theory. The Hamaker constant of citrate-coated AgNPs (3.7×10^{-20} J) derived in this work will allow for the modeling of DLVO interactions between citrate-coated AgNPs with other nanoparticles or surfaces in aquatic systems.
- **Demonstrated for the first time that heteroaggregation between citrate-coated AgNPs and HemNPs reduce the antimicrobial activity of AgNPs.** This study showed that AgNP–HemNP heteroaggregation could reduce the antimicrobial activity of AgNPs. The findings suggest that the impacts of AgNPs on microorganisms in natural and engineered aquatic environments could be reduced through heteroaggregation since the concentrations of naturally occurring colloids is much higher than that of AgNPs in these systems. In environmental and biomedical applications using AgNPs as a solution-based disinfectant, the heteroaggregation between AgNPs and naturally occurring colloids should be prevented in order to maximize the antimicrobial activity of AgNPs.

The list of publications and expected publications from this dissertation work is presented below:

1) Huynh, K. A., McCaffery, J. M., and Chen, K. L., Effects of Dimensionality on the Heteroaggregation of Carbon-based Nanomaterials and Hematite Nanoparticles in Aquatic Environments (in preparation). (Chapter 3)
2) Huynh, K. A., McCaffery, J. M., and Chen, K. L., Heteroaggregation Reduces Antimicrobial Activity of Silver Nanoparticles: Evidence for Nanoparticle–Cell Proximity Effects (in preparation). (Chapter 6)
3) Huynh, K. A. and Chen, K. L., Disaggregation of Heteroaggregates Comprising Multiwalled Carbon Nanotubes and Hematite Nanoparticles, *Environmental Science: Process and Impacts* (under revision). (Chapter 3)
4) Huynh, K. A., McCaffery, J. M., and Chen, K. L., Heteroaggregation of Multiwalled Carbon Nanotubes and Hematite Nanoparticles: Rates and Mechanisms, *Environmental Science and Technology*, 2012, 46, 5912–5920. (Chapter 2)

Huynh, K. A. and Chen, K. L., Aggregation Kinetics of Citrate and Polyvinylpyrrolidone Coated Silver Nanoparticles in Monovalent and Divalent Electrolyte Solutions, *Environmental Science and Technology*, 2011, 45, 5564–5571. (Chapter 4)

6.3. Future Work

Because different types of naturally occurring colloids are present in aquatic systems, the heteroaggregation between CNTs and other naturally occurring colloidal particles (other than HemNPs) should be investigated to obtain a better understanding of the environmental fate and transport of CNTs. Additional knowledge of the heteroaggregation process, such as the effects of dimensionality on the mechanisms of heteroaggregation, could be obtained through the cryo-TEM imaging of GO–HemNP and C_{60}–HemNP heteroaggregates. Moreover, it is plausible that, in binary systems composed of engineered nanoparticles and naturally occurring colloids, homoaggregation of nanoparticles and colloids can take place concurrently with the heteroaggregation process, especially under high ionic strength conditions. Thus, further study on the simultaneous homoaggregation and heteroaggregation processes is needed. In this dissertation work, the disaggregation behavior and strength of heteroaggregates were investigated using only heteroaggregates prepared at the optimal CNT/HemNP ratio that resulted in fast heteroaggregation. Therefore, effects of heteroaggregate structure on heteroaggregate strength should be evaluated through further disaggregation experiments using heteroaggregates prepared at different CNT/HemNP ratios.

In aquatic environments, the surface properties of engineered nanomaterials can change dramatically due to the adsorption/desorption of natural organic matter. Thus, studies of homoaggregation kinetics of modified AgNPs in the presence of other key components of natural organic matter, such as fulvic acids and polysaccharides, are needed. Furthermore, the long-term reversibility of the adsorption of citrate and PVP on AgNPs should be accessed to understand the long-term colloidal stability of AgNPs in the environment. In addition, additional studies can be conducted to understand the effects of heteroaggregation on the antimicrobial activity of AgNPs modified with different coating agents.

Curriculum Vitae

KHANH AN HUYNH

an.huynh@jhu.edu /www.anhuynh.com

EDUCATION

Ph.D. in Environmental Engineering, expected 2014 – Johns Hopkins University, Baltimore, MD
Advisor: Professor Kai Loon Chen
Dissertation title: *Heteroaggregation Between Engineered Nanoparticles and Hematite Nanoparticles in Aquatic Environments*

M.S.E. in Environmental Engineering, 2010 – Johns Hopkins University, Baltimore, MD

M.Eng. in Environmental Engineering, 2008 – Korea University, Seoul, South Korea
Advisor: Professor Jeehyeong Khim
Thesis title: *Effects of Chloride on* H_2 *Generation and TCE Degradation in Aqueous Solutions Containing Zero Valent Iron*

B.Eng. in Environmental Engineering, 2005 – Ho Chi Minh City University of Technology, Ho Chi Minh City, Vietnam (ranking: 1/150)
Advisor: Professor Van Phuoc Nguyen
Thesis title: *Recovery of Chromium from Tannery Solid Waste*

RESEARCH EXPERIENCE DURING PH.D. STUDY

- Determined the rates and mechanisms of the heteroaggregation between carbon nanotubes and hematite nanoparticles
- Studied the impacts of solution chemistry on the disaggregation of heteroaggregates comprising carbon nanotubes and hematite nanoparticles
- Examined the effects of dimensionality on the heteroaggregation of carbon-based nanomaterials and hematite nanoparticles
- Synthesized silver nanoparticles coated with different stabilizing agents and investigated their aggregation kinetics in aquatic environments
- Investigated the influence of heteroaggregation on the antibacterial properties of citrate-coated silver nanoparticles

TEACHING EXPERIENCES

- Instructor, Department of Geography and Environmental Engineering, Johns Hopkins University (Fall 2013)
  Courses: Environmental Engineering Fundamentals I (570.301)

- Teaching assistant, Department of Geography and Environmental Engineering, Johns Hopkins University (2008 – Spring 2013)
  Courses: Physical and Chemical Processes in Environmental Engineering II (570.448) and Environmental Engineering Fundamentals I (570.301)

- Lecturer, Faculty of Environmental Engineering, Ho Chi Minh City University of Technology, Vietnam (2008)
  Course: Senior Design Project

- Assistant Lecturer, Faculty of Environmental Engineering, Ho Chi Minh City University of Technology, Vietnam(2005 – 2006)
  Courses: Environmental Modeling, Water Treatment, and Wastewater Treatment
  Labs: Chemistry for Environmental Engineering and Air Pollution

INVITIED SEMINAR TALKS

1. Rates and Mechanisms of Heteroaggregation Between Carbon Nanotubes and Hematite Nanoparticles in Aquatic Environments, Semiconductor Research Corporation Engineering Research Center TeleSeminar, June 27, 2013

PUBLICATIONS

1. Huynh, K. A., McCaffery, J. M., and Chen, K. L., Heteroaggregation Reduces Antimicrobial Activity of Silver Nanoparticles: Evidence for Nanoparticle–Cell Proximity Effects (manuscript in preparation for submission to *Environmental Science and Technology Letters*).
2. Huynh, K. A. and Chen, K. L., Disaggregation of Heteroaggregates Comprising Multiwalled Carbon Nanotubes and Hematite Nanoparticles (submitted to *Environmental Science: Process and Impacts*)
3. Huynh, K. A., McCaffery, J. M., and Chen, K. L., Heteroaggregation of Multiwalled Carbon Nanotubes and Hematite Nanoparticles: Rates and Mechanisms, *Environmental Science and Technology*, 2012, 46, 5912–5920.
4. Huynh, K. A. and Chen, K. L., Aggregation Kinetics of Citrate and Polyvinylpyrrolidone Coated Silver Nanoparticles in Monovalent and Divalent Electrolyte Solutions, *Environmental Science and Technology*, 2011, 45, 5564–5571.